

Ludwig-Maximilians-Universität München



THERMAL, ELASTIC AND SEISMIC  
SIGNATURE OF HIGH-RESOLUTION  
MANTLE CIRCULATION MODELS

Dissertation  
zur Erlangung des Doktorgrades  
der Fakultät für Geowissenschaften der  
Ludwig-Maximilians-Universität München

vorgelegt von  
Bernhard Schubert

am  
2. März 2009

**1. Gutachter:** Prof. Dr. Hans-Peter Bunge

**2. Gutachter:** Prof. Dr. Heiner Igel

**Tag der mündlichen Prüfung: 17.07.2009**

# Contents

<b>Contents</b>	<b>i</b>
<b>Summary</b>	<b>1</b>
<b>List of Figures</b>	<b>3</b>
<b>List of Tables</b>	<b>5</b>
<b>Acknowledgments</b>	<b>7</b>
<b>Introduction</b>	<b>9</b>
Scientific Goals: Prediction and Assessment of Mantle Heterogeneity	9
Concepts and Seismological Information on Mantle Structure . . . .	10
Geodynamic Interpretation of Seismic Models . . . . .	13
Critical Aspects and Former Limitations . . . . .	14
Novel Integration of Geodynamics, Mineral Physics and Seismology	16
Outline of the Thesis . . . . .	17
<b>1 Thermal versus Elastic Heterogeneity in Mantle Circulation</b>	
<b>Models</b>	<b>21</b>
1.1 Introduction . . . . .	22
1.2 Computational Methods, Boundary and Initial Condition . . . . .	24
1.2.1 Model Setup . . . . .	25
1.3 Results . . . . .	26
1.3.1 Lateral Thermal Heterogeneity . . . . .	26
1.3.2 Radial Profiles of Temperature, $v_s$ , $v_p$ and Density . . . . .	28
1.3.3 Thermal vs. Elastic 3-D Heterogeneity . . . . .	29
1.4 Comparison of Modeled Heterogeneity to Tomography . . . . .	32
1.4.1 Comparison of Spectral Characteristics . . . . .	32
1.4.2 Comparison of Amplitudes . . . . .	33
1.5 Discussion . . . . .	34
1.5.1 Amplitudes of Seismic Heterogeneity and Plume Excess Temperature . . . . .	35
1.5.2 Strong Core Heat Flux . . . . .	37

---

1.5.3	Plume Morphology and Lacking Information on the Initial Condition . . . . .	37
1.6	Conclusions . . . . .	38
1.7	Figures – Chapter 1 . . . . .	40
<b>2</b>	<b>Tomographic Filtering of Mantle Circulation Models</b>	<b>55</b>
2.1	Introduction . . . . .	56
2.2	Tomographic Filtering and Parameterization of Models . . . . .	58
2.2.1	Tomographic Filtering . . . . .	58
2.2.2	Mantle Circulation Models . . . . .	59
2.2.3	Tomographic Model S20RTS . . . . .	60
2.3	Results . . . . .	60
2.3.1	Effects of Parameterization and Tomographic Filtering . . . . .	60
2.3.2	Effects on Spectral Characteristics of Heterogeneity . . . . .	61
2.3.3	Effects on Magnitudes of Heterogeneity . . . . .	62
2.3.4	Quantitative Analysis of Magnitude Effects . . . . .	63
2.3.5	Correcting for the Effects of Reparameterization . . . . .	64
2.3.6	Correction of Spectral Characteristics . . . . .	65
2.3.7	Correction of Histograms . . . . .	65
2.4	Discussion . . . . .	66
2.4.1	Lateral Temperature Variations and Magnitudes of Seismic Heterogeneity . . . . .	66
2.4.2	Horizontal Gradients of Thermal and Seismic Heterogeneity . . . . .	68
2.4.3	Current Limitations in the Comparison of Geodynamic and Tomographic Seismic Heterogeneity . . . . .	69
2.5	Conclusions . . . . .	69
2.6	Figures – Chapter 2 . . . . .	72
	<b>Conclusions and Outlook</b>	<b>85</b>
	Potential of Studying Magnitudes of Seismic Heterogeneity . . . . .	85
	Dominance of Thermal Anomalies . . . . .	87
	Perspectives . . . . .	87
	<b>Appendix</b>	<b>89</b>
<b>A</b>	<b>Rotational Stability and Geoid of Mantle Circulation Models</b>	<b>91</b>
A.1	Introduction . . . . .	92
A.2	Model Setup . . . . .	95
A.3	Analysis of Mass Anomalies in the Mantle . . . . .	96
A.3.1	Geoids . . . . .	96
A.3.2	True Polar Wander . . . . .	98
A.4	Discussion . . . . .	100
A.4.1	Rotational Stability . . . . .	100

---

A.4.2 Geoid . . . . .	102
A.4.3 Gravity data and the potential to distinguish between competing plate reconstructions? . . . . .	103
A.5 Conclusions . . . . .	103
A.6 Figures - Chapter 3 . . . . .	106
<b>Bibliography</b>	<b>121</b>



# Summary

A long-standing question in the study of Earth's deep interior is the origin of seismic mantle heterogeneity. The challenge is to efficiently mine the wealth of information available in complex seismic waveforms and to separate the potential contributions of thermal anomalies and compositional variations. High expectations to gain new insight currently lie within the application of high-performance computing to geophysical problems. Modern supercomputers allow, for example, the simulation of global mantle flow at Earth-like convective vigor or seismic wave propagation through complex three-dimensional structures. The sophisticated computational tools incorporate a variety of physical phenomena and result in synthetic datasets that show a complexity comparable to real observations. However, it is so far not clear how to combine the results from the various disciplines in a consistent manner to obtain a better understanding of deep Earth structure from the expensive large-scale numerical simulations. In particular, it is important to understand how to build conceptual models of Earth's mantle based on geodynamic considerations that can be quantitatively assessed and used to test specific hypotheses. One specific goal is to generate seismic heterogeneity from dynamic flow calculations that can be used in global wave propagation simulations so that synthetic seismograms can be directly compared to seismic data without the need to perform inversions.

In the multi-disciplinary study presented here, a new method is developed to theoretically predict and assess seismic mantle heterogeneity. Forward modeling of global mantle flow is combined with information from mineral physics and seismology. Temperatures inside the mantle are obtained by generating a new class of mantle circulation models at very high numerical resolution. The global average grid spacing of  $\sim 25$  km (around 80 million finite elements) allows for the simulation of flow at Rayleigh numbers on the order of  $10^9$  and to resolve a thermal boundary layer thickness of around 100 km. To assess the predicted present day temperature fields, the geodynamic flow calculations are post-processed with published thermodynamically self-consistent models of mantle mineralogy for a pyrolite composition to convert thermal structure into elastic parameters. Quantitative predictions of the magnitudes of seismic velocity and density variations are thereby possible due to the appropriately high numerical resolution necessary to obtain temperature variations that are consistent with the mineralogical con-

version. The resulting structures are compared to tomographic models based on a variety of statistical measures taking into account the limited resolving power of the seismic data. In a final step, the geodynamic models are investigated with respect to the influence of strong convective mass transport on the stability of Earth's rotation axis. This additional and independent analysis provides information on whether strongly bottom heated isochemical mantle circulation can be reconciled with paleomagnetic estimates of true polar wander.

One specific question that can be addressed with this approach is the origin of two large regions of strongly reduced seismic velocities in the lowermost mantle. Several seismological observations are interpreted as being caused by compositional variations. However, a large number of recent geodynamical, mineralogical and also seismological studies argue for a strong thermal gradient across the core-mantle boundary that might provide an alternative explanation through the resulting large temperature variations. Here, the forward modeling approach is used to test the assumption whether the presence of a strong thermal gradient in isochemical whole mantle flow is compatible with a variety of geophysical observations.

The results show that the temperature variations deduced from the new high-resolution mantle circulation models are capable of explaining gross statistical features of mantle structure mapped by tomography. The main finding is that models with strong core heating, which also give a surface heat flux consistent with observations, yield realistic depth profiles of root-mean-square (RMS) variations of shear wave velocity. Most importantly, only models with a large core contribution to the mantle energy budget are compatible with the strong negative seismic anomalies in the large low velocity provinces of the lower mantle. Taking into account the effects of limited resolving power of seismic data on the magnitudes of predicted seismic heterogeneity further improves this match to tomographic models. This illustrates that seismic heterogeneity is likely dominated by thermal variations and thus limits the possible role of chemical heterogeneity in the lower mantle. Altogether, the results strengthen the notion of strongly bottom heated isochemical whole mantle flow with a pyrolite composition. Furthermore, these findings give confidence in the consistency of the presented approach and demonstrate the great potential of geophysical large-scale high-performance simulations and their application to seismic data and tomographic models.



# List of Figures

1.1	Depth slices through tomographic mantle models of shear wave velocity S20RTS, TX2007, HMSL-S06 and PRI-S05 . . . . .	41
1.2	Three-dimensional view of temperature variations in mantle circulation model M2 with 35% core heating . . . . .	43
1.3	Depth slices through mantle circulation models M1 and M2 with weak and strong core heat flux . . . . .	44
1.4	Radial profiles of temperature, density, $v_s$ and $v_p$ in mantle circulation models M1–M4 . . . . .	45
1.5	Spectral power of heterogeneity in temperature and shear wave velocity for mantle circulation models M1–M4 . . . . .	47
1.6	Histograms of variations in temperature and shear wave velocity for mantle circulation models M1–M4 . . . . .	49
1.7	Spectral power of heterogeneity in shear wave velocity for tomographic models S20RTS, TX2007, HMSL-S06 and PRI-S05 . . . . .	50
1.8	Histograms of variations in shear wave velocity in tomographic models S20RTS, TX2007, HMSL-S06 and PRI-S05 . . . . .	51
1.9	Comparison of RMS amplitudes of heterogeneity between tomographic and geodynamic models . . . . .	52
2.1	Depth slices through tomographically filtered mantle circulation model M2 and tomographic model S20RTS . . . . .	73
2.2	Spectral heterogeneity maps for tomographically filtered mantle circulation models M1 and M2 . . . . .	75
2.3	Histograms of relative variations in $v_s$ for tomographically filtered mantle circulation models M1 and M2 . . . . .	77
2.4	Profiles of RMS amplitudes and relative amplitude reduction due to the reparameterization and tomographic filtering for mantle circulation model M2 . . . . .	78
2.5	RMS profiles of $v_s$ variations in the tomographically filtered models M1 and M2, corrected for the effects of reparameterization . . . . .	79
2.6	Spectral heterogeneity maps for the tomographically filtered models M1 and M2, corrected for the effects of reparameterization . . . . .	81

---

2.7	Histograms of $v_s$ variations in the tomographically filtered models M1 and M2, corrected for the effects of reparameterization . . . . .	83
A.1	Depth slices through the present day density distribution of mantle circulation model M2 . . . . .	107
A.2	Geoid kernels for different spherical harmonics degrees and the corresponding radial viscosity structure . . . . .	109
A.3	Comparison of observed and synthetic geoids . . . . .	111
A.4	Spectral amplitude of synthetic geoids and correlation with the observed geoid . . . . .	113
A.5	Synthetic true polar wander paths in the last 100 Ma computed from the mantle circulation models . . . . .	115
A.6	Spectral amplitude of density structure in degree 2 of the mantle circulation models as a function of depth and time . . . . .	117
A.7	Correlation of the synthetic and measured geoid as a function of viscosity increase at the upper mantle/lower mantle boundary and thickness of the asthenosphere . . . . .	118
A.8	Comparison of plate reconstructions by <i>Müller et al.</i> [2008] and <i>Lithgow-Bertelloni et al.</i> [1993] . . . . .	119

# List of Tables

1.1	Physical parameters and values employed in the simulations of mantle circulation . . . . .	53
1.2	Parameters and input values varied between mantle circulation models M1–M4 . . . . .	53
A.1	Parameters and input values varied between mantle circulation models M1, M1.5, and M2 . . . . .	120



# Acknowledgments

First of all, I want to thank my supervisor Prof. Hans-Peter Bunge for his guidance, valuable advice and for proposing this very interesting and scientifically rich PhD project. He always was willing to share his experience in long discussions and I am very grateful for everything that I learned from him. I am also very happy that he supported my wishes to attend international meetings and that he enabled contacts to a large number of scientists from all over the world.

I also want to thank my second supervisor Prof. Heiner Igel for initially raising my interest in seismology in general, and numerical wave propagation in particular. Discussions with him helped a lot to keep an eye on the seismological aspects of my project and I owe him many thanks for that he enabled my participation in all SPICE workshops, through which I obtained a broad overview of computational seismology. I am also happy to share his enthusiasm for cycling and thank him for many bike events that helped to forget about science from time to time.

Many thanks to Jeroen Ritsema (Univ. of Michigan, USA), Gerd Steinle-Neumann (Bayerisches Geoinstitut, Bayreuth) and Katrin Schaber (LMU Munich) for fruitful collaboration, vital discussions, and criticism on the work presented in this thesis. I also want to thank Saskia Goes and three anonymous reviewers for detailed and constructive comments on the papers in chapters 1 and 2.

Furthermore, I thank Lars Stixrude, Carolina Lithgow-Bertelloni and Antonio Piazzoni for providing their mineralogical models, Ch. Houser, M. Ishii, H. Karason, G. Masters, R. Montelli, J. Ritsema, N. Simmons and W.-J. Su for providing their tomographic models and the staff of the Leibniz-Rechenzentrum (LRZ) Munich, Germany for their support.

A big “thank you” to Markus Treml for many pleasant and enlightening discussions, which added to raising my interest in studies of Earth’s deep interior; to Christoph Moder for help on shell scripting, awk and sed programming and for sharing his experience on visualization of large volume data; and to Jens Oeser for setting up and maintaining a wonderful computational infrastructure at the Geophysics Institute in Munich and for support on technical issues.

Then, I owe a lot to my room mates, especially to Tini Plattner and Dieter Kurrle. Many thanks for helpful advice and for the sometimes urgently needed

distraction from dull work. For general help, advice and lively discussions during the last years I would like to thank my colleagues Karin Sigloch, Rocco Malservisi, Marcus Mohr, Andreas Fichtner, Martin Käser, Josep de la Puente and all the rest of the Geophysics Institute in Munich.

Special thanks to my brother Christian and my parents Regina and Erwin Schubert for permanent encouragement and all that they have done to make this possible.

And finally, very special thanks to my wife Cornelia for continuing help and support, and for bearing my moods during the preparation of this thesis.

This research was funded by the International Graduate School THESIS within the Elite-Network of Bavaria.

# Introduction

To date, the structure and evolution of Earth's mantle is still a matter of debate and especially the origin of seismic heterogeneity remains elusive. New insight seems now within reach due to the rise of computer technology, as scientific high-performance computing on large tera-flop supercomputers is currently revolutionizing the geosciences. Numerical solutions to a large number of problems encountered in geophysics are available nowadays and existing computational resources allow, for example, the simulation of global mantle flow or seismic wave propagation through complex three-dimensional structures. While algorithm development is at a fairly advanced stage, the routine application of these tools with the associated potential large impact is just at the beginning. Only in the last few years, computing full waveform synthetic seismograms for teleseismic studies that capture the full complexity of 3-D wave fields became feasible. Before, one classically had to resort to solution methods with substantial limitations to compute theoretical seismograms (e.g., ray theoretical approximations, one-dimensional structures, single-scattering Born theory etc.). Thus, the full impact of 3-D Earth structure on the observed wave field has not yet been explored.

In this respect however, it is not clear how to efficiently use available parallel computing architectures and sophisticated software tools to test theoretical models against observations in order to obtain a better quantitative understanding of mantle structure. One of the key questions still unanswered is how to build models of material properties in Earth's mantle from geodynamic considerations in such a way that they can be used for the simulation of seismic wave propagation. This relates to the fact that still rather little is known about the lateral variations in material parameters such as temperature and composition. The challenge is to consistently couple theoretical tools and methods from geodynamics, mineral physics and seismology so that specific geophysical hypotheses can be tested directly against seismic data without the need to perform inversions.

## **Scientific Goals: Quantitative Prediction and Assessment of Seismic Mantle Heterogeneity**

In the study presented here, a sequence of modeling and diagnostic steps is developed that work towards a comprehensive assessment of geodynamic models.

The multi-disciplinary approach integrates theoretical models generated using large-scale numerical simulations, tomographic images and observational data. The final aim is to generate predictions of mantle heterogeneity from a forward modeling approach that can be used for global wave propagation simulations. For this, the primary objectives are to obtain a better understanding of lateral temperature variations and seismic anomalies to be expected in vigorous mantle convection on the one hand, and how to combine the various modeling steps to allow for a consistent assessment of predicted mantle heterogeneity on the other hand. This involves a clear understanding of how to set up geodynamical simulations and how to do proper comparisons to tomography, for which information from mineral physics is needed to relate temperatures to elastic parameters. Finally, models that successfully pass the comparison with tomography have to be further tested against geodetic and paleomagnetic observations for additional independent verification. The coherent diagnostic procedure set up for this study can be used in the future to validate geodynamically derived elastic structures that are intended to be used for large-scale computations of 3-D full waveform synthetics.

## **General Concepts and Seismological Information on Mantle Structure**

The evolution of Earth's mantle over time is one of the major controlling factors for a variety of phenomena that directly affect the daily life of many people world wide. The continuous motions within the mantle on the order of millimeters to centimeters per year result in plate tectonics and especially the faulting of the crust. In consequence, the steady transport of material at the Earth's surface regularly produces earthquakes and volcanism all over the world. Zones of such active tectonic processes are, for example, located all around the Pacific Ocean, where the Nazca, Cocos, Juan de Fuca, Philippine and Pacific Plate are subducted beneath the Americas, and the Eurasian and Australian continents. Another famous region of long-lived subduction is from the Mediterranean to India, where the closure of the Tethys Ocean has led to the formation of large Mountain ranges from the Alps in the West to the Himalaya in the East.

The idea of plate tectonics has its origin in the theory of continental drift put forward in the pioneering work of Alfred Wegener in the early 20th century [[Wegener 1915](#)]. Several decades later, only in the 1960s, unequivocal evidence for continuous plate motions has been found in form of variations in the magnetization of ocean seafloor and the matching patterns of these on either side of spreading centers [[Vine and Matthews 1963](#)]. Since the discovery of plate tectonics, our understanding of planet Earth has undergone dramatic changes. Early ideas about mechanisms and forces that lead to the observed surface expressions of lithospheric plate motions included the fundamental concept of convection in



the mantle, and the hypothesis that the upper and lower mantle convect as two separate layers. But despite the awareness of the potential threat from natural hazards, rather few is known on the forces and processes inside the Earth that drive mantle flow.

The hypothesis of two-layered convection was promoted by findings from geochemistry arguing for (at least) two compositionally distinct reservoirs being present in the mantle [*McKenzie and Richter 1981*; *Allegre 1982*]. A separation of the upper and lower mantle seemed at first also plausible in the light of seismological studies. The extensive analysis of arrival times of seismic waves, radiated by earthquakes and recorded all over the world, led to the construction of 1-D profiles of elastic parameters [e.g., *Gilbert and Dziewonski 1975*; *Dziewonski and Anderson 1981*; *Kennett and Engdahl 1991*; *Kennett et al. 1995*]. These profiles revealed that the first-order radial structure of the Earth shows discontinuities in seismic wave speeds and density not only between crust, mantle and outer as well as inner core, but also between the upper and the lower mantle. It turned out that at least two such discontinuities can be observed globally inside the mantle at 410 and 660 km depth, the latter of which marks the upper mantle/lower mantle boundary. These discontinuities are commonly thought to reflect changes in physical parameters of the mantle due to phase transformations of minerals, such as olivine. Especially important for the dynamics of the mantle is the fact that the phase transformation of olivine at the 660 km discontinuity has a negative Clapeyron slope. This means that both, downward flow of cold material in the upper mantle as well as upward flow of hot material in the lower mantle, encounter resisting forces at this boundary.

Since then, the challenge has been to extend the 1-D models by allowing for lateral variations in seismic velocities. Mapping the three-dimensional elastic structure of the mantle is important as it reflects changes in temperature (and possibly chemical composition), which contribute to density and thus buoyancy differences that drive mantle flow. In the last decades, seismologists have made great progress in imaging the distribution of elastic parameters with a technique known as seismic tomography. Similar to medical tomography, seismic waves inside the Earth are represented as rays penetrating the Earth along various paths and recorded with seismometers at different positions all over the globe. In this way, the interior of the Earth is illuminated from all directions leading to the construction of 3-D images of Earth's interior. Today, a large number of tomographic models exist for both compressional ( $v_p$ ) and shear wave velocity ( $v_s$ ).

Despite the various indications for two-layered convection, seismic tomography produced images of mantle structure that clearly showed slabs of faster than average seismic velocities crossing — and being located well below — the 660 km discontinuity [*van der Hilst et al. 1991*]. Some of these slabs have been imaged all the way down to the core-mantle boundary (CMB), and all tomographic models now consistently show fast seismic anomalies in the lowermost mantle that

are concentrated in the circum-Pacific and regions under Asia [e.g., *Dziewonski et al.* 1977; *Su et al.* 1994; *Li and Romanowicz* 1996; *Grand et al.* 1997; *van der Hilst et al.* 1997; *Su and Dziewonski* 1997; *Kennett et al.* 1998; *Masters et al.* 2000; *Ritsema et al.* 2004; *Montelli et al.* 2006; *Panning and Romanowicz* 2006; *Simmons et al.* 2007; *Houser et al.* 2008; *Kustowski et al.* 2008]. Geodynamicists now widely agree that this feature is associated with cold downwellings from past subduction driving a substantial part of the mantle general circulation [*Richards and Engebretson* 1992; *Bunge et al.* 1998; *Lithgow-Bertelloni and Richards* 1998; *Becker and O’Connell* 2001; *Conrad and Lithgow-Bertelloni* 2002; *McNamara et al.* 2002]. Thus, the hypothesis of complete separation of upper and lower mantle has been dropped, but still the idea of partial separation and chemical differences between the two layers is favored by a number of geophysicists.

Recently, further improvements in seismic tomography, taking into account finite frequency effects of the wave field, led to highly resolved images of lower mantle plumes [*Montelli et al.* 2004, 2006] that extend from the core-mantle boundary all the way up to the 660 km discontinuity. *Nolet et al.* [2006] computed the expected amount of heat transported by the plumes observed in tomography and argued that the plume flux calculated from hotspot bathymetry [*Sleep* 1990] is strongly underestimated. Plumes probably contribute a significant part of the total of 30 TW that has to cross the upper mantle/lower mantle boundary, a value that is in line with the geodynamical estimates of heat being available in the mantle due to core heating. Moreover, such large values of heat flux can hardly be accounted for only by conduction, but rather require substantial heat advection.

Despite this further hint to extensive mass exchange across the 660 km discontinuity, the images of plumes showed clearly that seismically slow and therefore rather hot material stalls at the discontinuity, deflects there and forms broad plume heads. *Nolet et al.* [2006] took this as evidence for the discontinuity being accompanied by a thermal boundary layer and that smaller secondary plumes spawn from the upper mantle/lower mantle boundary to transport the heat to the surface. This view is supported by further evidence of the resistant nature of the 660 km discontinuity, as also some of the subducting slabs seem to come to rest there [*van der Lee and Nolet* 1997; *Fukao et al.* 2001].

Modern tomographic models also show remarkable agreement in that the long-wavelength structure in the lower mantle is dominated by two large low velocity regions under the Pacific and under Africa. The velocity reduction in these two regions is very strong, around  $-3$  to  $-4\%$  depending on the tomographic model. These so-called “superplumes” are therefore expected to play an important role for the dynamics of the mantle, but their origin still remains elusive.

Several studies argue that these regions are characterized by a different bulk composition from the surrounding mantle [*Ritsema et al.* 1999; *van der Hilst and Karason* 1999; *Wen et al.* 2001; *Ni et al.* 2002; *Ni and Helmberger* 2003; *Ritsema and van Heijst* 2002; *Deschamps and Trampert* 2003; *Wang and Wen*

2004] and that they show an increased density [Ishii and Tromp 1999, 2001]. Supporting evidence comes from probabilistic models of mantle heterogeneity [Resovsky and Trampert 2003; Trampert et al. 2004], and from seismic studies that simultaneously map the pattern of bulk sound and shear wave velocities [Kennett et al. 1998; Masters et al. 2000]. An additional argument for chemical heterogeneity was taken from direct observations of traveltime variations obtained from rays traversing the lower mantle under Africa, which indicate that the low-velocity structure there shows very rapid changes in physical parameters at its boundary (i.e., “sharp sides of the African superplume”).

## Geodynamic Interpretation of Seismic Models

Geophysicists have long sought to interpret the seismic heterogeneity in a geodynamic context and to incorporate the tomographic images into the framework of plate tectonics and mantle convection. The complex character of the low seismic velocity anomalies in the lower mantle has led to a wide range of speculations about possible mechanisms leading to the observed structures. A popular idea is that a higher density may be due to iron enrichment, which would help to explain the observed large velocity reduction in addition to creating and stabilizing the long-wavelength nature of the superplumes. Hot buoyant mantle from a strong thermal boundary layer at the CMB would provide a straightforward alternative explanation for these anomalies. This view is promoted by a large number of studies from geodynamics, seismology and mineral physics arguing for a high CMB temperature and a large heat flux from the core into the mantle [e.g., Glatzmaier and Roberts 1995; Kuang and Bloxham 1997; Boehler 2000; Steinle-Neumann et al. 2001; Buffett 2002; Gubbins et al. 2004; Nimmo et al. 2004; Nolet et al. 2006; Alfè et al. 2002; Alfè et al. 2007; van der Hilst et al. 2007; Steinberger and Holme 2008].

Several studies tried to shed light on the state and composition of the mantle by investigating the 1-D seismic reference profiles and inverting them for the average geotherm and compositional gradient with depth [see e.g., Khan et al. 2008, for a summary]. A problem that arises in all of these studies is that seismic velocities are sensitive to changes in temperature and composition in a similar manner. This results in trade-offs between the various parameters (e.g., thermal anomalies, iron and perovskite content) leaving a wide range of possible combinations that explain the radial seismic structure of the mantle equally well. For example, as a result of trade-offs between thermal and chemical effects, the 1-D temperature profile has been both proposed to be super- as well as subadiabatic, in conjunction with a variety of different possible chemical gradients [e.g., Jackson 1998a; Marton and Cohen 2002; Deschamps and Trampert 2004; Mattern et al. 2005; Matas et al. 2007; Khan et al. 2008]. Further uncertainties arise from the use of different seismic and mineralogical data sets and forward or inverse methodologies applied, as well as from geographic bias due to uneven ray

coverage when only traveltimes are used. Moreover, it has yet to be shown that non-linearities expected in the relation of thermal anomalies and seismic variations can readily be ignored and that the mapping of 1-D seismic profiles into an average radial geotherm is meaningful.

Taking advantage of developments in numerical fluid dynamics and the steady increase in computational resources, geodynamicists now have the means at hand to solve the equations of motions for the whole mantle. Owing to parallelization of computer codes, full 3-D models in spherical shells can be computed since the mid-1990s [*Bunge and Baumgardner 1995*]. In this way, systematic studies on the influence of a variety of parameters on flow patterns and temperature variations were possible. Based on spectral analyses, the major controlling factors on mantle flow were found to be the radial viscosity stratification and the existence of stiff lithospheric plates [*Bunge and Richards 1996; Bunge et al. 1996, 1997*].

For deep Earth studies involving the comparison of geodynamically predicted structures with tomography, mantle circulation modeling is the method of choice today [e.g., *Bunge et al. 2002; McNamara and Zhong 2005*]. Similar to the techniques applied in meteorology, geological data (e.g., models of plate motion history in particular) are incorporated into the geodynamic models through a process which is usually termed “sequential data-assimilation”. So far, however, simulations were restricted in grid resolution, limiting their ability to model convection at Earth-like Rayleigh-number, which is on the order of  $10^9$ .

Classically, the simulated mantle structures then were either directly compared to tomographic models by correlation of geographic pattern or analyzed in their spectral power of heterogeneity [e.g., *Bunge et al. 1998, 2002; McNamara and Zhong 2005*]. In most cases so far, a qualitative agreement or disagreement between the spectral characteristics of predicted temperatures and the seismic properties of tomographic models was taken to be sufficient to judge a certain geodynamic model. However, several problems exist with the assessment of geodynamically predicted heterogeneity and little is actually known about how to set up geodynamic studies on mantle structure in a way that they can be consistently, and even more importantly, quantitatively tested against the existing data.

## **Critical Aspects and Former Limitations in the Assessment of Geodynamic Models**

Temperature and elastic parameters are related in complicated ways through the material properties of mantle mineralogy. Therefore, the interpretation of temperatures in terms of elastic mantle structure and a direct comparison with tomographic models may be incomplete and misleading. To prevent misinterpretations, temperatures need to be converted into seismic velocities prior to the comparisons. Geodynamic studies so far were based on simple depth-independent

linear conversions between temperature and seismic velocities, which limited their ability to investigate geodynamically predicted seismic heterogeneity in a quantitative manner [e.g., *Mégnin et al. 1997*; *Bunge and Davies 2001*; *Davies and Bunge 2001*; *Bunge et al. 2002*; *Ritsema et al. 2007*]. Furthermore, the simplified conversion was not suited to capture the non-linear effects expected in the transition zone [*Stixrude and Lithgow-Bertelloni 2007*].

A second problem is that the geographic location of predicted mantle structure strongly depends on the initial and boundary conditions of the forward problem of geodynamics. For example, uncertainties in the plate motion history grow with age of the reconstructions, resulting in poorly constrained location of structure in the lowermost mantle. An even more important problem exists in finding an appropriate initial condition for the temperatures in the geologic past, which ultimately limits us to geographically correlate geodynamic and tomographic models.

A further difficulty exists in that tomographic models inherently suffer from limited resolving power of the data sets available. The fundamental problem in tomographic inversion is that earthquakes are mostly located around plate margins and that seismic receivers can usually only be set up on land. The restricted source-receiver geometries result in uneven seismic data coverage, which leads to a non-uniqueness inherent in tomographic inversions. In order to obtain stable solutions, the inverse problems require regularization (e.g., smoothing and/or damping). As a result, tomographic images are always blurred versions of the true structure of the Earth. Therefore, seismic anomalies tend to be smeared in all directions, and their magnitude will on average be smaller than the real velocity variations. It has been shown by a number of studies that it is crucial to take the effects of uneven data coverage and damping into account when comparing geodynamic models to tomography [e.g., *Mégnin et al. 1997*; *Bunge and Davies 2001*; *Davies and Bunge 2001*; *Ritsema et al. 2007*].

Finally, geodynamic models that are compatible with tomography need to also satisfy further independent observations. One such example is true polar wander (TPW), the coherent motion of the Earth's surface with respect to its rotation axis, which is most likely controlled by redistribution of deep seated mass anomalies due to vigorous convection inside the Earth's mantle. Paleomagnetic evidence suggests that this motion has been small, not exceeding more than 10–15° of latitudinal variation during the past 100 million years (Ma) [*Besse and Courtillot 1991, 2002*; *Tarduno and Smirnov 2001*]. Thus, the rate of TPW has been on average only about 0.1° to 0.2° per Ma.

In summary, the key problems that need to be addressed in building and testing conceptual models of Earth's mantle are:

1. Relation between temperature and elastic parameters
2. Trade-offs between temperature and composition
3. Boundary and initial conditions of global mantle flow
4. Effects of limited tomographic resolution in the comparison of seismic structures
5. Assessment of models against a range of independent data sets

## **Novel Integration of Geodynamics, Mineral Physics and Seismology**

It is highly desirable to address the above problems all at once by combining concepts from geodynamics, mineral physics and seismology into an integrative study. The existence of tera-flop supercomputers and a series of recent breakthrough developments in these fields now make it possible to couple the various tools and methods in a consistent manner.

For example, progress in the extent and precision of experiments in high pressure mineral physics (e.g., equation of state by X-ray diffraction, phase equilibria, calorimetric data) as well as advances in first principles calculations of material properties recently enabled the construction of thermodynamically self-consistent models of mantle mineralogy [e.g., *Ricard et al. 2005*; *Piazzoni et al. 2007*; *Stixrude and Lithgow-Bertelloni 2005, 2007*]. Based on Gibbs free energy minimization, the stable phase assemblage can thus be computed for every P,T,x (pressure, temperature, composition) condition of the mantle. From the temperature dependent phase diagrams, physical properties such as density, bulk and shear modulus can be calculated by equation of state extrapolation. In this way, non-linearities in the temperature sensitivity of the elastic moduli or density can now be taken into account.

In the analysis of seismic properties and their relation to temperature via a mantle mineralogy model one needs to pay special attention to the vigor of convection, as one must ensure that modeled temperature variations are consistent with temperature variations assumed in the underlying mineralogy. For this, large computing power involving hundreds to thousands of processors is needed, which is only available recently. Owing to this increase in computational resources it is now possible to employ a new class of global mantle circulation models (MCMs) at very high numerical resolution. This allows to approach for the first time the vigorous regime of global mantle flow and to construct its corresponding elastic structure.

Here, the first such high-resolution mantle circulation models are presented and tested against tomography. For a quantitative assessment of the geodynamic models, the simulations of global mantle flow are combined with recently published thermodynamic models of mantle mineralogy and tools to account for the effects of limited resolving power of tomography. This way, the analysis presented in this thesis strives for a better understanding of lateral variations in temperature and seismic velocities inside the Earth. The major benefit is that only the consistent combination of all relevant geophysical disciplines will enable us to limit the classical trade-offs between inferred temperature variations and chemical heterogeneity.

Altogether, the important novelty of the approach presented here is that one can directly relate changes in physical parameters governing the motion of the mantle to changes in elastic structures, and in the future to seismic data. The results of this study are of great relevance to future geophysical, as well as geochemical, deep Earth studies, as they provide further constraints on mantle dynamics and will be especially helpful in building consistent conceptual models of the Earth.

## Outline of the Thesis

The analysis of high-resolution mantle circulation models is organized in three parts. Chapter 1 deals with the model generation, the differences between thermal heterogeneity and elastic heterogeneity and a first comparison to four tomographic S-wave models. In chapter 2, the comparison to tomography is extended by taking into account tomographic resolution effects. Finally, in appendix A, an analysis of true polar wander deduced from the geodynamic models is described. This additional part is based on the diploma study of Katrin Schaber [Schaber 2008], which was co-supervised by the author.

### Chapter 1: Thermal versus Elastic Heterogeneity in High-Resolution Mantle Circulation Models with Pyrolite Composition

In chapter 1, forward modeling of global mantle flow is used to test whether strong core heating results in seismic heterogeneity compatible with tomographic models in terms of spectral characteristics and magnitude. As noted above, a large thermal gradient across the CMB is favored by a number of recent studies. To keep things simple, and to isolate the effects of core heating, the study is focused on isochemical whole mantle circulation. The pyrolite model [Ringwood 1975; Irifune 1987] is consistent with this choice.

This chapter starts with a brief description of the computational methods and parameters employed. Next, the influence of thermal heterogeneity on corresponding variations in  $v_s$  and  $v_p$  is investigated and the seismic structures are

compared to tomographic models directly and with statistical measures, such as the spectral power, histograms and RMS profiles of heterogeneity.

For the conversion of temperatures into elastic parameters, two of the aforementioned thermodynamic models of mantle mineralogy are used [*Piazzoni et al. 2007*; *Stixrude and Lithgow-Bertelloni 2007*], coupled to a model of shear moduli [*Stixrude and Lithgow-Bertelloni 2005*]. In both models, stable phase assemblages in the CFMAS (CaO – FeO – MgO – Al<sub>2</sub>O<sub>3</sub> – SiO<sub>2</sub>) system are computed by Gibbs Free Energy minimization prior to the equation-of-state extrapolation of physical parameters.

Given the problems related to constraining the geographic pattern of mantle heterogeneity, spectral characteristics are only examined briefly. The magnitudes of thermal and elastic heterogeneity however, which are analyzed in form of histograms, seem to be a good measure for the comparison of geodynamic and tomographic models.

Chapter 1 has been published in “Geochemistry, Geophysics, Geosystems”: *Schubert, B. S. A., H.-P. Bunge, G. Steinle-Neumann, C. Moder, and J. Oeser (2009), Thermal versus elastic heterogeneity in high-resolution mantle circulation models with pyrolite composition: High plume excess temperatures in the lowermost mantle, *Geochem. Geophys. Geosyst.*, 10 (1), Q01W01, doi: 10.1029/2008GC002235.*

## **Chapter 2: Tomographic Filtering of High-Resolution Mantle Circulation Models**

In chapter 2, the comparison of the mantle circulation models with tomography is extended by taking into account the limited resolving power of tomographic inversions; that is, the models are modified to reflect the effects of uneven seismic data coverage and damping. Here, this is achieved by “filtering” the shear wave velocity structures from the MCMs with the resolution operator of tomographic S-wave model S20RTS [*Ritsema et al. 2004*]. As noted before, the models in this study benefit from recent progress in mineral physics, which now provides improved relations between thermal and elastic parameters based on the thermodynamically self-consistent treatment of mineral phase assemblages. By combining these advances with an analysis of the effects of limited tomographic resolution, a quantitative comparison of geodynamically predicted seismic heterogeneity with tomography is now possible.

This chapter starts with a short description of the tomographic filtering process. The filtering involves the transformation of the geodynamic models onto the parameterization of S20RTS, which has important implications for the following analysis of seismic heterogeneity. As in chapter 1, the comparison of the tomographically filtered mantle circulation models with S20RTS is focused on the magnitudes of shear wave velocity variations. Moreover, the gradients of  $v_s$  are analyzed and compared to the sharp sides of the African superplume.



Chapter 2 is accepted for publication in “Geochemistry, Geophysics, Geosystems”: *Schuberth, B. S. A., H.-P. Bunge and J. Ritsema (2009), Tomographic Filtering of high-resolution mantle circulation models: Can seismic heterogeneity be explained by temperature alone?*, accepted in *Geochem. Geophys. Geosyst.*,

### **Appendix A: Rotational Stability and Geoid of High-Resolution Mantle Circulation Models**

In a final step, the MCMs are tested against geodetic and paleomagnetic observations. Synthetic geoids are computed for the density structure of the models, which are compared to the geoid obtained from satellite measurements. Furthermore, true polar wander paths and speeds are computed from the density distributions corresponding to the different stages of the plate tectonic reconstructions.

First, theory and analytic methods involved in geoid and TPW computation are reviewed briefly. Then, the effects of substantial core heat flux on the rotational stability of MCMs are explored, testing the hypothesis that strongly bottom heated mantle flow is compatible with the record of Mesozoic and Cenozoic polar motion. Synthetic geoids and TPW are calculated analytically from the predicted density anomalies taking the same viscosity profile assumed in the MCMs. This assures consistency between modeled mantle heterogeneity and its geoid and TPW response.

Appendix A is in submission to “Geochemistry, Geophysics, Geosystems”: *Schaber, K., H.-P. Bunge, B. S. A. Schuberth and R. Malservisi (2009), Rotational stability and geoid of a strongly core heated Earth*, *Geochem. Geophys. Geosyst.*, *subm.*



# Chapter 1

## Thermal versus Elastic Heterogeneity in High-Resolution Mantle Circulation Models with Pyrolite Composition: High Plume Excess Temperatures in the Lowermost Mantle\*

### Abstract

We study a new class of high-resolution mantle circulation models and predict their corresponding elastic heterogeneity. Absolute temperatures are converted to seismic velocities using published thermodynamically self-consistent models of mantle mineralogy for a pyrolite composition. A grid spacing of  $\sim 25$  km globally allows us to explore mantle flow at earth-like convective vigor so that modeled temperature variations are consistent with the underlying mineralogy. We concentrate on isochemical convection and the relative importance of internal and bottom heating in order to isolate the thermal effects on elasticity. Models with a large temperature contrast on the order of 1000 K across the core-mantle boundary, corresponding to a substantial core heat loss of up to 12 TW, result in elastic structures that agree well with tomography for a number of quantitative measures: These include spectral power and histograms of heterogeneity as well as radial profiles of root-mean-square amplitudes. In particular, high plume excess temperatures of +1000–1500 K in the lowermost mantle lead to

---

\*Chapter 1 has been published in “Geochemistry, Geophysics, Geosystems”: *Schuberth, B. S. A., H.-P. Bunge, G. Steinle-Neumann, C. Moder, and J. Oeser (2009), Thermal versus elastic heterogeneity in high-resolution mantle circulation models with pyrolite composition: High plume excess temperatures in the lowermost mantle, *Geochem. Geophys. Geosyst.*, 10 (1), Q01W01, doi:10.1029/2008GC002235.*

significant negative anomalies of shear wave velocity of up to  $-4\%$ . These are comparable to strong velocity reductions mapped by seismic tomography in the prominent low-velocity regions of the lower mantle. We note that the inference of a large core heat flux is supported by a number of geophysical studies arguing for a substantial core contribution to the mantle energy budget. Additionally, we find significant differences between the characteristics of thermal heterogeneity and the characteristics of elastic heterogeneity in the transition zone due to phase transformations of upper mantle minerals. Our results underline the necessity to include mineral physics information in the geodynamic interpretation of tomographic models.

## 1.1 Introduction

Seismic tomography has advanced to a point where it provides considerable insight into the structure of the deep Earth. Particularly important for our understanding of deep Earth processes are two robust features of lower mantle heterogeneity (see Figure 1.1): One is a long wavelength fast seismic velocity anomaly concentrated into the circum-Pacific and regions under Asia [e.g., *Li and Romanowicz 1996; Masters et al. 1996; Grand et al. 1997; van der Hilst et al. 1997; Su and Dziewonski 1997; Kennett et al. 1998; Masters et al. 2000; Ritsema and Van Heijst 2000; Ritsema and van Heijst 2002; Montelli et al. 2004, 2006*]. It is now widely agreed upon by geodynamicists that this feature is associated with cold downwellings from past subduction driving a substantial part of the mantle general circulation [*Richards and Engebretson 1992; Bunge et al. 1998; Lithgow-Bertelloni and Richards 1998; Becker and O'Connell 2001; Conrad and Lithgow-Bertelloni 2002; McNamara et al. 2002*].

Less certain is the origin of another feature consisting of two pronounced low seismic velocity anomalies located beneath the Pacific and under Africa. Hot buoyant mantle from a strong thermal boundary layer at the core-mantle boundary (CMB) would provide a straightforward explanation for these anomalies. However, several studies argue that these regions are characterized by a different bulk composition from the surrounding mantle [*Ritsema et al. 1999; Ishii and Tromp 1999, 2001; van der Hilst and Karason 1999; Wen et al. 2001; Ni et al. 2002; Ni and Helmberger 2003; Ritsema and van Heijst 2002; Deschamps and Trampert 2003; Wang and Wen 2004*]. Supporting evidence for this comes from probabilistic models of mantle heterogeneity [*Resovsky and Trampert 2003; Trampert et al. 2004*], and from seismic studies that simultaneously map the pattern of bulk sound and shear wave velocities [*Kennett et al. 1998; Masters et al. 2000*].

The complex character of the low seismic velocity anomalies has prompted geodynamicists to investigate the behavior of mantle flow with compositional variations [e.g., *Christensen and Hofmann 1994; Davaille 1999; Kellogg et al.*

1999; *Tackley 2000, 2002*], and to illuminate the dynamic consequences of a dense component in the deep mantle [*Hansen and Yuen 1989, 1994, 2000; Montague and Kellogg 2000; Davaille et al. 2002; Stegman et al. 2002; Jellinek and Manga 2004; Nakagawa and Tackley 2004; McNamara and Zhong 2004b, 2005; Farnetani and Samuel 2005*].

Equally important for our understanding of these anomalies is the thermal state of the mantle, which is complicated by the simultaneous presence of mixed heating modes, i.e., by the effects of internal heating from radioactive decay and bottom heating from the core. The subadiabatic nature of the mantle geotherm away from thermal boundary layers is a direct consequence of internal heating, as noted early on by *Jeanloz and Morris [1987]*, and there is growing consensus that the mantle geotherm departs by as much as 300–500 K from the adiabat [*Matyska and Yuen 2000; Bunge et al. 2001; Monnereau and Yuen 2002; Sleep 2003*].

Mantle non-adiabaticity points to a strong thermal gradient and a correspondingly high heat flux across the CMB [*Bunge 2005; Mittelstaedt and Tackley 2006; Zhong 2006; Lay 2008*], as large as 30 percent ( $\sim 10$  TW) of the total mantle heat loss. Thus, it is likely that bottom heating plays a more prominent role in the mantle general circulation than what is commonly inferred from arguments based on the dynamic topography over hotspots [*Davies 1988; Sleep 1990*]. It is therefore important to study the nature of heterogeneity in global mantle circulation models (MCM) when strong core heating is present. Of course, mantle heterogeneity modeled by geodynamicists must be compared to the seismic properties mapped by tomography. Both are related through the material properties of mantle mineralogy. In this respect, however, interpretations have remained limited as the trade-offs between thermal and chemical effects have not allowed an unequivocal identification of the cause of heterogeneities both for the upper [*Cammarano et al. 2003*] and the lower mantle [*Deschamps and Trampert 2004; Mattern et al. 2005; Matas et al. 2007*].

In this study, we test in a forward modeling approach whether strong core heating results in seismic heterogeneity compatible to observations in spectral characteristics and magnitude. To keep things simple, and to isolate the effects of core heating, we focus our attention on isochemical global mantle circulation. The pyrolite model [*Ringwood 1975; Irifune 1987*] is consistent with this choice.

We start this paper with a brief description of the computational methods and parameters employed. We next investigate the thermal heterogeneity of mantle flow with a substantial amount of core heat flux (as much as 12 TW), and isolate the effects of core heating from variations in the radial viscosity profile through simple end-member models. We explore the influence of thermal structure on corresponding heterogeneities in shear ( $v_s$ ) and compressional ( $v_p$ ) wave velocity, which we compare to tomographic models directly and with statistical measures. For the conversion of temperatures into elastic parameters we take advantage of progress in mineral physics and use two recently published thermodynamic mod-

els of mantle mineralogy [*Piazzoni et al. 2007*; *Stixrude and Lithgow-Bertelloni 2007*], coupled to a model of shear moduli [*Stixrude and Lithgow-Bertelloni 2005*]. In both models, stable phase assemblages in the CFMAS (CaO – FeO – MgO – Al<sub>2</sub>O<sub>3</sub> – SiO<sub>2</sub>) system are computed by Gibbs Free Energy minimization. We refer to these models hereafter as PSBD and SLB, respectively.

In the analysis of seismic properties and their relation to temperature via a mantle mineralogy model one needs to pay special attention to the vigor of convection, as one must ensure that modeled temperature variations are consistent with temperature variations assumed in the underlying mineralogy. To this end, we capitalize on growing computational resources and employ new global mantle circulation models at very high numerical resolution. This allows us to approach for the first time the vigorous regime of global mantle flow and to construct its corresponding elastic structure. Our models do not preclude the existence of chemical variations, but they suggest that the large-scale elastic heterogeneity of the mantle can be understood in terms of isochemical whole mantle circulation with strong hot upwellings from the CMB.

## 1.2 Computational Methods, Boundary and Initial Condition

We compute global mantle flow with the parallel finite element code TERRA, which has been benchmarked [*Bunge 1996*] and described in detail before [*Bunge and Baumgardner 1995*; *Bunge et al. 1996, 1997*]. The code solves the momentum and energy balance at infinite Prandtl number (no inertial forces) in a spherical shell, with the inner radius being that of the outer core and the outer radius corresponding to Earth’s surface. The computational domain is discretized with a mesh derived from the regular icosahedron, providing almost equidistant grid spacing throughout the mantle. A key difference to earlier studies [e.g., *Bunge et al. 2002*] is the very high resolution of the mesh with more than 80 million finite elements. The models are implemented on 128 cores of a topical compute cluster dedicated to large-scale geophysical modeling [*Oeser et al. 2006*]. The horizontal resolution is 30 km at the outer surface, and decreases to half that value at the CMB, while a uniform radial grid spacing of 25 km is applied throughout the shell. This fine discretization allows us to explore large-scale mantle flow at earth-like convective vigor and to employ a thermal Rayleigh number of  $10^9$  based on internal heating; that is, we are able to resolve a characteristic thermal boundary layer thickness on the order of 100 km, comparable to that of oceanic lithosphere.

Our circulation models incorporate mantle compressibility effects in form of the anelastic liquid approximation [*Jarvis and McKenzie 1980*; *Glatzmaier 1988*], and the radial variation of state variables is represented through a Murnaghan

equation of state [Murnaghan 1951] with parameter values identical to [Bunge *et al.* 2002]. We apply a thermal conductivity of  $3.0 \text{ W m}^{-1} \text{ K}^{-1}$  and an internal heating rate of  $6.0 \times 10^{-12} \text{ W kg}^{-1}$  throughout this study, roughly the chondritic value [Urey 1956]. Thermal boundary conditions are constant temperature at the surface (300 K) and the CMB. The latter is chosen such as to produce models with weak or strong core heat flux (see section 1.2.1). Mechanical boundary conditions are always free-slip (no shear-stress) at the CMB, while velocities are specified at the surface according to a widely adopted plate motion history model [Lithgow-Bertelloni and Richards 1998] that spans the past 120 million years (Ma). Meteorologists refer to this approach as *sequential* data-assimilation [see Talagrand 1997, for a review].

The high numerical resolution in our models requires an interpolation of all plate boundaries between successive plate stages, similar to Steinberger [2000], to avoid unrealistic separation of slab fragments. The interpolation is performed at 1 Ma intervals and involves geometric, but no geologic considerations. For this, we created a set of 120 plate configurations based on the eleven plate stages of Lithgow-Bertelloni and Richards [1998] while keeping their corresponding set of eleven Euler poles.

The large convective vigor in our models has the effect that the RMS surface velocity obtained from an independent set of free convection simulations (with no imposed plate motion) approaches earth-like values (about 5 cm/yr). This remarkable observation allows us to keep time identical to Earth time in all simulations, and to avoid scaling the assimilated plate velocities to lower values.

A general problem in mantle circulation modeling is the choice of an initial condition. This choice is rather arbitrary, as the structure of the mantle sometime in the past is principally unknown. Here, we follow the philosophy of Bunge *et al.* [1998, 2002] and approximate the unknown initial conditions of mid-Cretaceous mantle heterogeneity by running our models with global plate configurations fixed to the oldest available reconstructions at 120 Ma ago until they reach a thermal quasi steady-state.

Finally, the temperature field of the MCMs is post-processed and mapped to seismic velocities using the two thermodynamically self-consistent models of mantle mineralogy, PSBD and SLB, mentioned in section 1.1. In this simple approach, phase transitions of upper mantle minerals are therefore incorporated in our elastic models, even though their dynamic effects on the flow are not included in the calculations.

### 1.2.1 Model Setup

We focus on four mantle circulation models (M1–M4) and explore variations in the amount of bottom heating and the radial viscosity structure, while keeping all other model parameters constant (see Table 1.1). Our radial viscosity profiles account for three distinct layers (which we identify with the lithosphere, the upper

and the lower mantle, respectively) separated at 100 km and 660 km depth. These are inferred from geoid [e.g., *Hager and Richards 1989*] and post glacial rebound studies [*Paulson et al. 2007*] as a first-order rheological stratification of Earth’s mantle. Each model includes a relatively strong lithosphere, where the viscosity is  $10^{23}$  Pa.s. The upper mantle viscosity in model M1 is  $10^{21}$  Pa.s, the Haskell value [see *Mitrovica 1996*], and increases by a factor of 100 in the lower mantle. We ease the notation and index our model viscosities to the Haskell value, which we denote as “1”. Thus, the viscosity profile of M1 is 100, 1, 100 for the lithosphere, the upper and the lower mantle, respectively. A modest CMB heat flux of 1.5 TW (around 5% of the total surface heat flow) is accomplished by setting the CMB temperature to 2900 K.

The viscosity profile of M2 is identical to M1, but we impose a much higher core heat flux of 12 TW (roughly 35% of the surface heat flow) by setting the CMB temperature to 4200 K. This makes M1 and M2 end-members in terms of core heating with Urey numbers (the ratio of internal heating to total surface heat loss) of 0.95 and 0.65, respectively. M3, to which we ascribe a viscosity profile of 100, 0.5, 100, in effect explores the influence of a mechanically weaker upper mantle (relative to M1 and M2) and a correspondingly higher upper/lower mantle viscosity jump. A core heat flow of 9 TW (roughly 25% of the surface heat flow) is accomplished by setting the CMB temperature to 4000 K. M4 (with a profile of 100, 0.5, 50) reduces the overall mantle viscosity relative to M1, and moves the upper/lower mantle viscosity jump to 450 km depth. The depth and magnitude of the viscosity contrast between upper and lower mantle is not well known. We therefore chose to test a shallower depth in combination with the reduced overall viscosity in M4. A core heat flux of 10 TW (around 30% of the surface value) results from a CMB temperature of 3500 K in this case. Note that M4 produces a heat flow comparable to M2 and M3 despite its lower CMB temperature. This is a consequence of the reduced viscosity and the correspondingly more vigorous convection in this model. Together, M1–M4 span a reasonable range of mantle viscosity and core heat flux values, which are summarized in Table 1.2.

## 1.3 Results

### 1.3.1 Lateral Thermal Heterogeneity

Figure 1.2 shows three-dimensional (3-D) views of the temperature distribution in M2. The four view angles are centered on the Atlantic, the Indian Ocean, and the western and eastern Pacific, respectively. The earth-like convective vigor produces a narrow, upper thermal boundary layer with a thickness of about 100 km, and correspondingly thin and elongated downwellings in regions of present day plate convergence (e.g., under the Marianna and Izu-Bonin subduction systems, the Sumatra and Tonga-Kermadec trench). Remnants of the Tethyan subduction



are visible in a broad upper and mid-mantle region under Eurasia. Subduction of the old Farallon plate is evident in the deeper mantle under eastern North America and under South America. In the lowermost mantle, prominent hot upwellings are located in the southeast Pacific and under southern Africa up to Europe and Iceland (see top panels in Fig. 1.2). While the upwellings are consistent with the dynamics of flow with strong core heat flux, their morphology and location are entirely due to the model initialization, since the available plate motion history is too short to affect the pattern of deep mantle heterogeneity (see *Bunge et al.* [2002] for a discussion, and *Torsvik et al.* [2008] for efforts to extend plate motion histories to longer time periods in the past).

A remarkable feature is the spontaneous emergence of the asthenosphere as a region of relatively uniform temperature with much less thermal heterogeneity (the thin, almost white band in the upper mantle in Fig. 1.2, bottom panels). Due to the lower viscosity in this layer, material flows laterally over considerable distance (see thermal upwelling under the East Pacific Rise which feeds a broad region of hot asthenosphere in the equatorial Pacific), and as a result thermal variations are effectively equilibrated. This agrees well with petrological studies, which infer only minor melting temperature variations beneath the global mid-ocean ridge system [*McKenzie and Bickle* 1988; *Presnall and Gudfinnsson* 2008].

Horizontal sections through M1 and M2 are shown in Figure 1.3. Columns one and two (from left to right) illustrate how thermal structure varies between models with high and low core heat flux. Starting from the top, at 100 km depth, cold downwellings dominate the thermal heterogeneity pattern, as noted before. Continental regions and the oldest parts of the oceans are also colder than average, while hot material beneath oceanic regions follows the global distribution of spreading centers. Slabs control the thermal structure also at 340 km depth. Deeper down at 800 km depth, prominent cold downwellings are located around the Pacific, but their position differs from shallower depth levels because they reflect earlier stages of plate subduction (e.g., cold material associated with subduction of the Farallon plate east of North America's West Coast, and remnants of the Tethys Ocean as a distinct cold feature beneath Africa, Arabia and India). A hot thermal anomaly in M2 is located in the southeast Pacific.

There is little overall change in the mid mantle, at 1450 km depth, except for the location of downwellings. Here, the Farallon slab lies east of North America, and remnants of subduction exist under central America. The feature with the largest thermal amplitude is a group of downwelling slabs corresponding to the broad collision of India and Eurasia. Cold material exists also under the north Pacific, which can be traced back to the convergence of the North American and Kula plate 50–70 Ma ago according to the reconstructions. Significant differences between M1 and M2 appear between 2000 km and the CMB. M2 is dominated by prominent hot upwellings under the South Pacific Ocean and (to a lesser extent) in the Indian Ocean, while cold material spreads laterally in both models as it approaches the lowermost mantle and the CMB. Near the CMB at 2800 km depth,

hot upwellings in M2 give rise to large lateral temperature variations, reaching maximum positive values of up to +1500 K (see also Figure 1.6), while in model M1 there are much smaller variations on the order of +200–250 K.

### 1.3.2 Radial Profiles of Temperature, $v_s$ , $v_p$ and Density

Figure 1.4a shows the averaged temperature profiles of models M1–M4 and a 1750 K reference adiabat. As expected, all geotherms are subadiabatic due to internal heating and are up to 350–550 K lower than the reference adiabat in the lowermost mantle (2500–2700 km depth).

Density profiles for M2 obtained in combination with the mineralogical models PSBD and SLB are shown in Figure 1.4b, together with the density profiles of PREM and AK135M [*Dziewonski and Anderson 1981*; *Kennett et al. 1995*]. We focus on M2 in this and the remaining subfigures, because the variability of 1-D profiles between the MCMs is small. Both mineral physics models predict similar densities in the upper 1200 km of the mantle. They also provide rather good estimates of depth and magnitude of the density jumps across the discontinuities, as well as a reasonable gradient in the transition zone.

Figure 1.4c shows the  $v_s$  profiles inferred from M2. Both profiles run virtually parallel in the transition zone and the lower mantle. However, model SLB gives S-wave velocities about 1.5–2% lower than model PSBD, the latter being in reasonable agreement with the seismic reference profiles. The gradient of  $v_s$  in the lower mantle is larger than observed for both models of mantle mineralogy. The predicted P-wave profiles (Fig. 1.4d) are also parallel in most of the mantle, but show exactly opposite characteristics to  $v_s$ . Model SLB now gives higher  $v_p$  values than PSBD and their gradients are again larger than for the seismic models. The fact that both mineral physics models predict parallel offset profiles in  $v_s$  and in  $v_p$  can be traced back to differences in their databases and demonstrates the need to reduce uncertainties in experimental values.

For both P- and S-wave velocities, the depth of the 410 km discontinuity is overpredicted using either of the mineralogical models. Together with the low values of the seismic velocities in the upper mantle, and assuming that pyrolite is a reasonable estimate of mantle composition, this indicates that the absolute temperatures may be overestimated.

Changing the average temperature profile may improve the fit to the seismic observations. We tested this in that we lowered the geotherm of M2 by 500 K resulting in a temperature profile with 1250 K footing temperature, but no change in slope compared to the original profile. A geotherm with footing temperature of around 1250 K (roughly 1000 °C) is unlikely in the Earth. Typical estimates derived from melting temperatures of basalts at mid-ocean ridges yield values of around 1350 °C or roughly 1600–1650 K, which is much closer to our original geotherm. The  $v_s$  profile from the artificially lowered geotherm using model SLB falls closer to the values of PREM and AK135M, but is still too low by 0.3–0.5%

in the lower mantle. At the same time, density and  $v_p$  are larger than the seismic reference values. We note that the upper mantle temperature in our simulations depends mostly on the viscosity structure of the lithosphere (i.e., both absolute values and thickness), which leaves room for lowering the overall temperatures in future simulations and to bring our predicted 1-D profiles closer to observations. However, since this study focuses on 3-D variations we do not intend to fit seismic reference profiles.

### 1.3.3 Thermal vs. Elastic 3-D Heterogeneity

We return to Figure 1.3 where relative variations in S- and P-wave velocity derived from model M2 are shown in columns three and four. The elastic heterogeneity is inferred by converting absolute model temperatures to absolute values of S- and P-wave velocity using the mineralogical model SLB for a pyrolite composition. Relative variations are then computed with respect to the mean seismic velocity at each depth. The main effect of the conversion is to amplify heterogeneity in the uppermost mantle, while there is a trend toward less heterogeneity with depth. Note that shear velocity variations are much stronger throughout the mantle than variations in compressional velocity.

#### Spectral Characteristics

Spectral heterogeneity maps (SHM) [*Jordan et al. 1993*], which are contour plots of spectral amplitude *vs.* depth, for all four MCMs are shown in Figure 1.5. In the following, we consider temperatures together with shear wave velocities based on the mineralogical model SLB. Radial profiles of the root-mean-square (RMS) power of the spherical harmonics expansion are also shown. Spectral power  $\sigma_l$  per degree  $l$  is computed at each depth level and for spherical harmonics degrees  $l = 1, \dots, 20$  by [*Dahlen and Tromp 1998*, B.8]

$$\sigma_l = \sqrt{\frac{1}{2l+1} \left[ a_{l0}^2 + \sum_{m=1}^l (a_{lm}^2 + b_{lm}^2) \right]}, \quad (1.1)$$

where  $a_{lm}$  and  $b_{lm}$  are the coefficients of the expansion and the RMS power is given by:

$$\delta\hat{v} = \sqrt{\frac{1}{\sqrt{4\pi}} \sum_{l=1}^{l_{max}} (2l+1)\sigma_l^2}. \quad (1.2)$$

Spectral power of thermal heterogeneity (Fig. 1.5a–d) is concentrated in the upper and lower thermal boundary layers of all MCMs, i.e., in the lithosphere and

in the lowermost mantle. Thermal variations in the lithosphere exist on a broad range of spatial scales as indicated by strong spectral power in all spherical harmonic degrees. In the low-viscosity upper mantle, by comparison, there is much less thermal heterogeneity. The strength of heterogeneity increases again at the top of the lower mantle due to the higher viscosity there. Starting at around 750 km depth, pronounced heterogeneity at the largest length scale (spherical harmonic degree two) exists in all models, with a further increase in heterogeneity amplitude from the mid mantle (1500 km) downward. This low order pattern is due to the dominant long wavelength planform of the oldest stages of assimilated plate motion history from 80 to 120 Ma ago, and reflects the combined effects of plate motion and viscosity stratification [*Bunge and Richards 1996*]. In the deepest mantle, and approaching the lower thermal boundary layer, heterogeneity can also be found in higher degrees. Note that the weak mid mantle heterogeneity in M4 (Fig. 1.5d) reflects the lower viscosities in this model. The overall distribution of heterogeneity, with maxima near the top and bottom thermal boundary layers, is also reflected in the radial profiles of RMS spectral power in all four MCMs.

The spectral heterogeneity maps for  $v_s$ , displayed in Figures 1.5e–h, look rather different compared to those of temperature, which reveals the strong effects of mantle mineralogy. They only show similarities in the overall characteristics (strong heterogeneity in the lithosphere and the lowermost mantle, dominated by long wavelength structure). The biggest difference in spectral power between  $v_s$  and thermal variations exists in the upper mantle, where narrow bands of spectral power up to degree 20 are visible for  $v_s$ . These correspond to the major phase transformations in the transition zone at 410 km, 520 km and 660 km depth. Variations in the amount of CMB heat flow influence the power distribution less than the differences in radial viscosity profiles (compare e.g., Figs. 1.5e,f and h), as the radial viscosity structure primarily controls the speed of flow and therefore the depth of subducted material. A higher CMB heat flux instead increases the amplitude of lower mantle heterogeneity, e.g., more heterogeneity is present in the lowermost mantle in model M2 compared to M1 and also in higher degrees.

The difference in spectral heterogeneity between temperature and shear wave velocity in the upper mantle can be explained by the increased sensitivity of shear wave velocity to temperature at the upper mantle discontinuities. This sensitivity is the result of two combined effects: On the one hand temperature directly influences the elastic properties of a fixed phase assemblage. On the other hand, temperature also affects the stable phase assemblage, which in turn strongly changes the elastic properties of the bulk rock [*Ricard et al. 2005*; *Stixrude and Lithgow-Bertelloni 2007*]. The latter effect is most significant in the upper mantle, leading to the fine scale heterogeneity observed in  $v_s$  in the transition zone.

The change in pattern between thermal and elastic spectral heterogeneity suggests caution in the geodynamic interpretation of tomographic models ( $v_s$  or  $v_p$ ). For example, from the spectral characteristics of  $v_s$  in Figures 1.5e–h

one may argue for a change in the convective style between the upper and lower mantle. The underlying thermal variations in the geodynamic models, however, show an increase in the power of heterogeneity from the upper to the lower mantle, opposite to what is seen in the elastic parameters. As noted before, this is the result of an increase in viscosity at the upper mantle/lower mantle boundary, which however, does not inhibit mass exchange.

### Amplitude Distributions of 3-D Heterogeneity

Histograms of variations in temperature and shear wave velocity are shown in Figure 1.6. We contour the total number of model grid points at any given depth (y-axis) as a function of their temperature or shear wave anomaly (x-axis) relative to the horizontal mean. We consider thermal heterogeneity first (Figs. 1.6a–d) and note that the largest number of model grid points in each depth has temperatures near the mean radial value, as expected for vigorous convection. In other words, thermal anomalies are small nearly everywhere, as heat transport is dominated by advection outside the thermal boundary layers. All histograms reveal maximum cold thermal anomalies (slabs) on the order of  $-1000$ – $1500$  K at all depth levels, which correspond to the temperature drop across the upper thermal boundary layer, as expected. The minor fluctuations with depth reveal transient features in the subduction history; that is, these changes can be attributed to variations in the amount of subducted slab material at different plate tectonic stages.

The most pronounced difference between the MCMs occurs for hot anomalies, i.e., plumes rising from the thermal boundary layer above the CMB. Model M1 with a weak lower thermal boundary layer and a correspondingly low core heat flux is characterized by low amplitude positive temperature variations with magnitudes less than  $+500$  K. In contrast to that, the MCMs with high CMB heat flow (M2–M4) show large positive values in the lower mantle and a strong decrease of plume excess temperatures as the material rises adiabatically in the otherwise subadiabatic mantle. In these models, hot (positive  $dT$ ) anomalies are reduced from around  $+1000$ – $1500$  K at the CMB to  $+200$ – $300$  K in the upper mantle.

All histograms are asymmetric with respect to their bounds in most of the depth levels. Moreover, they show a strong increase in variance and spread with depth in the lower mantle, except for M1. Thermal heterogeneity of all models is characterized by substantial negative skew in the upper mantle outside the lithosphere, and only models with high CMB flux show a gradual change to positive skewness in the lowermost mantle and a nearly bi-modal distribution, there.

Similar to the spectral heterogeneity maps, the histograms for shear wave velocity in Figures 1.6e–h differ considerably from those of temperature. Most of

the difference is due to the general decrease in sensitivity of shear wave velocity to temperature with depth [Trampert *et al.* 2001; Cammarano *et al.* 2003; Goes *et al.* 2004; Stixrude and Lithgow-Bertelloni 2007]. This can be seen, for example, when comparing maximum positive temperature variations in Figure 1.6b to the corresponding shear velocity anomalies in Figure 1.6f. While the hot temperature anomalies increase strongly with depth in the lower mantle, their respective S-wave perturbations remain nearly constant. In consequence, the largest spread of S-wave perturbations is located in the upper mantle exceeding values of 8% on the positive side. Strong variations in the transition zone directly show the influence of phase changes and the corresponding changes in elastic parameters.

Moreover, the comparison of thermal and seismic heterogeneity reveals the non-linearity introduced through the mineralogical model, which has also been observed by Goes *et al.* [2004]. Positive temperature variations lead to larger variations in  $v_s$  than negative variations (e.g., for model M2:  $\frac{dlnv_s}{dT} = -5.1 \times 10^{-5}$  at  $\sim 2500$  K vs.  $-4.0 \times 10^{-5}$  K $^{-1}$  at  $\sim 1500$  K in the upper part of the lower mantle; and  $-2.9 \times 10^{-5}$  at  $\sim 3000$  K vs.  $-2.5 \times 10^{-5}$  K $^{-1}$  at  $\sim 2000$  K in the lowermost mantle, respectively). This non-linearity results in a modification of the spread and asymmetry in the histograms. Model M2 shows the strongest asymmetry in the lowermost mantle with values of more than  $-4\%$  compared to  $+2\%$  on the positive side. Especially the large slow values exceeding  $-4\%$  are remarkable. In contrast to that, the small positive thermal variations in model M1 result in much smaller negative  $v_s$  perturbations of around  $-1\%$ . This marks the significant difference to models with strong core heating. In addition, the latter are characterized by a change from positive skewness in the upper part of the lower mantle to negative skewness near the CMB. Furthermore, they have a peak at fast seismic velocities in the lowermost mantle and show a strong increase of variance with depth.

## 1.4 Comparison of Modeled Heterogeneity to Tomography

### 1.4.1 Comparison of Spectral Characteristics

Figure 1.7 shows the spectral characteristics of the four tomographic models from Figure 1.1. In all models, heterogeneity is concentrated in the lithosphere, the upper mantle and the lowermost lower mantle. The significant power in higher degrees close to the surface and the CMB indicates considerable small scale heterogeneity. Note also that model PRI-S05 was built using body wave data only [Montelli *et al.* 2006], which may be the reason for the lower spectral heterogeneity in the lithosphere compared to the other models. All spectra are “red” and generally show a strong degree two signal in most of the lower mantle (S20RTS, TX2007 and HMSL-S06). Heterogeneity is weakest in the mid mantle

and all models show a change in spectral power from the transition zone into the lower mantle.

Our isochemical mantle circulation models are in good agreement with these characteristics, which also show a concentration of heterogeneity close to thermal boundary layers and a red spectrum. The latter results from the combination of large-scale plate motion and a high viscosity lower mantle [Bunge and Richards 1996]. The MCMs also display a change in the spectra of elastic heterogeneity from the upper to the lower mantle. As discussed in section 1.3.3 this is due to the mineralogical properties of the mantle.

### 1.4.2 Comparison of Amplitudes

In Figure 1.8, we plot histograms of the tomographic S-wave models. Note that they show considerable differences among each other, especially in the spread of amplitudes. Models S20RTS and TX2007 have much smaller amplitudes in almost all depth levels compared to models HMSL-S06 and PRI-S05, which may reflect differences in tomographic resolution due to different inversion procedures or data sets used. The variability of the maxima in the lower mantle, which however is less than in our MCMs, may be a combination of transient geodynamic features, as well as artifacts from the inversion. In all histograms, the peak deviates from the mean value in certain depths, most strongly so in the lowermost mantle where all models show a shift to positive variations. Furthermore, the variance increases close to the CMB. Interestingly, extreme values are asymmetric in the lowermost mantle, with negative  $v_s$  perturbations of up to  $-4\%$  compared to  $+2\%$  on the positive side (especially in models HMSL-S06 and PRI-S05). At the same time, the histograms have negative skewness there, as opposed to the positive skewness in the upper part of the lower mantle, a feature that has been noted also by Yanagisawa and Hamano [1999] for other S-wave velocity models. Similar to all histograms is that the largest perturbations occur in the lithosphere and upper mantle which is consistent with the high spectral power observed in this depth range.

The geodynamic models with strong core heating show the same marked asymmetry in the lowermost mantle with negative  $v_s$  anomalies of up to  $-4\%$ , while the values of around  $-1\%$  in model M1 are much lower than observed. Moreover, they also display a change in skewness from positive to negative throughout the lower mantle and a peak at positive values close to the CMB supporting the notion that the mantle is heated substantially from below. Furthermore, the skewness pattern indicates that thermal structure in the mantle is dominated by cold downwellings (i.e., slabs) down to 1500 km, and very hot active upwellings at greater depths. Yanagisawa and Hamano [1999] have argued along similar lines based on 2-D convection simulations in a Cartesian setup and a direct comparison of resulting temperatures to tomographic shear wave models. The results in

Figure 1.6 show that this conclusion is largely independent of the details of the radial viscosity structure.

One robust property inferred from tomography is an increase in the RMS amplitude of seismic heterogeneity below 2000 km depth, often taken as an indication for deep mantle chemical heterogeneity. In Figure 1.9a and 1.9b we plot RMS profiles of the four tomographic S-wave models and six additional P-wave models, all of which show the largest RMS amplitudes in the upper 200 km of the mantle and a gradual increase from a minimum in the mid-mantle to values of around 1% for  $v_s$  and 0.3–0.5% for  $v_p$  close to the CMB. For ease of comparison to our MCMS, we construct upper and lower bounds from the tomography profiles by taking the maximum and minimum RMS values of all tomographic models in each depth (black dashed and dash-dotted lines, respectively in Figs. 1.9c and 1.9d). In most of the mantle, the geodynamic RMS profiles of  $v_s$  and  $v_p$  lie within these bounds. Only model M2 gives larger values in the lowermost mantle for both seismic velocities. At the transition zone discontinuities, the RMS amplitudes of the MCMS show strong variations and large values as a consequence of the complex sensitivity of  $v_s$  to temperature, as noted before. Lower values and less variation in the tomographic models may be related to vertical smearing of heterogeneity from the transition zone into the uppermost lower mantle, where the geodynamic models show values at the lower bound.

## 1.5 Discussion

We have investigated the thermal and elastic structure of high-resolution mantle circulation models and find that whole mantle flow with strong core heating is compatible with a variety of quantitative measures inferred from tomography: histograms, RMS amplitudes, and spectral power of variations in shear wave velocity. In particular, the hot lower mantle thermal anomalies on the order of 1000 K and the corresponding reduction in shear wave velocity of up to  $-4\%$ , which we infer using published models of mantle mineralogy [*Piazzoni et al. 2007*; *Stixrude and Lithgow-Bertelloni 2005, 2007*], agrees remarkably well with shear wave anomalies mapped in low seismic velocity regions of the deeper mantle (see histograms in Figures 1.6e–h and 1.8). Apart from the isochemical, pyrolitic nature of our models, we have made three basic assumptions in the construction of global geodynamic mantle heterogeneity: 1) a large-scale flow structure related to past plate motion, 2) a radial viscosity profile that agrees with post-glacial rebound and geoid observations, and 3) a significant vertical temperature change across the CMB of  $\sim 1000$  K corresponding to a large core heat flow of 9–12 TW.



### 1.5.1 Amplitudes of Seismic Heterogeneity and Plume Excess Temperature

While the first two assumptions are reasonably well agreed upon by geodynamacists, the third assumption requires careful consideration, being promoted, as it is, by a number of recent studies: *van der Hilst et al.* [2007], for example, find a CMB temperature of  $3950 \pm 200$  K from inverse scattering of core-reflected shear waves (ScS). CMB temperature values between 3500 and 4000 K and a large jump of 1000–1500 K across D'' are also suggested by *Steinberger and Holme* [2008], who fit models of instantaneous mantle flow, which are based on density variations derived from tomographic shear wave models, to the geoid and observations of CMB excess ellipticity and topography. High-pressure experiments on the melting temperature of iron alloys also point to a high CMB temperature of  $4000 \pm 200$  K and a correspondingly large temperature drop on the order of 1000 K at the base of the lower mantle as reviewed by *Boehler* [2000]. These results are further supported by first-principle calculations of the elastic parameters and melting curve of iron under core conditions. When combined with seismic constraints the material simulations place estimates of the inner-core boundary (ICB) temperature at 5400–5700 K [*Steinle-Neumann et al.* 2001; *Alfè et al.* 2002]. Correcting for the adiabatic gradient through the outer core this translates to a CMB temperature of about 4000 K and a high excess temperature of deep mantle upwellings [*Alfè et al.* 2007].

The near surface excess temperature of mantle upwellings by comparison is rather small, ranging between +200 and +300 K [*Schilling* 1991]. The much larger excess temperatures in the deeper mantle, however, can be gleaned from two thermodynamic considerations: First, as noted before, internal heating in combination with the slow overturn of the mantle lowers the geotherm by 300–500 K compared to an adiabat [*Jeanloz and Morris* 1987; *Matyska and Yuen* 2000; *Bunge et al.* 2001; *Monnereau and Yuen* 2002; *Sleep* 2003; *Mattern et al.* 2005]. The temperature distribution in plumes instead is nearly adiabatic, as they rise relatively quickly through the mantle, on a time scale on the order of 100 Ma. The net effect is a systematic increase of plume excess temperature by about 300 K as one moves deeper into the mantle [*Bunge* 2005]. The second consideration follows from the adiabatic gradient being proportional to temperature. This implies a steeper thermal gradient in plumes relative to normal mantle. For example, an isentrope tied to a footing temperature of 2000 K undergoes a temperature increase with depth nearly twice that of an adiabat footed at 1000 K. Consequently, the adiabatic temperature increase in plumes exceeds that of normal mantle by about 300 K [see *Piazzoni et al.* 2007, Fig. 7]. Combining these two effects suggests that the near surface excess temperature of mantle plumes of around +300 K translates into hot thermal variations on the order of +1000 K in the lowermost mantle, entirely consistent with a strong thermal gradient across the CMB.

The dominance of thermal variations on seismic heterogeneity contrasts with recent interpretations of seismic tomography [*Su and Dziewonski 1997; Masters et al. 2000; Ishii and Tromp 1999; Trampert et al. 2004*]. For example, *Trampert et al. [2004]* have inverted normal mode splitting observations and surface wave data for variations in temperature, perovskite and iron content. Using a probabilistic approach, they find a large likelihood that density variations in the lowermost mantle are dominated by chemical rather than thermal anomalies. However, their inferred temperature variations of  $\pm 300$  K, and in particular the low excess temperature of hot upwellings in the lowermost mantle, are difficult to understand in light of the above considerations. Our MCMs with strong core heat flux (M2–M4) instead suggest that one can account for the observed amplitudes of seismic heterogeneity in the lowermost mantle by thermal variations and their effects on elasticity. The high plume excess temperatures in the deeper mantle agree with tomographic studies showing a depthwise increase in heterogeneity strength of low seismic velocity anomalies [*Boschi and Dziewonski 1999; Romanowicz and Gung 2002; Montelli et al. 2004*], and are probably related to independent evidence for ultra-low seismic velocities at the CMB [*Garnero 2000*], as these temperatures approach the lower mantle solidus. A thermal interpretation of lower mantle seismic velocity anomalies is also favored by recent joint inversions of seismic data, free-air gravity, dynamic topography and excess ellipticity of the CMB [*Simmons et al. 2007*].

Experimental [*Andrault et al. 2001; Mao et al. 1991; Zhang and Weidner 1999*] and first-principle results [*Kieffer et al. 2002*] demonstrate that compositional variations strongly affect the volume and shear modulus of perovskite. Similarly, one observes in (Mg,Fe)O magnesio-wüstite that an increase in iron content significantly lowers the shear modulus [*Lin et al. 2006*, and references therein]. These findings bear on our models, since Figures 1.6 and 1.9 show that the strong positive thermal anomalies, which we infer from the MCMs, imply shear wave anomalies that match and in some cases (M2) exceed the bounds of lower mantle heterogeneity mapped by seismic tomography. A further increase in heterogeneity by further reducing the shear wave velocities would follow, if one assumed iron enrichment in the low velocity regions [*Wang and Weidner 1996; Jackson 1998b*], unless one attributes much lower excess temperatures to them [*Trampert et al. 2004*].

We note, however, that tomographic studies in general suffer from limited resolving power, only providing a filtered view into Earth’s mantle. Imaged velocity anomalies and inferred temperature variations may thus be underestimated. Further comparisons are therefore needed to explore the effects of “tomographic filtering”, which are likely to reduce the amplitudes of geodynamically predicted heterogeneity [*Mégnin et al. 1997; Davies and Bunge 2001; Bunge and Davies 2001*].

### 1.5.2 Strong Core Heat Flux

Beyond the considerations on seismic heterogeneity, our results also bear on CMB heat flux. The strongly bottom heated MCMs (M2–M4) predict a substantial core heat loss in the range of 9–12 TW, considerably higher than the heat transport commonly inferred from hotspots [*Davies 1988; Sleep 1990*]. A number of geodynamic studies have recently supported a significant core heat loss to overcome problems of insufficient internal mantle heat sources [*Kellogg et al. 1999*], and to satisfy the power requirements of the geodynamo [*Glatzmaier and Roberts 1995; Kuang and Bloxham 1997*] and estimates of the thermal history of the core [*Buffett 2002; Nimmo et al. 2004*]. In particular, *Gubbins et al. [2004]* infer a large passive heat transport along the outer-core adiabat of 9 TW from compressible two-component core convection. Additional heat is released from ohmic dissipation in the generation of the magnetic field, for which our current limited understanding provides estimates ranging from 0.1 to 3.5 TW [*Roberts and Glatzmaier 2000; Buffett 2002; Roberts et al. 2003; Labrosse 2003; Gubbins et al. 2003; Christensen and Tilgner 2004*]. The total core heat loss may thus approach 9–12 TW. Specifically, this implies a core contribution to the overall mantle heat budget in the range of 30–40%, and a Urey number of 0.6, much closer to estimates from geochemistry of 0.3–0.5 [*McDonough 2007*] than classic geodynamical values of  $\sim 0.9$ –0.95 [*Turcotte and Schubert 2001*]. Moreover, a substantial core heat loss is also favored by *Nolet et al. [2006]* and would at least in part address the difficulty raised by missing heat production in the mantle [*Urey 1956; Jochum et al. 1983*].

### 1.5.3 Plume Morphology and Lacking Information on the Initial Condition

An important argument in support of chemical heterogeneity is the morphology, or shape, of deep mantle upwellings, taken either from direct observations of seismic data [*Ni et al. 2002*], or from laboratory [*Jellinek and Manga 2004*] and numerical studies [*McNamara and Zhong 2004b*]. Unfortunately, the shape of lower mantle structure is poorly constrained by mantle circulation models relying on the sequential assimilation of past plate motions [*Bunge et al. 2002; McNamara and Zhong 2005*]. The difficulty arises from lack of information on the initial condition [*Bunge et al. 2003*] and uncertainties in models of plate motion history, which grow larger as one goes back in time. As an example of the latter, we compare Figures 1.3 and 1.1. The hot upwelling structure under southern Africa is predicted too far south by our MCM approach (see also the cold downwelling structure under Northeast Africa in Figs. 1.2 and 1.3), probably as a result of uncertainties in the convergence history of the African and Eurasian plates. This interpretation is supported by the recent reconstructions of *Müller et al. [2008]*, which place the convergent margin farther north than the plate motion history

used in our study [*Lithgow-Bertelloni and Richards 1998*]. Efforts are currently underway to extend models of past plate motions further back in time [*Torsvik et al. 2008*], and to explore adjoint techniques in geodynamic simulations to better constrain the temporal evolution of the mantle [*Bunge et al. 2003*; *Ismail-Zadeh et al. 2004, 2007*; *Liu and Gurnis 2008*].

## 1.6 Conclusions

We have presented global models of thermal and elastic mantle heterogeneity derived from high-resolution mantle circulation modeling involving 80 million finite elements. Variations in seismic velocities are obtained by converting absolute temperatures into elastic heterogeneity using recently published thermodynamically self-consistent models of mantle petrology and elasticity. We find significant differences in the characteristics of thermal and seismic heterogeneity, which warrant a careful geodynamic interpretation of tomographic models. Most importantly, our models make a number of quantitative predictions for statistical properties such as spectral power, histograms and RMS amplitudes, all of which are found in good agreement with tomography. A key observation is the magnitude of lower mantle thermal anomalies (on the order of 1000 K). The corresponding strong reduction in shear wave velocity, which we infer for hot upwelling regions in our models, agrees well with the magnitude of shear wave anomalies mapped by tomography in low velocity regions of the deeper mantle.

Our results suggest that simple isochemical mantle circulation models are capable of explaining some first-order observations from tomography when combined with strong heat flux from the core on the order of 9–12 TW. This number is supported by many recent studies on core and mantle dynamics, related material properties, as well as by seismological observations. Uncertainties in plate tectonic reconstructions and the unknown initial condition of mantle general circulation, however, limit our capabilities of constraining the geographic pattern of heterogeneity in the lowermost mantle.

The models presented here may be improved in various ways. For example, updated models of plate motion history will help to better constrain the location and morphology of deeper mantle structure. Also, we have not included the effects of horizontal viscosity variations, which are particularly important in the lithosphere in generating shear localisation and plate like behavior through temperature dependent viscosities and plastic yielding [*Trompert and Hansen 1998*; *Richards et al. 2001*], although a combination of neotectonic and mantle convection modeling appears effective in modeling the complexities of plate motion [*Iaffaldano et al. 2006*; *Iaffaldano and Bunge 2008*].

Furthermore, the mineralogical models currently do not account for the potential presence of post-perovskite, thus limiting conclusions on structure in D". Moreover, we have also excluded any additional complexity arising from chem-

---

ical variations, choosing to study simple isochemical models first and to isolate thermal effects. Work by *Hutko et al.* [2008] and *Hernlund and Houser* [2008] suggests that at least part of the observed anti-correlation of  $v_s$  and  $v_\phi$ , which is difficult to explain from a uniform composition, could be related to the occurrence of post-perovskite. With respect to sharp gradients in seismic structures observed in the lower mantle, and the possibility to explain these by a purely thermal origin, our high-resolution MCMs with their strong lateral variations will have to be filtered to the resolution of tomography for further comparisons.

Finally, tomographic models as well have to be refined, especially in terms of resolving the amplitudes and gradients of heterogeneity. In this respect, various improvements in tomographic imaging techniques are currently investigated, such as finite frequency tomography including waveform amplitude information [*Sigloch et al.* 2008] or full waveform inversion using adjoint techniques [*Tromp et al.* 2005; *Fichtner et al.* 2006a,b].

## 1.7 Figures – Chapter 1

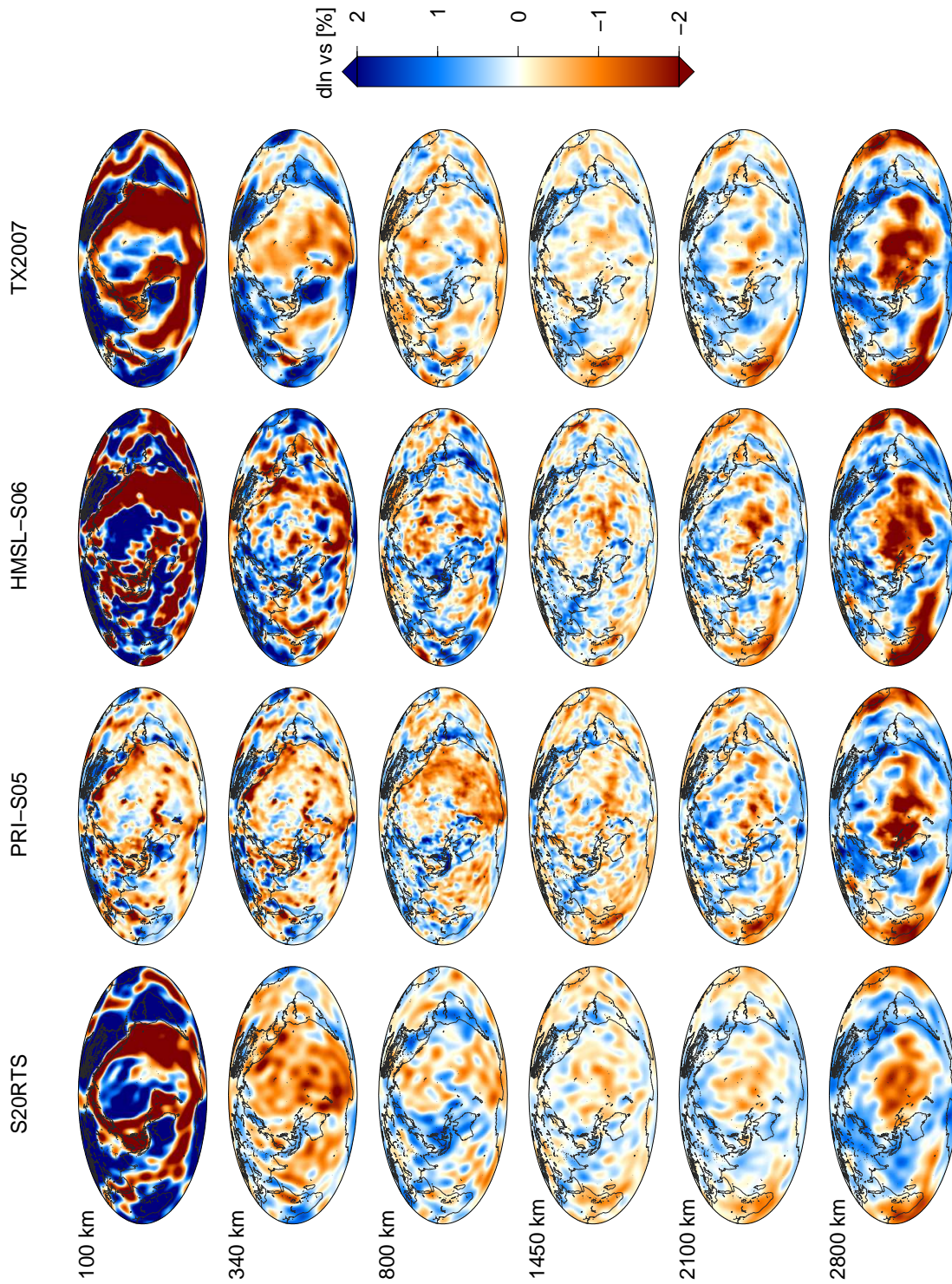


Figure 1.1: Depth slices through tomographic mantle models of shear wave velocity S20RTS [*Ritsema et al. 2004*], PRI-S05 [*Montelli et al. 2006*], HMSL-S06 [*Houser et al. 2008*], TX2007 [*Simmons et al. 2007*]. Variations in S-wave velocity are given relative to each corresponding 1-D radial seismic reference model. The color scale ranges from  $-2\%$  to  $+2\%$  as shown on the right. Heterogeneity is strongest in the lithosphere, the upper mantle and near the CMB. Note the dynamically important slow seismic velocity structures located under the Pacific and Africa in lowermost mantle (called “Large Low Velocity Provinces” or “superplumes”) and the ring of fast velocities around the Pacific.





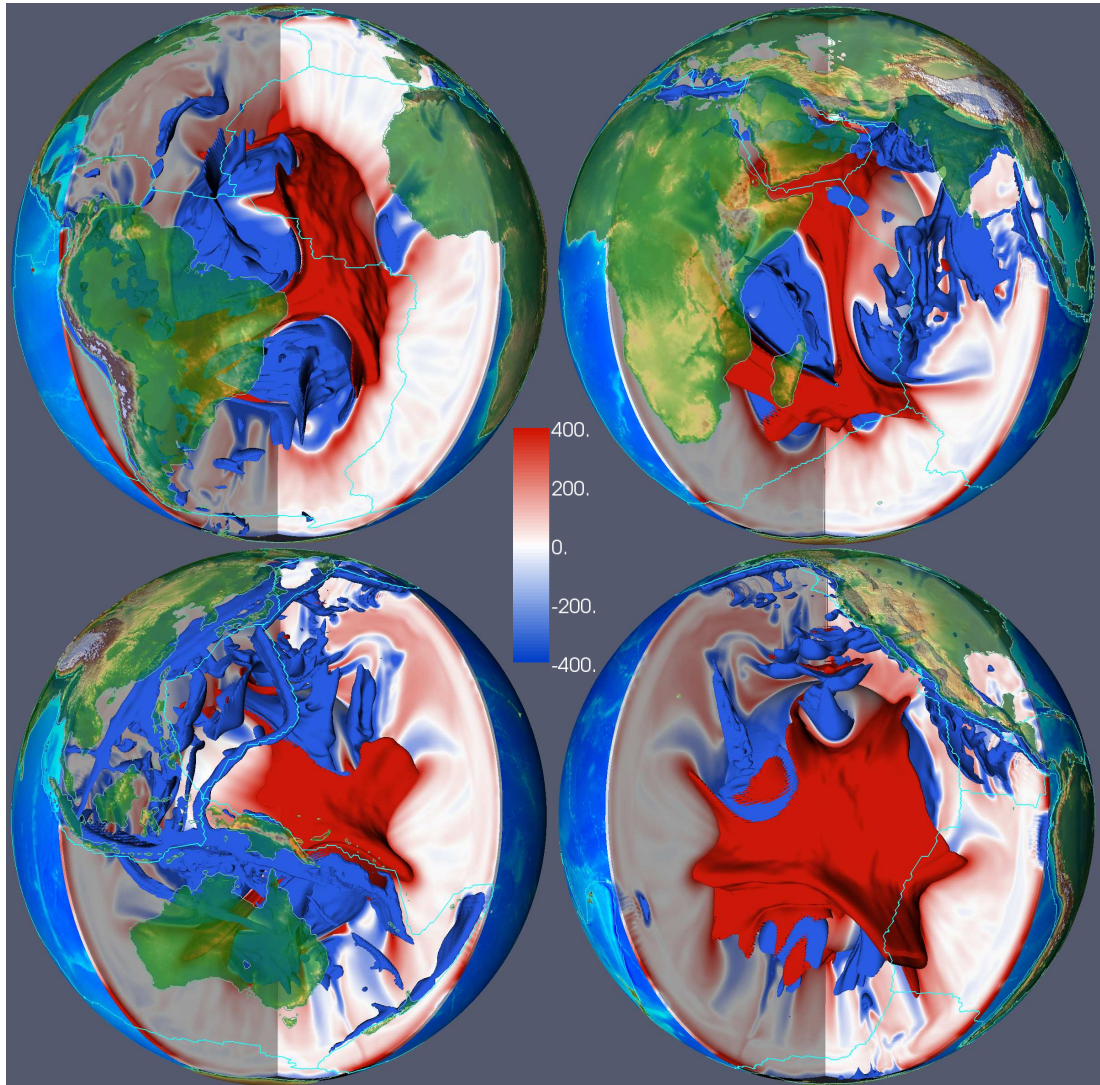


Figure 1.2: Three-dimensional representation of temperature variations in model M2 with strong core heat flux (see text). The four adjacent cross sections are centered on 35 (upper left), 125 (lower right), 215 (lower left) and 305 (upper right) degrees longitude. The color scale is saturated at  $-400$  K and  $+400$  K, and continents with color-coded topography and plate boundaries (cyan lines) are overlain for geographic reference. Isosurfaces of temperature are displayed for  $-600$  K and  $+400$  K. The  $+400$  K isosurface is clipped in the uppermost 500 km to allow views into the mantle underneath the mid-ocean ridge system, which spans large parts of the oceanic upper mantle. The reduced thermal heterogeneity in the upper mantle (thin, almost white band best visible in the views centered on 125 and 215 degrees longitude) is a consequence of the lower viscosity, there. Note also the prominent thermal upwelling in the Eastern and Central Pacific not far from the SOPITA anomaly identified on thermal and geochemical grounds by *Staudigel et al.* [1991].

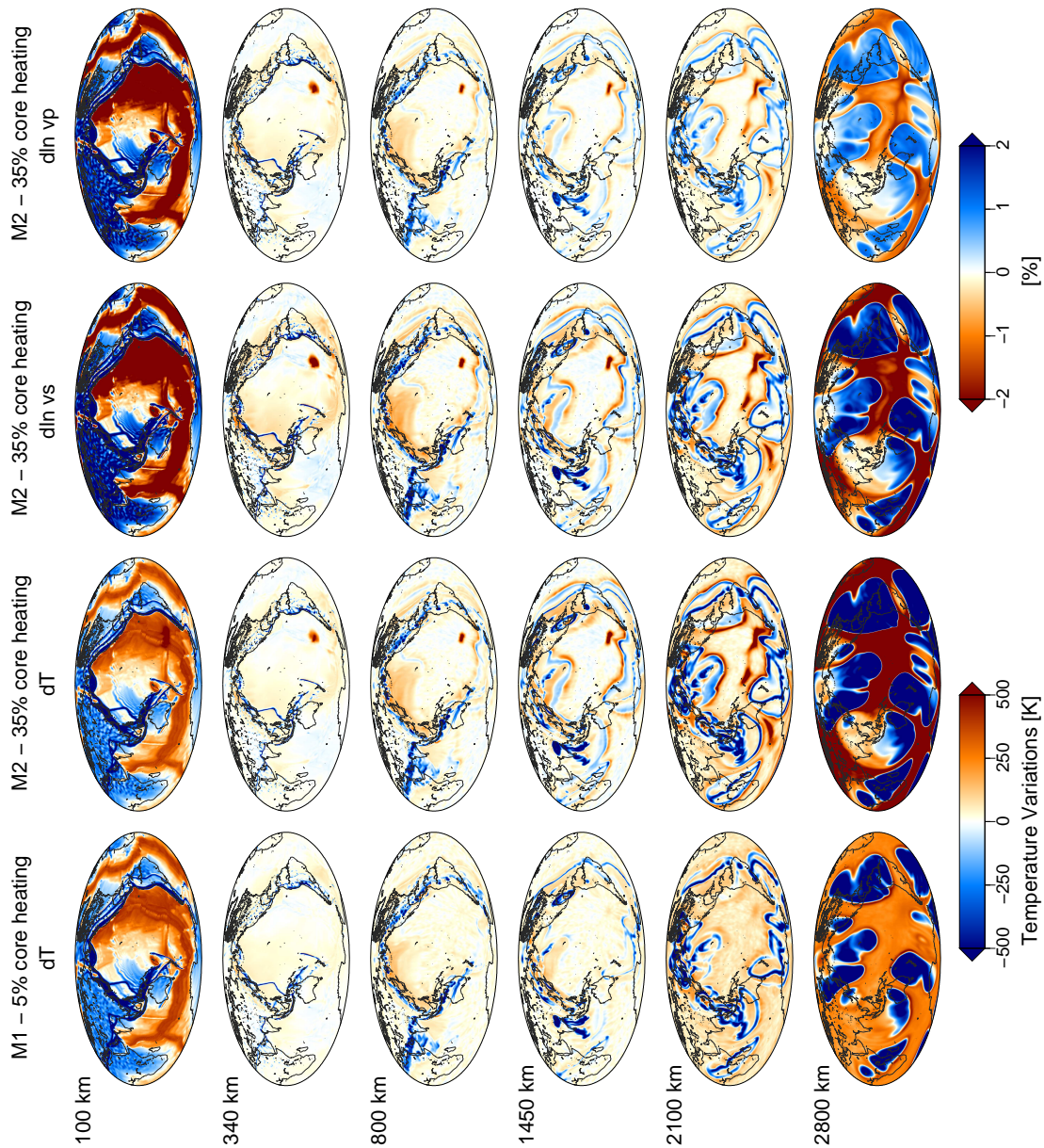


Figure 1.3: Depth slices through mantle circulation models M1 and M2 with weak and strong core heat flux, respectively. (left) Temperature variations in M1 and M2 and (right) elastic structure in M2 (strong core heating) for variations of shear, as well as compressional wave velocity relative to their radial average. Absolute values of seismic velocities are obtained from absolute values of temperature using the mineralogical model SLB [*Stixrude and Lithgow-Bertelloni 2005, 2007*].

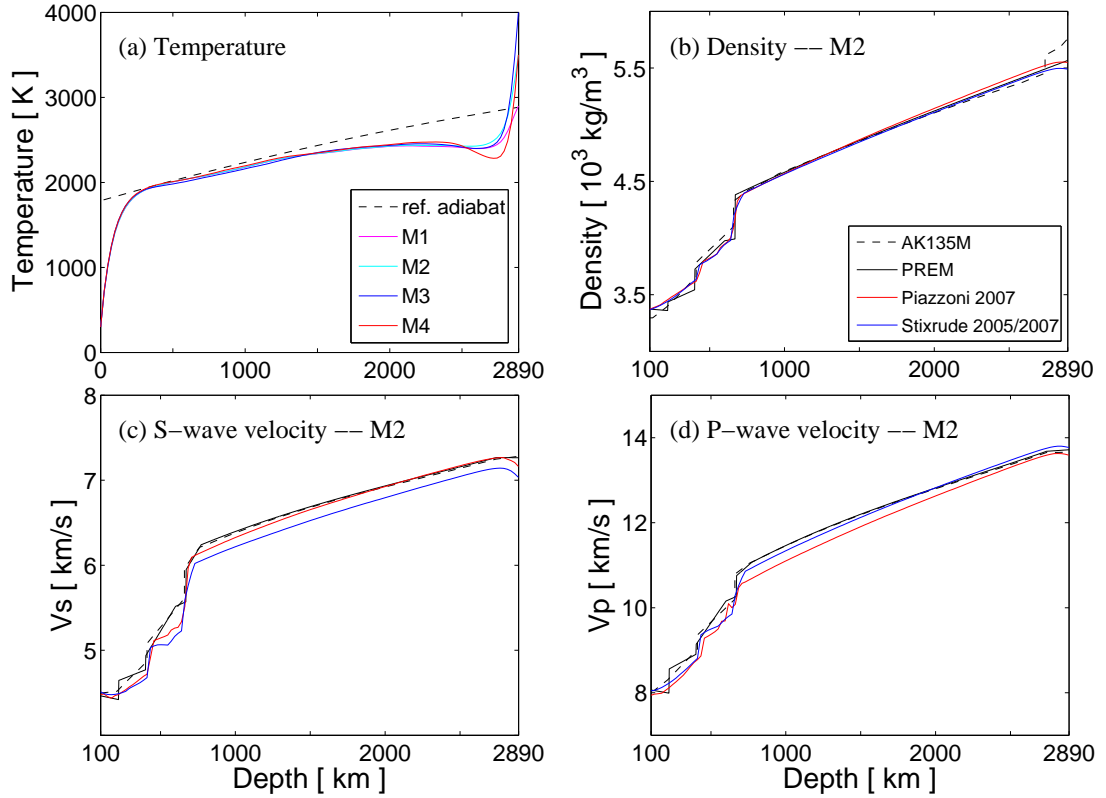


Figure 1.4: a) Temperature profiles of models M1–M4 together with the reference adiabat used in the simulations. Note that all profiles are subadiabatic due to internal heating and depart by about 300–500 K from the adiabat in the lowermost mantle. b) Laterally averaged profiles of density derived from model M2 using the mineralogical models PSBD [Piazzoni *et al.* 2007] and SLB [Stixrude and Lithgow-Bertelloni 2005, 2007] for conversion of temperature to density. Density of the seismic reference models AK135M and PREM are shown for comparison. c) and d) same as b) for averaged 1-D profiles of shear and compressional wave velocities obtained from model M2, respectively.

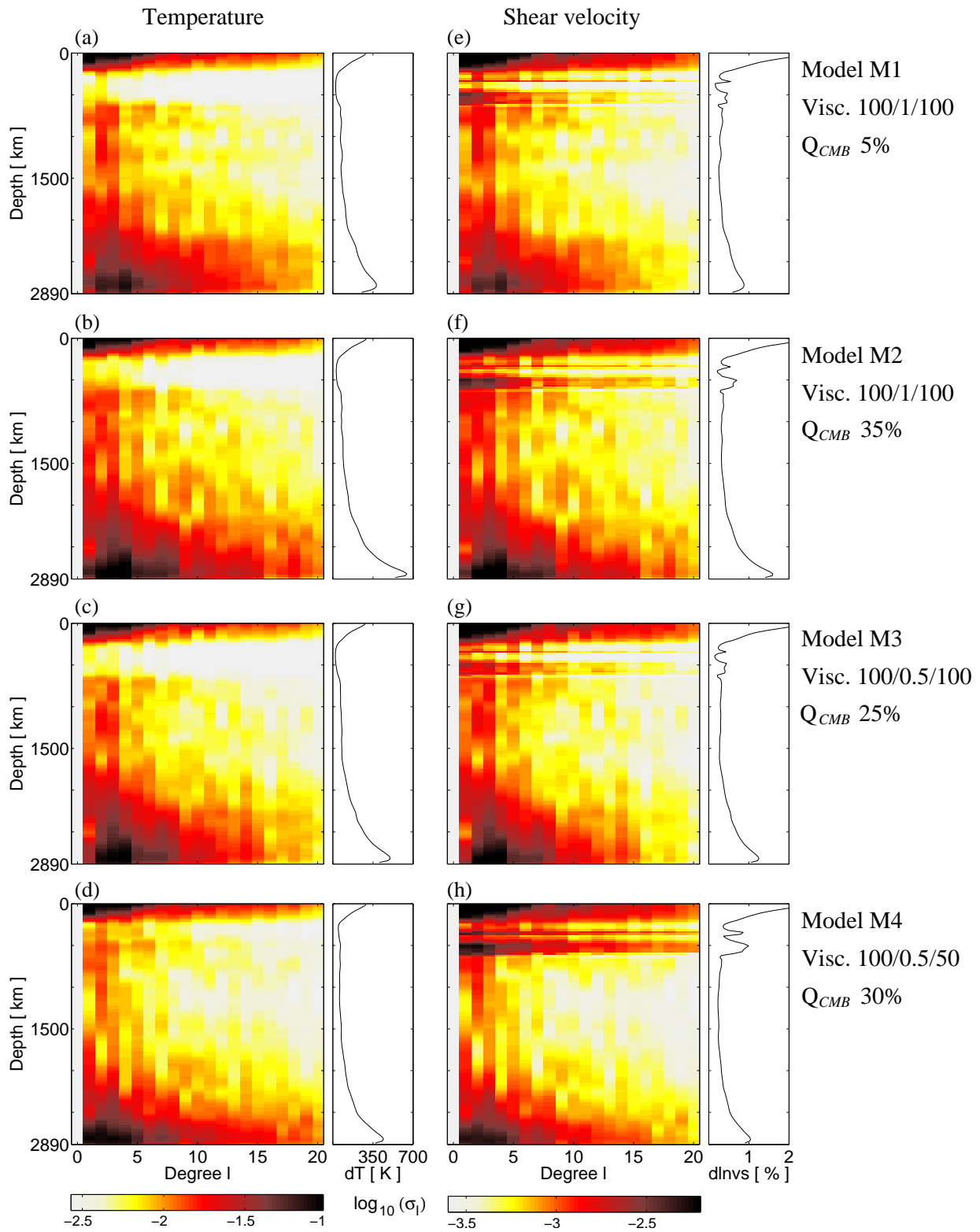


Figure 1.5: Spectral power of heterogeneity in (a–d) temperature and (e–h) shear wave velocity for mantle circulation models M1–M4 (see text). Spectral power is plotted on a logarithmic scale as a function of spherical harmonics degree and depth. Subplots on the right of each spectral heterogeneity map show the root-mean-square amplitudes of temperature and  $v_s$  perturbations as a function of depth, respectively. Relative variations of shear wave velocity are derived from the mantle circulation models using the mineralogical model SLB [*Stixrude and Lithgow-Bertelloni 2005, 2007*]. Note the differences between thermal and seismic heterogeneity. For example, the change in spectral power from the upper to the lower mantle is of opposite sense. The narrow bands of strong power in  $v_s$  in the upper mantle are a consequence of the mineralogy in the transition zone (see text), even though there is reduced thermal heterogeneity in these depth levels. Note the overall increase in spectral amplitude of temperature and  $v_s$  in the lowermost mantle.

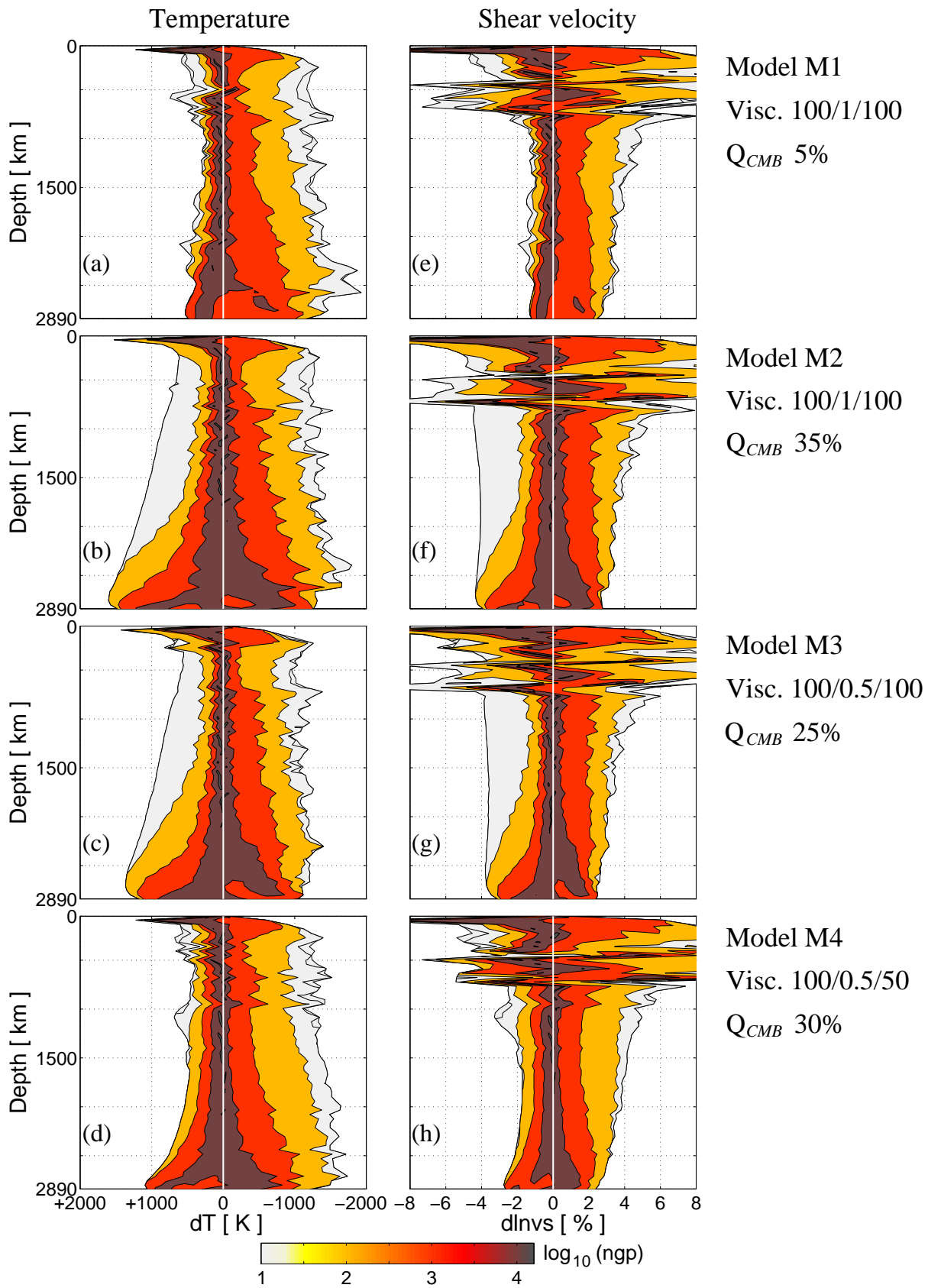


Figure 1.6: (a–d) Histograms of temperature variations in mantle circulation models M1–M4. Color scale and contours represent number of grid points ( $ngp$ ) on a logarithmic scale as a function of temperature perturbation and depth. Contour lines are plotted for  $\log_{10}(ngp) = 1, 2, 3$  and 4. Note: The x axis ( $dT$ ) of the temperature histograms has been flipped in consequence of the negative sensitivity of  $v_s$  to temperature to ease the comparison with the histograms for  $v_s$ . (e–h) Same as (a–d) for variations of shear wave velocity obtained from mantle circulation models M1–M4 using the mineralogical model SLB [*Stixrude and Lithgow-Bertelloni 2005, 2007*]. Comparison of thermal and elastic structures reveals the general decrease in sensitivity of  $v_s$  to temperature with depth. Maximum thermal variations on the order of  $-1000$  K from cold slabs and more than  $+1000$  K from hot upwellings in the lowermost mantle (M2–M4) result in maximum  $v_s$  anomalies of  $+2\%$  and  $-4\%$ . In contrast to these models with strong core heating, model M1 has much lower negative  $v_s$  amplitudes of around  $-1\%$  resulting from positive thermal anomalies of only up to  $+500$  K.

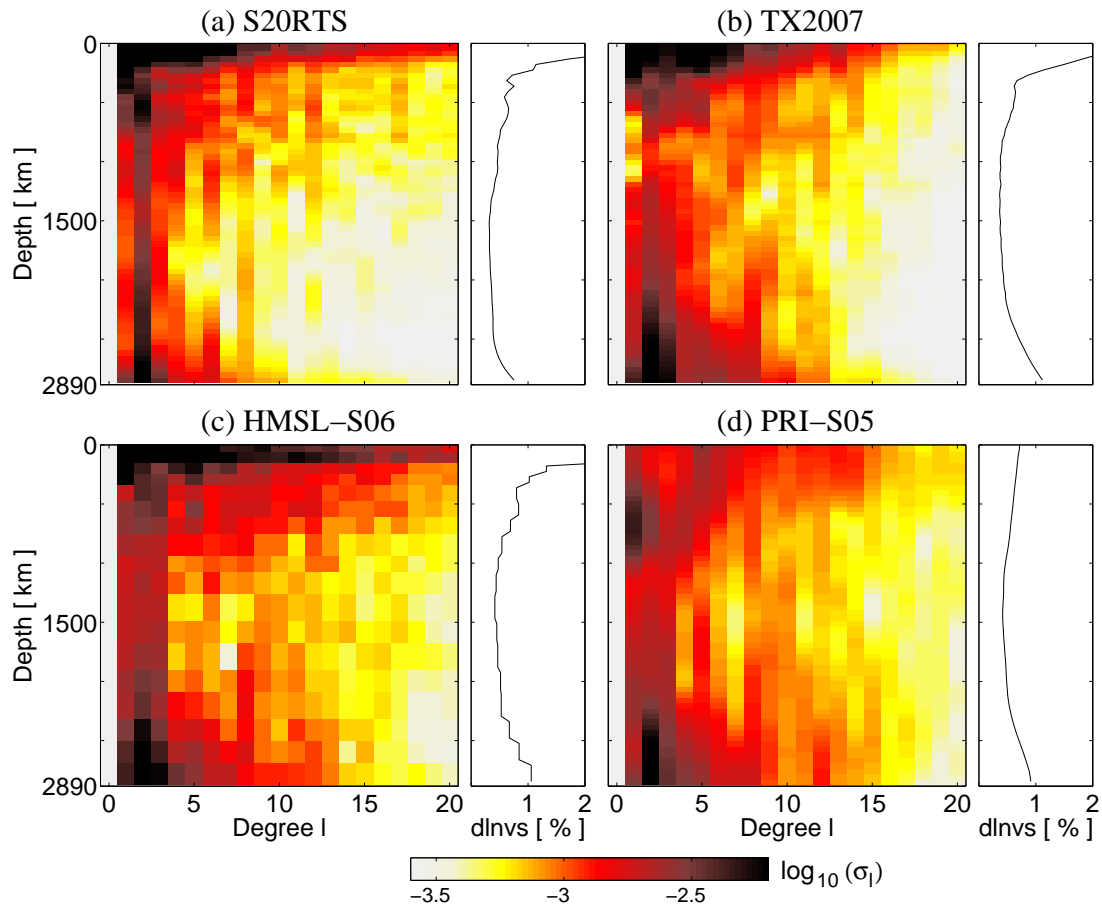


Figure 1.7: Spectral power of heterogeneity in tomographic S wave models S20RTS [Ritsema *et al.* 2004], TX2007 [Simmons *et al.* 2007], HMSL-S06 [Houser *et al.* 2008] and PRI-S05 [Montelli *et al.* 2006] plotted on a logarithmic scale as a function of spherical harmonics degree and depth. Subplots on the right of each spectral heterogeneity map show the root-mean-square amplitudes of relative  $v_s$  perturbations in each depth.



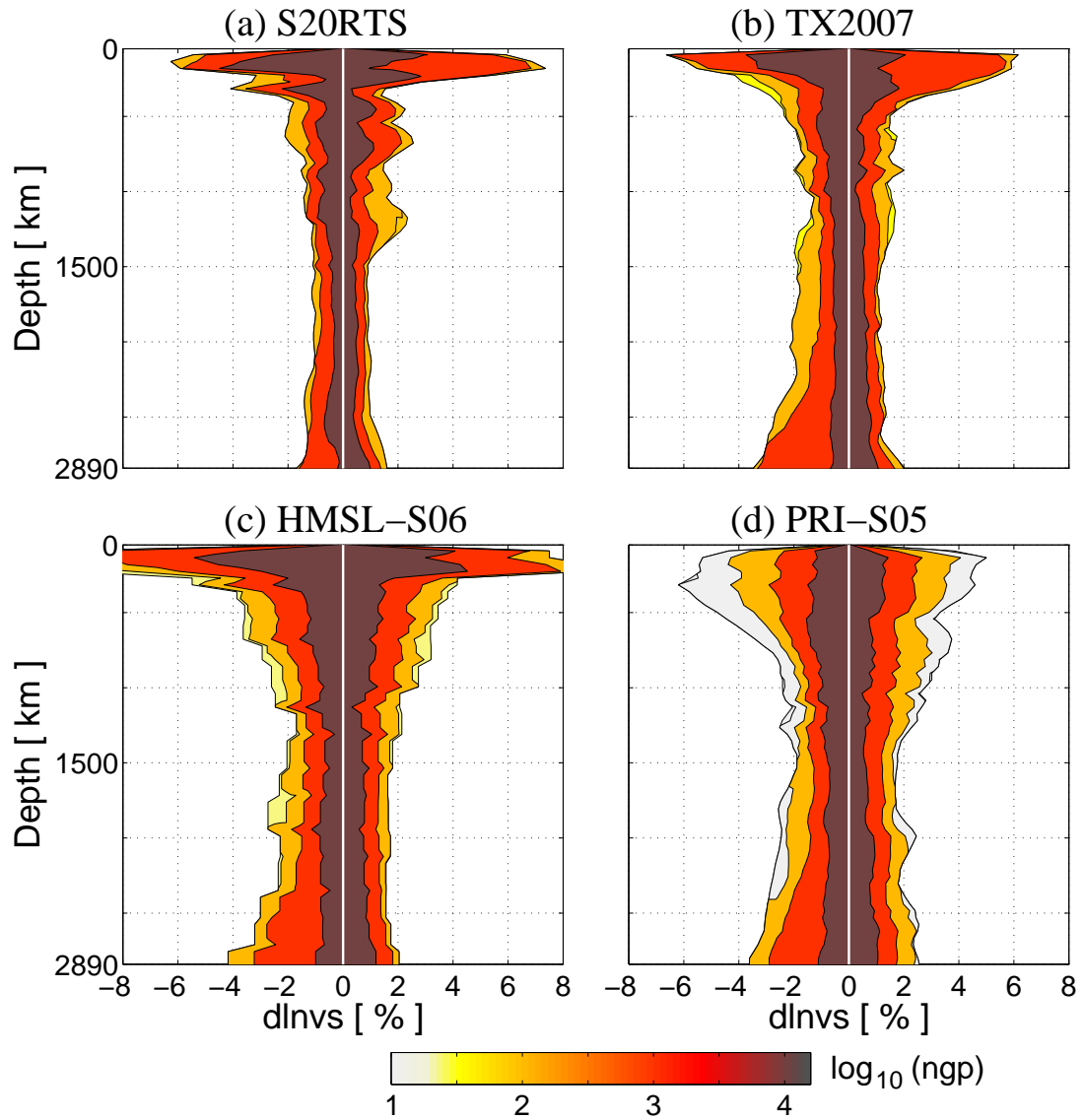


Figure 1.8: Histograms of relative variations in shear wave velocity for tomographic models S20RTS [Ritsema *et al.* 2004], TX2007 [Simmons *et al.* 2007], HMSL-S06 [Houser *et al.* 2008] and PRI-S05 [Montelli *et al.* 2006]. Color scale and contour lines are the same as in Figure 1.6. The tomographic histograms are normalized to the number of grid points in our MCMs to allow for a direct comparison with Figure 1.6.

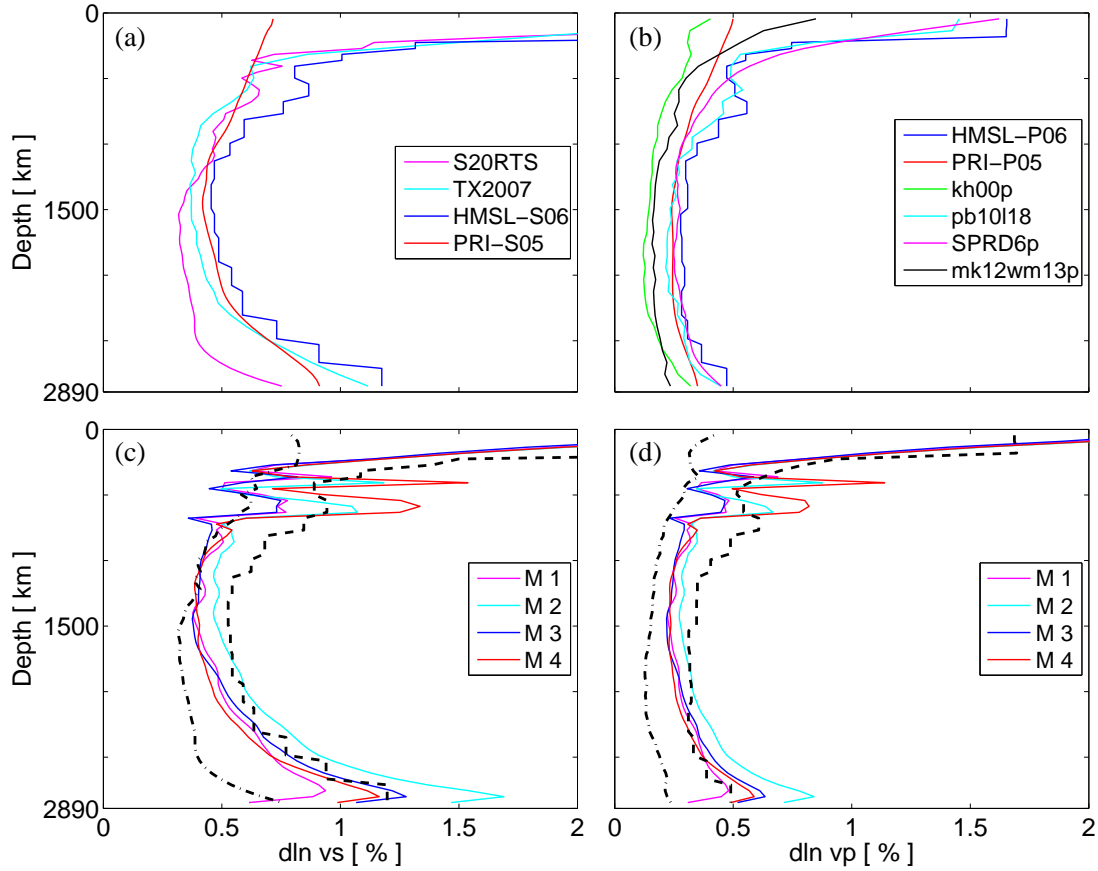


Figure 1.9: Comparison of root-mean-square amplitudes of heterogeneity between tomographic and geodynamic models. a) RMS profiles of variations in S-wave velocity of tomographic models S20RTS [Ritsema *et al.* 2004], TX2007 [Simmons *et al.* 2007], HMSL-S06 [Houser *et al.* 2008] and PRI-S05 [Montelli *et al.* 2006]. b) RMS profiles of P-wave velocity of models HMSL-P06 [Houser *et al.* 2008], PRI-P05 [Montelli *et al.* 2006], kh00p [Káráson and van der Hilst 2001], pb10l18 [Masters *et al.* 2000], SPRD6p [Ishii and Tromp 2001] and mk12wm13p [Su and Dziewonski 1997]. a) and b) illustrate the variation among different tomographic models but also show a general increase in heterogeneity with depth in the lower mantle. c) RMS profiles of S-wave heterogeneity predicted from models M1–M4 using the mineralogical model SLB [Stixrude and Lithgow-Bertelloni 2005, 2007]. Dashed and dash-dotted black lines show upper and lower bounds of tomographic heterogeneity strength taken from a). d) same as c) but for P-wave heterogeneity with dashed and dash-dotted black lines corresponding to upper and lower bounds of the P-wave models in b). Note that the amplitudes of heterogeneity derived from the geodynamic models falls within the bounds of tomographic models.

Table 1.1: Physical parameters and values employed in the simulations of mantle circulation. Values in this table were kept constant in all four mantle circulation models M1–M4.

outer shell radius	6370	km
inner shell radius	3480	km
$T_{Surface}$	300	K
$\eta_{ref}$ (reference viscosity)	$1.0 \times 10^{21}$	Pa s
thermal conductivity $k$	3.0	$\text{W m}^{-1} \text{K}^{-1}$
thermal expansivity $\alpha$ (surface)	$4.011 \times 10^{-5}$	$\text{K}^{-1}$
thermal expansivity $\alpha$ (CMB)	$1.256 \times 10^{-5}$	$\text{K}^{-1}$
internal heating rate $Q_{int}$	$6.0 \times 10^{-12}$	$\text{W kg}^{-1}$
heat capacity	$1.134 \times 10^3$	$\text{J kg}^{-1} \text{K}^{-1}$
$Ra_H$ (based on $\eta$ upper mantle)	$\simeq 10^9$	

Table 1.2: Variable parameters and respective values in models M1–M4. Viscosities in the lithosphere (LI), upper mantle (UM) and lower mantle (LM) are indexed to the reference viscosity of  $\eta_{ref} = 1 \times 10^{21}$  Pa s.

Model	Viscosity structure			Depth of UM/LM boundary [km]	$T_{CMB}$ [K]	CMB heat flow	
	LI/UM/LM	w.r.t $\eta_{ref}$				[TW]	(% surface heat flow)
M 1	100	1	100	660	2900	1.5	(5)
M 2	100	1	100	660	4200	12	(35)
M 3	100	0.5	100	660	4000	9	(25)
M 4	100	0.5	50	450	3500	10	(30)



# Chapter 2

## Tomographic Filtering of High-Resolution Mantle Circulation Models:

### Can Seismic Heterogeneity be Explained by Temperature Alone? \*\*

#### Abstract

Recent high-resolution mantle circulation models (MCMs) together with thermodynamic mineralogical models make it possible to construct 3-D elastic mantle heterogeneity based on geodynamic considerations. In the presence of a strong thermal gradient across D” and corresponding large temperature variations in the lower mantle, the heterogeneity predicted from isochemical whole mantle flow agrees well with tomographic models in terms of magnitudes of S-wave velocity ( $v_s$ ) variations [Schubert *et al.* 2009]. Here, we extend the comparison of geodynamic and tomographic structures by accounting explicitly for the limited resolving power of tomography. We focus on lateral variations in  $v_s$  and use the resolution operator  $\mathcal{R}$  associated with S20RTS [Ritsema *et al.* 2004] to modify our geodynamic models so that they reflect the long-wavelength ( $>1000$  km) nature and the effects of heterogeneous data coverage and damping inherent to the tomographic inversion. Prior to the multiplication with  $\mathcal{R}$ , the geodynamic models need to be reparameterized onto the basis of S20RTS. The magnitude reduction introduced by this reparameterization is significant and needs careful assessment. We attempt a correction of the reparameterization effects and find that the inherent tomographic filtering alone then leads to a magnitude reduction by a factor of  $\sim 2$  in the lower mantle. Our tomographically filtered models with strong core

---

\*\*Chapter 2 is accepted for publication in “Geochemistry, Geophysics, Geosystems”: Schubert, B. S. A., H.-P. Bunge and J. Ritsema (2009), *Tomographic Filtering of high-resolution mantle circulation models: Can seismic heterogeneity be explained by temperature alone?*, accepted in *Geochem. Geophys. Geosyst.*

heating agree well with S20RTS, which resolves maximum negative anomalies of around  $-1.5\%$  in the lowermost mantle. Temperature variations on the order of  $+1000$  K, corresponding to perturbations of around  $-3\%$  in  $v_s$  in the unfiltered model, would be seen as  $-1.5\%$  when “imaged” with the data and damping of S20RTS. This supports our earlier finding that isochemical whole mantle flow with strong core heating and a pyrolite composition can be reconciled with tomography. In particular, the large lateral temperature variations associated with lower mantle plumes are able to account for the slow seismic anomalies in the large low velocity zones under Africa and the Pacific. We also find that strong gradients in shear wave velocity of  $2.25\%$  per 50 km in our unfiltered models compare well with the sharp sides of the African superplume [e.g., *Ritsema et al. 1998*; *Ni et al. 2002*].

## 2.1 Introduction

Seismologists now widely agree that the large scale structure of the lower mantle is dominated by a ring of seismically fast material in the circum-Pacific region and by two prominent slow anomalies under Africa and the Pacific [e.g., *Dziewonski et al. 1977*; *Su et al. 1994*; *Li and Romanowicz 1996*; *Grand et al. 1997*; *van der Hilst et al. 1997*; *Su and Dziewonski 1997*; *Kennett et al. 1998*; *Masters et al. 2000*; *Ritsema et al. 2004*; *Montelli et al. 2006*; *Panning and Romanowicz 2006*; *Simmons et al. 2007*; *Houser et al. 2008*; *Kustowski et al. 2008*]. While the fast seismic structures can generally be related to the history of plate subduction [*Richards and Engebretson 1992*; *Bunge et al. 1998*; *Lithgow-Bertelloni and Richards 1998*; *Becker and O’Connell 2001*; *Conrad and Lithgow-Bertelloni 2002*; *McNamara et al. 2002*] the nature of the large low velocity zones remains elusive.

It has been proposed that these “superplumes” are chemically distinct from the surrounding material as they show anticorrelated variations in shear and bulk sound velocity as well as evidence for an increased density [*van der Hilst and Karason 1999*; *Ritsema and van Heijst 2002*; *Masters et al. 2000*; *Ishii and Tromp 2001*; *Wen et al. 2001*; *Ni et al. 2002*; *Trampert et al. 2004*; *Wang and Wen 2004*]. The large amplitudes of lateral variations in shear wave velocity of up to  $-3-4\%$ , in particular, have been taken to argue for compositional heterogeneity [e.g., *Farnetani and Samuel 2005*; *Samuel et al. 2005*].

Recently, we have shown that strong seismic heterogeneity in the lowermost mantle can be reconciled with isochemical whole mantle flow in the presence of a large thermal gradient across D” on the order of  $1000-1500$  K [*Schuberth et al. 2009*]. The strong thermal gradient in the lower boundary layer of our mantle circulation models leads to high excess temperatures of lower mantle upwellings with similar magnitude of  $+1000-1500$  K. These correspond to significant reductions in shear wave velocity of around  $-3-4\%$  after conversion to seismic heterogeneity with thermodynamically self-consistent models of mantle mineralogy [*Piazzoni*

*et al.* 2007; *Stixrude and Lithgow-Bertelloni* 2005, 2007]. The strong reductions in shear wave velocity in our models compare well with the negative  $v_s$  anomalies mapped by recent tomographic studies in the large low velocity zones under Africa and the Pacific [*Montelli et al.* 2006; *Simmons et al.* 2007; *Houser et al.* 2008]. We note that a high CMB temperature and a correspondingly large temperature drop across D” with associated high heat flow is consistent with a number of studies from geodynamics, seismology and mineral physics [e.g., *Glatzmaier and Roberts* 1995; *Kuang and Bloxham* 1997; *Boehler* 2000; *Steinle-Neumann et al.* 2001; *Buffett* 2002; *Gubbins et al.* 2004; *Nimmo et al.* 2004; *Nolet et al.* 2006; *Alfè et al.* 2002; *Alfè et al.* 2007; *van der Hilst et al.* 2007; *Steinberger and Holme* 2008].

In *Schuberth et al.* [2009], we did not account for the limited resolving power of tomography, which is known to be important in the analysis of geodynamic models. For example, *Mégnin et al.* [1997] applied the “linear tomographic filter”, corresponding to model SAW12D [*Li and Romanowicz* 1995] to mantle convection models. They showed that seismic data coverage significantly affects the spectral characteristics of their geodynamic models. *Bunge and Davies* [2001] traced rays through mantle circulation models, and found a significant change in the pattern of heterogeneity in regions of poor ray-coverage. Using the same approach, *Davies and Bunge* [2001] observed a systematic bias towards negative synthetic travel-time residuals and explained this by most earthquakes being located in areas of fast seismic velocities (i.e., active subduction). Recently, *Ritsema et al.* [2007] applied the resolution operator corresponding to the tomographic model S20RTS to isochemical and thermochemical models of mantle circulation and observed a substantial decrease the total spectral power of heterogeneity and a change in geographic pattern.

The aforementioned studies clearly demonstrate the need to account for the limited resolving power of tomography. However, being based on simple depth-independent linear conversions between temperature and seismic velocities, the studies were limited in their ability to investigate the effects of tomographic resolution on the magnitudes of velocity anomalies. As noted before, our models benefit from recent progress in mineral physics, which now provides improved relations between thermal and elastic parameters based on the thermodynamically self-consistent treatment of mineral phase assemblages. By combining these advances with an analysis of the effects of limited tomographic resolution, a quantitative comparison of geodynamically predicted seismic heterogeneity with tomography can be attempted. In the present study, we therefore extend the assessment of our MCMs by “filtering” their shear wave velocity structures with the resolution operator of S20RTS.

We start this paper with a short description of the tomographic filtering process. This involves the transformation of our geodynamic models onto the parameterization of S20RTS, which has important implications for the following analysis of seismic heterogeneity. In the comparison of our tomographically fil-

tered models with S20RTS we focus on statistical measures such as the spectral power, histograms and root-mean-square (RMS) profiles of heterogeneity.

The characteristics of our filtered models agree well with S20RTS. As expected, the magnitudes of seismic heterogeneity are significantly reduced during the filtering process. The amplitude reduction is due, in part, to the reparameterization and we explore possibilities to correct for this effect in a second step. Importantly, our MCM with strong core heating shows negative  $v_s$  anomalies of around  $-1.5\text{--}2\%$  in the lowermost mantle when only the effects of uneven data coverage and damping are considered. These values are fully compatible with the anomalies mapped S20RTS. Finally, we note that the gradients of seismic heterogeneity in the original (unfiltered) version of this model compare well with those inferred from direct observations of traveltimes sampling the lower mantle under Africa [Ritsema *et al.* 1998; Ni *et al.* 2002].

## 2.2 Tomographic Filtering and Parameterization of Models

### 2.2.1 Tomographic Filtering

We modify our theoretically predicted mantle heterogeneity using the resolution operator  $\mathcal{R} = \mathbf{G}^\dagger \mathbf{G}$  associated with S20RTS, where  $\mathbf{G}$  is the operator of the seismic forward problem and  $\mathbf{G}^\dagger$  its generalized inverse. Details of this procedure can be found in Ritsema *et al.* [2007]. The geodynamic prediction of seismic heterogeneity is defined as the “true” model  $\mathbf{m}$ , which is multiplied with  $\mathcal{R}$  to obtain a “filtered” representation  $\mathbf{m}'$  as if imaged by tomographic inversion:

$$\mathbf{m}' = \mathcal{R} \cdot \mathbf{m} \quad (2.1)$$

Since  $\mathcal{R}$  includes all the effects on resolution due to limited data coverage and model regularization, this process is computationally easier and faster than ray tracing and inversion of synthetic traveltimes. The filtered geodynamic model can then be compared to the corresponding tomographic model. In this respect, it is important that the resolution operator  $\mathcal{R}$  is computed based on the same damping parameter  $\epsilon$  as the tomographic model. In the case of S20RTS,  $\epsilon$  was chosen to be 0.035 [Ritsema *et al.* 2007], which we therefore adopt here as well.

Theoretical predictions of mantle heterogeneity are usually taken from numerical simulations, which are performed on large grids to accommodate the vigorous convective regime of the Earth. Typical grid spacings are on the order of several tens of kilometers globally. This results in meshes with  $\sim 10^6$  degrees of freedom [Bunge *et al.* 2002; McNamara and Zhong 2004a]. In contrast, global tomographic models currently provide a maximum spatial resolution on the order



of several hundred to thousand kilometers [Ritsema *et al.* 2004; Montelli *et al.* 2006; Simmons *et al.* 2007; Houser *et al.* 2008]. Geodynamic mantle structures thus have to be reparameterized onto the basis of the specific tomographic model to compare with, as resolution matrices are given in the corresponding parameterizations. Then, the adapted models parameters defining the true structure  $\mathbf{m}$  in Equation (2.1) can be tomographically filtered by multiplication with  $\mathcal{R}$ . The reparameterization leads to a drastic reduction in the model dimensionality, which in turn result in a significant alteration of the model characteristics, as will be shown in section 2.3. We introduce the following notation for our MCMs:  $M^o$  denotes their original parameterization,  $M^r$  the reparameterization to the basis of S20RTS, and  $M^f$  denotes the reparameterized and filtered model (i.e.,  $M^r$  multiplied with  $\mathcal{R}$ ). Changes in characteristics between the original model  $M^o$  and  $M^f$  are thus a combination of two separate effects. In the following, we use the terms “tomographic filtering” or “resolving power of tomography” only for the modification of models due to the multiplication with the resolution matrix.

### 2.2.2 Mantle Circulation Models

The construction and characteristics of  $v_s$  heterogeneity from our MCMs are described in detail in Schubert *et al.* [2009]. Here we summarize their numerical parameterization, which is important in the context of tomographic filtering.

The MCMs are computed with the code TERRA [Bunge and Richards 1996; Bunge *et al.* 1996, 1997] and are discretized with a mesh derived from the regular icosahedron, which provides almost equidistant grid spacing throughout the mantle. Horizontal grid spacing is around 30 km at the Earth’s surface and due to the sphericity of the model about 15 km at the CMB. In radial direction, the model is discretized with 128 equidistant layers leading to  $\sim 25$  km vertical grid spacing. This fine discretization leads to a total of around 80 million grid points, which allows us to simulate large scale mantle flow with earth-like convective vigor and to employ a thermal Rayleigh number of  $\sim 10^9$  based on internal heating. Thus, we are able to resolve a characteristic thermal boundary layer thickness on the order of 100 km, comparable to that of oceanic lithosphere.

Apart from the isochemical, pyrolitic nature of the investigated models, two basic assumptions are made in the prediction of global mantle heterogeneity: 1) a large-scale flow structure related to past plate motion, 2) a radial viscosity profile that agrees with post-glacial rebound and geoid observations.

We focus our analysis of tomographic filtering effects on two of the four models described in Schubert *et al.* [2009], namely M1 and M2. The models have the same viscosity stratification, but are end-member models in terms of bottom heating. The reference viscosity of the upper mantle is  $1 \times 10^{21}$  Pa·s, while the viscosity in both the lithosphere and the lower mantle is 100 times larger. Model M1 is heated mainly from within (5% core heating), whereas model M2 has a strong component of bottom heating of around 35% of the surface heat flux.

### 2.2.3 Tomographic Model S20RTS

S20RTS is based on three different data types: normal mode splitting functions, Rayleigh wave phase velocities and body wave travel times [Ritsema *et al.* 2004]. It is parameterized laterally in spherical harmonics up to degree 20 and radially with 21 spline functions. The radial splines interpolate continuously across the 660 km discontinuity and their spacing is denser in the upper mantle where the resolving power of the data is higher. In total, S20RTS includes 10,000 parameters resulting in a lateral resolution of around 1000 km. After damping, about 3000 effective unknowns are resolved.

## 2.3 Results

### 2.3.1 Effects of Parameterization and Tomographic Filtering

Figure 2.1 shows the shear wave velocity structure of model M2 in the two parameterizations, and filtered to the resolution of S20RTS. In Figure 2.1a, M2 is plotted in its original parameterization on the numerical grid of the code TERRA (i.e.,  $M2^o$ ). The earth-like convective vigor leads to a narrow upper thermal boundary layer, around 100 km thick. Thin and elongated fast velocity structures at 340 km depth (e.g., all around the Pacific) correspond to cold, downwelling slabs located in regions of present day subduction. With increasing depth, their locations change according to earlier stages of subduction as given by the plate motion history. In the lowermost mantle, the downwelling material spreads laterally above the CMB and the strong lower thermal boundary layer leads to significant hot upwellings, as for example in the southeast Pacific.

In Figure 2.1b, M2 is plotted in the parameterization of S20RTS (i.e.,  $M2^r$ ). Spatial resolution is significantly lower than in  $M2^o$  due to the restriction of model parameters to spherical harmonics degrees lower than 20. The reparameterization results in the spreading of anomalies and in a reduction of their amplitudes. Especially the thin slabs in the upper mantle are substantially broadened compared to the original parameterization. At 100 km depth, fast continental areas as well as slow mid-ocean ridge systems display lower values than in the original parameterization. The same is true in the lower mantle, where the magnitudes of the large slow anomalies located under the Pacific, Africa and the Indian Ocean are reduced.

Figure 2.1c shows  $M2^f$ ; that is,  $M2^r$  filtered to the resolving power of S20RTS. The main effect of the filtering is to further reduce the amplitudes in the lower mantle, especially at 2800 km depth. There, the shape of the anomalies is not affected much in contrast to the mid-mantle. At 1450 km and 2100 km, some lateral smearing of heterogeneity can be observed. Interesting to note is that in

certain regions of the upper mantle amplitudes appear to be enhanced. This is, for example, the case for the slow seismic velocities under the Pacific and the fast velocities corresponding to the Farallon slab under western North America at 340 km depth.

Irrespective of the general magnitude reduction, Figures 2.1b and 2.1c indicate that the pattern of seismic heterogeneity in the lowermost mantle is resolved quite well by S20RTS. This is probably related to the fact that S20RTS incorporates a large set of diffracted data in the S-wave dataset in addition to surface wave dispersion measurements and normal mode splitting coefficients [Ritsema *et al.* 2004] resulting in a rather uniform global data coverage.

For comparison, S20RTS is shown in Figure 2.1d. The general character of our filtered model M2<sup>f</sup> agrees quite well with S20RTS. The poor geographic correlation, however, is primarily due to the unknown initial condition of the forward problem of mantle dynamics [Bunge *et al.* 2003], and uncertainties in the plate motion history [Bunge *et al.* 2002; McNamara and Zhong 2005; Schubert *et al.* 2009]. Thus, independently of the important effects of tomographic resolution, this limits the use of morphological considerations in the assessment of geodynamic models, unless better constraints, especially on the temperature variations in the past, become available.

### 2.3.2 Effects on Spectral Characteristics of Heterogeneity

In Figure 2.2, we plot spectral heterogeneity maps (SHM) [Jordan *et al.* 1993], which are contour plots of spectral amplitude of heterogeneity versus depth. Shown are M1 and M2 in their original, reparameterized, and filtered representations (Figs. 2.2a–c and 2.2d–f, respectively). In addition, we show corresponding radial profiles of the root-mean-square power of the spherical harmonics expansion. Spectral power  $\sigma_l$  per degree  $l$  is computed at each depth level and for spherical harmonics degrees  $l = 1, \dots, 20$  by [Dahlen and Tromp 1998, B.8]

$$\sigma_l = \sqrt{\frac{1}{2l+1} \left[ a_{l0}^2 + \sum_{m=1}^l (a_{lm}^2 + b_{lm}^2) \right]}, \quad (2.2)$$

where  $a_{lm}$  and  $b_{lm}$  are the coefficients of the expansion and the RMS power  $\delta\hat{v}$  up to degree  $l_{max}$  is given by:

$$\delta\hat{v}_{l_{max}} = \sqrt{\frac{1}{\sqrt{4\pi}} \sum_{l=1}^{l_{max}} (2l+1)\sigma_l^2}. \quad (2.3)$$

The spectral characteristics of both MCMs are quite similar, Model M1 only shows overall less power. The strong degree two in the lower mantle is mainly a

consequence of the long-wavelength structure of earlier stages of the plate motion history. Together with the viscosity stratification this generally leads to a red spectrum of the mantle [*Bunge and Richards 1996; Bunge et al. 1998, 2002*].

In the original parameterization of M1 and M2, heterogeneity is strongest in the thermal boundary layers, where it is distributed over a wide range of spatial scales. In the mid-mantle, heterogeneity is weaker and concentrated in low degrees. Thin layers of increased heterogeneity in the upper mantle correspond to phase transformations at 410, 520 and 660 km depth.

Figures 2.2b and 2.2e show the SHMs of the reparameterized models M1<sup>r</sup> and M2<sup>r</sup>. Differences to the original models are small and derive from the difference in radial parameterization. The strong heterogeneity in the transition zone is smeared vertically and the distinct band of the 410 km discontinuity is smoothed away. Heterogeneity in the lowermost mantle is affected as well, which can also be seen from the RMS profiles.

The SHMs of the filtered models M1<sup>f</sup> and M2<sup>f</sup> are given in Figures 2.2c and 2.2f, respectively. Power is mainly reduced in high degrees, and the lowermost mantle is affected stronger than the rest. This is also visible from the RMS profiles. The band of high spectral power in the transition zone, which is more pronounced in M2<sup>r</sup>, is mostly filtered away and only low degrees (1–5) still show substantial power there.

### 2.3.3 Effects on Magnitudes of Heterogeneity

Figure 2.3 shows histograms of the lateral  $v_s$  variations in our MCMs; that is, we contour the distribution of magnitudes of heterogeneity as a function of relative perturbation and depth. In analogy to the SHMs in Figure 2.2, the histograms are given for the original, reparameterized, and filtered versions of M1 and M2. First, we note that in the original parameterization (Figs. 2.3a and 2.3d), largest amplitudes are located in the upper mantle and the transition zone with values of up to 5% and more. In the upper part of the lower mantle, heterogeneity is weaker and the distribution is asymmetric towards fast seismic anomalies (i.e., positive skewness). In M2, the skewness changes with depth being negative in the lowermost mantle as a consequence of the strong thermal gradient across D<sup>''</sup>. The most prominent feature in the original parameterization of M2 is the asymmetry of maxima in the lowermost mantle with values of  $-4\%$  and  $+2.8\%$ . In contrast, M1 with weak core heating only shows small negative anomalies of less than  $-1\%$  in most of the lower mantle and a positive skewness throughout.

Figures 2.3b and 2.3e show the histograms of the reparameterized models M1<sup>r</sup> and M2<sup>r</sup> and a comparison with Figures 2.3a and 2.3d illustrates that the reduction of magnitudes introduce in this step is depth-dependent. Amplitudes of heterogeneity are decreased stronger in the upper half than in the lower half of the mantle. This indicates that the short-scale variations in the upper mantle are not captured by the degree-20 parameterization. Amplitude reduction in the

lower mantle is smaller due the predominance of long-wavelength structure there, which in turn is a consequence of the higher viscosity and the absence of major phase changes. Effects on positive and negative anomalies are different as can be seen, for example, from the change in skewness in the lower mantle. The same holds for the transition zone, where positive anomalies are affected stronger than negative perturbations, as is apparent from the fact that the positive anomalies at 660 km depth have all but disappeared.

As expected, the tomographic filtering further reduces the amplitudes of heterogeneity (see Figs. 2.3c and 2.3f). Both models show similar magnitudes of positive anomalies in the lower mantle. Similar to the original parameterization, model M1<sup>f</sup> displays asymmetric distributions towards positive values in all of the lower mantle, only that maximum negative  $v_s$  anomalies are around  $-0.5\%$  now. The histogram of M2<sup>f</sup> is more symmetric and maximum anomalies in the lowermost mantle are around  $\pm 1.5\%$  reaching up to  $\pm 2\%$  close to the CMB.

### 2.3.4 Quantitative Analysis of Magnitude Effects

To quantitatively analyze the effects of reparameterization and tomographic filtering, we first concentrate on root-mean-square amplitudes of heterogeneity. Figure 2.4a shows RMS profiles for  $v_s$  variations in the three versions of M2 (i.e., the original, reparameterized, and filtered model). RMS values in the original parameterization are largest in the upper thermal boundary layer with values exceeding 2%. Between 300 and 1500 km depth, heterogeneity decreases to values of 0.5% and monotonically increases again from this mid-mantle minimum to values of up to 1.6% near the CMB. Strong variations of RMS in the upper mantle correspond to the phase transformations in the transition zone.

RMS amplitudes of the reparameterized model are lower than in the original parameterization. In addition, only one maximum is left in the transition zone as noted also for the SHMs in section 2.3.2. Between 800 km and 2000 km depth, RMS values are below 0.5% and reach  $\sim 1.2\%$  close to the CMB. The amplitude difference to the original parameterization is strongest in the transition zone and uppermost lower mantle and decreases with depth. As mentioned above, the depth-dependence of this magnitude reduction relates to the different nature of heterogeneity between upper and lower mantle (i.e., short-scale variations in the upper mantle due to a complex set of phase changes and predominantly long-wavelength features in the lower mantle resulting from the higher viscosity there).

After applying the tomographic filter, the RMS profile is nearly constant in most of the mantle with values close to 0.3%, but still shows a weak minimum at around 1500 km depth. A comparison with the profile of the reparameterized model shows that the reduction of RMS values is stronger in the lower half of the mantle indicating again that the resolving power of S20RTS is better in the upper mantle. There, mainly the local maximum in the transition zone is reduced. In

the lowermost 300 km, the filtered model shows a strong increase in RMS values reaching  $\sim 0.7\%$  close to the CMB.

Figure 2.4b shows the total relative amplitude reduction resulting from the filtering procedure. In addition, we plot the separated contributions from the effects of reparameterization and tomographic filtering. The total relative amplitude reduction is almost constant with depth in the lower mantle and exceeds 0.5 nearly everywhere. Close to the CMB, about two-thirds of the original amplitude is lost. Note that the profiles for the reparameterization and tomographic filtering effects cross at around 1500 km depth. Above this depth, the total reduction is dominated by the reparameterization while the effects of tomographic resolution are stronger below.

### 2.3.5 Correcting for the Effects of Reparameterization

As seen from Figures 2.2–2.4, the characteristics of the tomographically filtered models are significantly influenced by the effects of the reparameterization. A first order correction of these effects could be attempted in a post-processing step to the tomographic filtering due to the linear nature of  $\mathcal{R}$ ; that is, the heterogeneity of short-scale structure, which is lost in the degree-20 parameterization of the filtering procedure, can be considered as additional contribution in the quantitative analysis. In the following, we try to do this by correcting for the total amplitude reduction resulting from the reparameterization. This allows estimates of the properties of our models as if only exposed to the limited resolving power of S20RTS.

The RMS values  $\delta\hat{v}^{f+}$  for the tomographic filter effect alone are obtained by computing the ratio of RMS values of the tomographically filtered model  $M^f$  with the reparameterized model  $M^r$  for each depth  $d$ . In this way, we isolate the component of amplitude reduction associated with  $\mathcal{R}$ . We then multiply this depth-dependent ratio  $\frac{\delta\hat{v}^f}{\delta\hat{v}^r}$  with the RMS values of the original model  $\delta\hat{v}^o$ :

$$\delta\hat{v}^{f+}(d) = \delta\hat{v}^o(d) \cdot \frac{\delta\hat{v}^f(d)}{\delta\hat{v}^r(d)}. \quad (2.4)$$

In Figure 2.5, we show RMS profiles for our filtered models corrected in this manner, which we also denote  $M1^{f+}$  and  $M2^{f+}$ . The RMS profile of S20RTS is plotted for comparison. The general characteristics of the original models, such as the large amplitudes close to the thermal boundary layers and peaks in the transition zone, are conserved when only accounting for the tomographic filtering; that is, without the bias due to the reparameterization. As in the original parameterization, model  $M2^{f+}$  with high CMB heat flux has larger values than  $M1^{f+}$  in all depths. Below 1500 km depth, the difference between  $M1^{f+}$  and  $M2^{f+}$  increases gradually. RMS values in  $M2^{f+}$  get larger below 2500 km, where model  $M1^{f+}$  only shows a moderate increase. Directly above the CMB models

$M1^{f+}$  and  $M2^{f+}$  display RMS amplitudes of 0.4% and 0.8%, respectively. Below 1500 km depth,  $M2^{f+}$  agrees remarkably well with S20RTS, while  $M1^{f+}$  shows values that are 20–30% lower than S20RTS there.

### 2.3.6 Correction of Spectral Characteristics

In a next step, we perform a similar correction as in section 2.3.5 for the spectral heterogeneity maps. In this case, we account for the loss of spectral power during the reparameterization for each spherical harmonics degree  $l$ , separately, again depending on depth:

$$\sigma_l^{f+}(d) = \sigma_l^o(d) \cdot \frac{\sigma_l^f(d)}{\sigma_l^r(d)} \quad (2.5)$$

Figures 2.6a,b show the SHMs for the filtered and corrected models  $M1^{f+}$  and  $M2^{f+}$ , respectively. The comparison with Figures 2.2a and 2.2d illustrates the effect of the limited tomographic resolution of S20RTS alone. Heterogeneity is mostly reduced in the high degrees of the lower mantle. Furthermore, the tomographic filtering results in vertical smearing of power from the transition zone into the upper part of the lower mantle.

Except for their magnitudes, the spectral characteristics of  $M1^{f+}$  and  $M2^{f+}$  are very similar, in analogy to the original SHMs in Figures 2.2a and 2.2d. Both show a marked change in spectral pattern across the 660 km, discontinuity, which is even more pronounced than in the unfiltered original models due to the strong reduction of power in high degrees of the lower mantle. The characteristic difference between upper and lower mantle compares well with the change in spectral pattern seen in S20RTS (Fig. 2.6c), and is a consequence of the phase changes in the transition zone together with the unresolved structure in the higher degrees of the lower mantle.

### 2.3.7 Correction of Histograms

We also attempt a first order correction of the amplitude distributions in our MCMs. For this, we take the values of seismic heterogeneity from the filtered model and multiply them with the depth-dependent ratio of RMS values from the original model and the reparameterized model (which is similar to the operation in Equation (2.4)). To account for possible asymmetries in the reparameterization, we perform this operation for positive and negative perturbations separately.

In Figure 2.7, we show histograms for the filtered and corrected models  $M1^{f+}$  and  $M2^{f+}$  together with the histogram of S20RTS. The main characteristics of the original models are conserved (e.g., largest amplitudes in the upper mantle, and in  $M2^o$  a change in skewness from positive to negative throughout the lower mantle,

which can also be seen in the histogram of S20RTS). Comparing the maximum values in Figures 2.7a,b with those in Figures 2.3a,d indicates that amplitudes of heterogeneity in our MCMs are lowered by almost a factor of 2 when affected by the limited tomographic resolution alone. The histogram of  $M2^{f^+}$  (Fig. 2.7b) compares well with S20RTS for both positive and negative amplitudes in most depth levels. This is markedly different for  $M1^{f^+}$ , which shows maximum negative anomalies of less than  $-0.5\%$  in most of the lower mantle as a consequence of the lower core heating.

## 2.4 Discussion

### 2.4.1 Lateral Temperature Variations and Magnitudes of Seismic Heterogeneity

An important result of our analysis is the change in the characteristics of our geodynamic models introduced by the reparameterization. The transformation of model parameters from the original high-resolution grid ( $\sim 25$  km global grid spacing) onto the low-degree spherical harmonics basis of S20RTS is needed to perform the tomographic filtering and results in a significant “loss” of short-scale heterogeneity. The fact that heterogeneity in the upper mantle suffers more drastically from the long-wavelength reparameterization is related to velocity variations being present on very short length-scales there (see SHMs in Figs. 2.2a and 2.2d), which in turn is a consequence of the complex set of phase transformations in the transition zone. Interestingly, the associated amplitude reduction of the seismic anomalies appears to be not only depth-dependent, but also different for positive and negative velocity variations, as can be seen from the change in skewness of the histograms in Figure 2.3. Most importantly, however, the amplitude reduction induced by the reparameterization is comparable in magnitude to the effects of uneven data coverage and damping.

The tomographic filtering is also depth-dependent, indicating a better ability of S20RTS to resolve velocity variations in the upper mantle due to fundamental mode and overtone surface wave constraints. Owing to their different depth dependencies of relative amplitude loss, the combination of reparameterization and subsequent multiplication with  $\mathcal{R}$  then leads to an almost constant total magnitude reduction in the lower mantle of around 60 percent of the original amplitudes (see Fig. 2.4).

The loss of short-scale heterogeneity associated with the reparameterization in itself seems unphysical, as structural variations on length-scales of around 100 km and less are expected to be present in the mantle (e.g., slabs). However, whether the reparameterization should be accounted for in comparisons of geodynamic and seismic models depends on the potential of short-scale structure to affect long-wavelength tomographic images. If that is the case, geodynamic models should



be modified in such a way only, as to reflect the effects of limited resolving power alone.

In this respect, *Mégnin et al.* [1997] have shown that aliasing of short-scale heterogeneity into the low degrees of tomographic models can be observed in the inversion of long period S-wave data for large-scale structure. In other words, velocity variations in the inverted long-wavelength structure may be larger than the actual large-scale structure in Earth due to short-scale structure “seen” by the seismic waves. This implies that the information on short-scale heterogeneity in the seismic data is not totally lost, as for example due to finite frequency effects such as wave front healing, but rather is mapped as additional contribution into the tomographic models. Put differently, the aliasing in tomography may counteract to some extent the reducing effect of limited tomographic resolution and result in a slight amplification of the long-wavelength anomalies.

The occurrence of structural aliasing is expected from theoretical considerations [*Dahlen* 2004]: In the case of perfect illumination of a given velocity perturbation by waves with finite frequency, the anomaly recovered with ray-tomography will have the same volume-integrated total perturbation. The recovered anomaly, however, will be broader due to lateral smearing and will have a smaller maximum amplitude. This “mass” conservation of seismic anomalies suggests that only uneven data coverage and the associated need to damp inversions are the reason for tomographically resolved amplitudes being on average (in a root-mean-square sense) smaller than in the Earth.

As for the geodynamic models, the volume-integral of the velocity perturbations is not conserved during reparameterization and we have therefore attempted to correct for the associated magnitude reduction. Taking advantage of the linearity of the resolution operator, it is possible to consider the short-scale structure lost in the long-wavelength parameterization as additional contribution in the statistical characteristics of the tomographically filtered MCMs (see sections 2.3.5–2.3.7). This way, an approximation of the magnitude reduction of seismic heterogeneity due to the limited tomographic resolving power alone is provided.

After correcting for reparameterization induced changes in the characteristics of our tomographically filtered geodynamic models, we find that shear wave velocity anomalies are reduced by a factor of around 2 in the bottom 500 km of the mantle (i.e., from the tomographic filtering alone). More specifically, large negative anomalies of  $-3-4\%$  in the lowermost mantle, corresponding to plume excess temperatures of  $+1000-1500$  K, would be mapped as  $-1.5-2\%$ , and are therefore in good agreement with the values of S20RTS. We note that large lateral temperature variations in the lower mantle can be anticipated from a number of geodynamic considerations on plume excess temperatures, including the adiabatic ascent of plumes in the subadiabatic mantle [*Bunge* 2005] and the fact that the adiabatic gradient is itself temperature dependent, getting steeper with increasing temperature [e.g., *Piazzoni et al.* 2007].

The corrected histogram of our strongly bottom heated model M2 shows slightly larger maximum positive velocity anomalies than S20RTS (compare Figs. 2.7b and 2.7c). This may on one hand indicate that the negative temperature variations of slabs in our models are somewhat too large. On the other hand, it may as well show that accounting for the total amplitude reduction of the reparameterization overestimates the aliasing effect in tomography. However, as the difference occurs only for slabs and the reparameterization (and therefore the way that tomographic aliasing is represented in our comparison) mostly affects the upper mantle, this does not influence our conclusions on plume temperatures in the lower mantle.

We do not preclude compositional variations in Earth’s mantle, but the tomographic filtering of our MCMs shows that it is quite possible to explain seismic heterogeneity by temperature variations alone. This finding may place limits on the potential role of chemical heterogeneity, as the large plume temperatures anticipated in the lower mantle already account for the seismic signal in the large low velocity zones. Chemical heterogeneity, adding on to the large thermal anomalies, is expected to further enhance the seismic anomalies [*Wang and Weidner 1996; Jackson 1998a*] and will therefore possibly overpredict the magnitudes of velocity variations. Thus, our study lends further support to the notion of vigorous, isochemical whole mantle flow with strong core heating.

## 2.4.2 Horizontal Gradients of Thermal and Seismic Heterogeneity

Sharp horizontal gradients in seismic velocities have sometimes been advanced as an argument for chemical variations [*Ni et al. 2002; Brodholt et al. 2007*]. Evidence for strong gradients in shear wave velocity, which may be related to anomalously warm buoyant mantle due to continental insulation [*Anderson 1982; Phillips and Bunge 2005*], comes from the observation of rapid variations of body wave traveltimes over a small azimuthal range for ray-paths turning in the deep mantle under Africa [e.g., *Ritsema et al. 1998*]. Based on this direct observation, *Ni et al. [2002]* estimated that shear wave velocities in the lower mantle vary by up to 3% over a distance of 50 km (i.e., a gradient of relative perturbations of  $\sim 6 \times 10^{-7} \text{ m}^{-1}$ ).

To investigate the abruptness with which velocity variations change laterally in isochemical whole mantle flow, we can directly examine our unfiltered models, as we do not need to account for tomographic resolution effects in the comparison to the direct observation of rapid azimuthal traveltime variations.

Our unfiltered MCM M2<sup>o</sup> (Fig. 2.1a) shows slow anomalies in the lowermost mantle directly bounded by fast material. The resulting gradients are around  $4.5 \times 10^{-7} \text{ m}^{-1}$  or 2.25% over 50 km, comparable to the values suggested by *Ni et al. [2002]*. These gradients in shear wave velocity relate to thermal gradients

of  $\sim 0.015\text{--}0.018\text{ K m}^{-1}$  or around 750–900 K per 50 km. Such strong thermal variations in isochemical mantle circulation models are entirely expected, as heat transport inside the Earth is dominated by advection (typical Peclet numbers of around 10–100) so that sharp gradients are preserved.

### 2.4.3 Current Limitations in the Comparison of Geodynamic and Tomographic Seismic Heterogeneity

In the present study, we concentrated on variations in shear wave velocity and the comparison to S20RTS. It would be helpful to also compare our MCMs to other tomographic S-wave models, as well as to compare the additionally predicted  $v_p$  heterogeneity to tomographic P-wave models. However, resolution matrices are currently available only for a few tomographic models. Especially for models with a large number of parameters in the inversion, the construction of  $\mathcal{R}$  is computationally not feasible [Nolet, 2008; pers. comm.]. A further complication arises from the varying degrees of approximations concerning the forward problem of seismology used in different tomographic studies. Furthermore, direct comparison of S- and P-wave models may be biased due to the different frequency content of the respective data sets. The approach taken here thus seems not well suited to address the question of potential anticorrelation of  $v_s$  with bulk sound velocity  $v_\phi$ , or density, in the lowermost mantle.

Our conclusions are furthermore limited in that the mineralogical models currently do not include the post-perovskite phase. Recent studies point to the possibility that the anticorrelation of lower mantle shear and bulk sound velocity variations may be caused by phase heterogeneity associated with post-perovskite [Hutko *et al.* 2008; Hernlund and Houser 2008]. However, post-perovskite is likely to occur only in cold regions of the lowermost mantle [Tateno *et al.* 2009] and therefore our results on high plume excess temperatures will probably not be affected much.

## 2.5 Conclusions

We have quantitatively related lateral temperature variations to magnitudes of seismic heterogeneity taking into account their complex relation through mantle mineralogy and the effects of limited tomographic resolution. In our analysis, we concentrated on isochemical whole mantle circulation to study the effects of bottom heating without any complications due to compositional variations. We have focused on models with strong core heating, as a number of studies have argued for a large thermal gradient across D'' on the order of 1000 K and a high core heat flow.

The tomographic filtering of seismic velocity structures involves the reparameterization of our geodynamic models onto the long-wavelength basis of S20RTS.

The drastic decrease in model dimensionality from  $8 \times 10^7$  to  $10^4$  results in an artificial reduction of the magnitude of seismic heterogeneity. Based on the linearity of the resolution operator, we have shown that the short-scale heterogeneity lost in the reparameterization can be considered as an additional contribution to the statistical characteristics of the filtered MCMs. With this correction, we arrive at a consistent comparison with tomography, as it is likely that seismic inversions inherently incorporate information on short-scale variations due to structural aliasing.

We find a good agreement of the tomographically filtered and reparameterization corrected MCMs with S20RTS. However, only the MCM with strong core heating shows magnitudes of slow seismic anomalies in the lowermost mantle that are compatible with the values seen in S20RTS. Shear wave velocity perturbations of  $-3-4\%$  in this model are reduced by a factor of 2 when accounting for uneven data coverage and damping. Furthermore, thermal gradients of around  $750-900$  K per 50 km in the corresponding unfiltered model result in shear wave velocity gradients of  $\sim 2.25\%$  over 50 km, which are in good agreement with the study of *Ni et al.* [2002] for the sharp sides of the African superplume. Our results thus confirm the conclusion of *Schuberth et al.* [2009] that isochemical whole mantle circulation with substantial CMB heat flow of 9–12 TW and a pyrolite composition is consistent with a number of seismic observations on the lower mantle.



## 2.6 Figures – Chapter 2

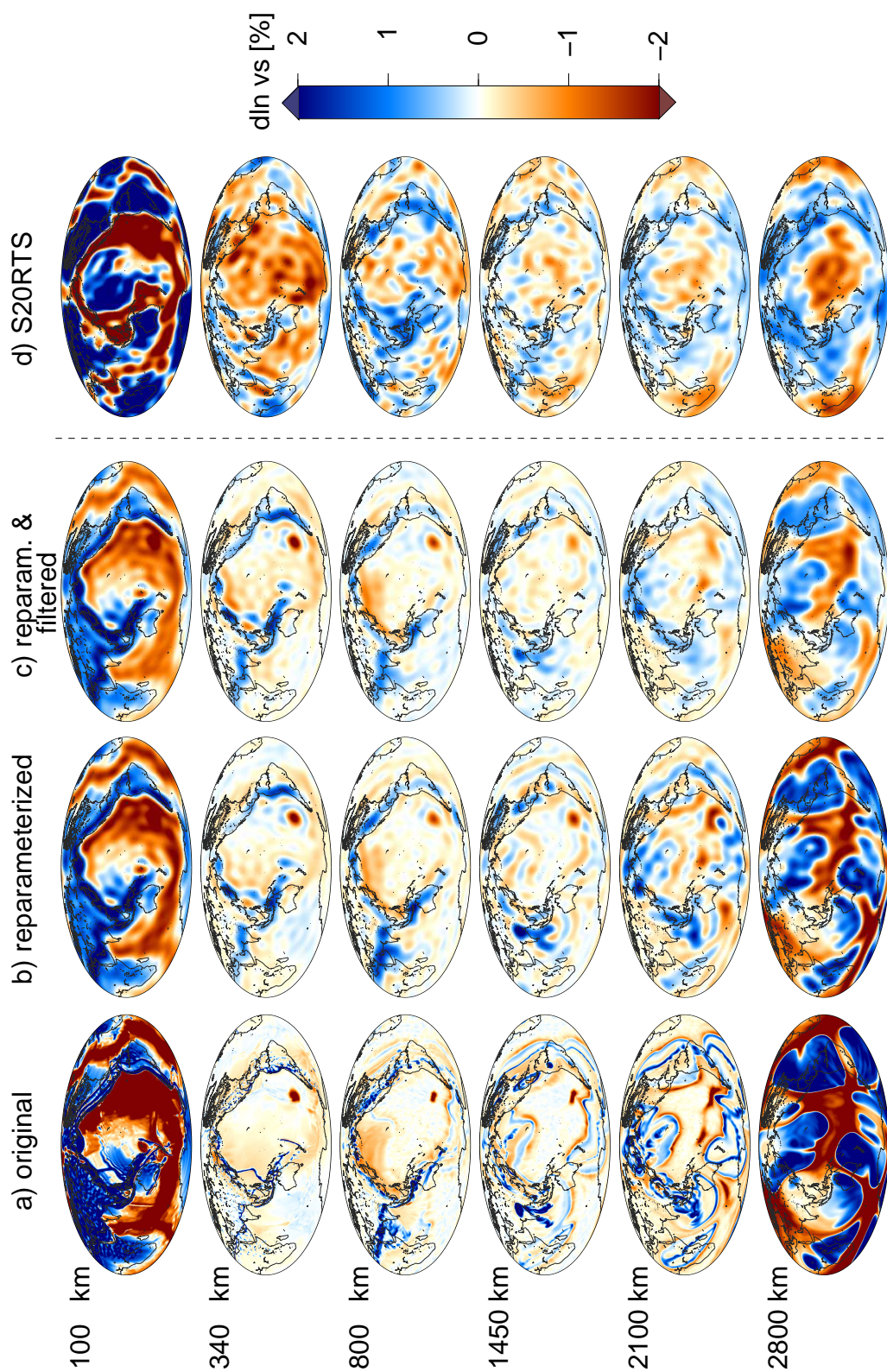


Figure 2.1: Depth slices through (a–c) mantle circulation model M2 (35% core heating) and (d) tomographic model S20RTS [Ritsema *et al.* 2004]. Variations in S-wave velocity are given relative to each corresponding 1D radial reference profile. a) M2 in the original parameterization of the code TERRA (80 million grid points resulting in  $\sim 25$  km global grid spacing) [Schuberth *et al.* 2009]. b) M2 in the parameterization of S20RTS (spherical harmonics up to degree 20 and 21 radial splines resulting in 10,000 model parameters and a spatial resolution on the order of 1000 km). Note the amplitude reduction of heterogeneity introduced by the reparameterization. c) M2 after tomographic filtering; that is, the reparameterized model multiplied with the resolution operator of S20RTS so that it reflects the limited resolving power due to uneven data coverage and damping. A further reduction of heterogeneity can be observed, as well as lateral smearing of structure. See section 2.2 for details on the different parameterizations and the tomographic filtering.

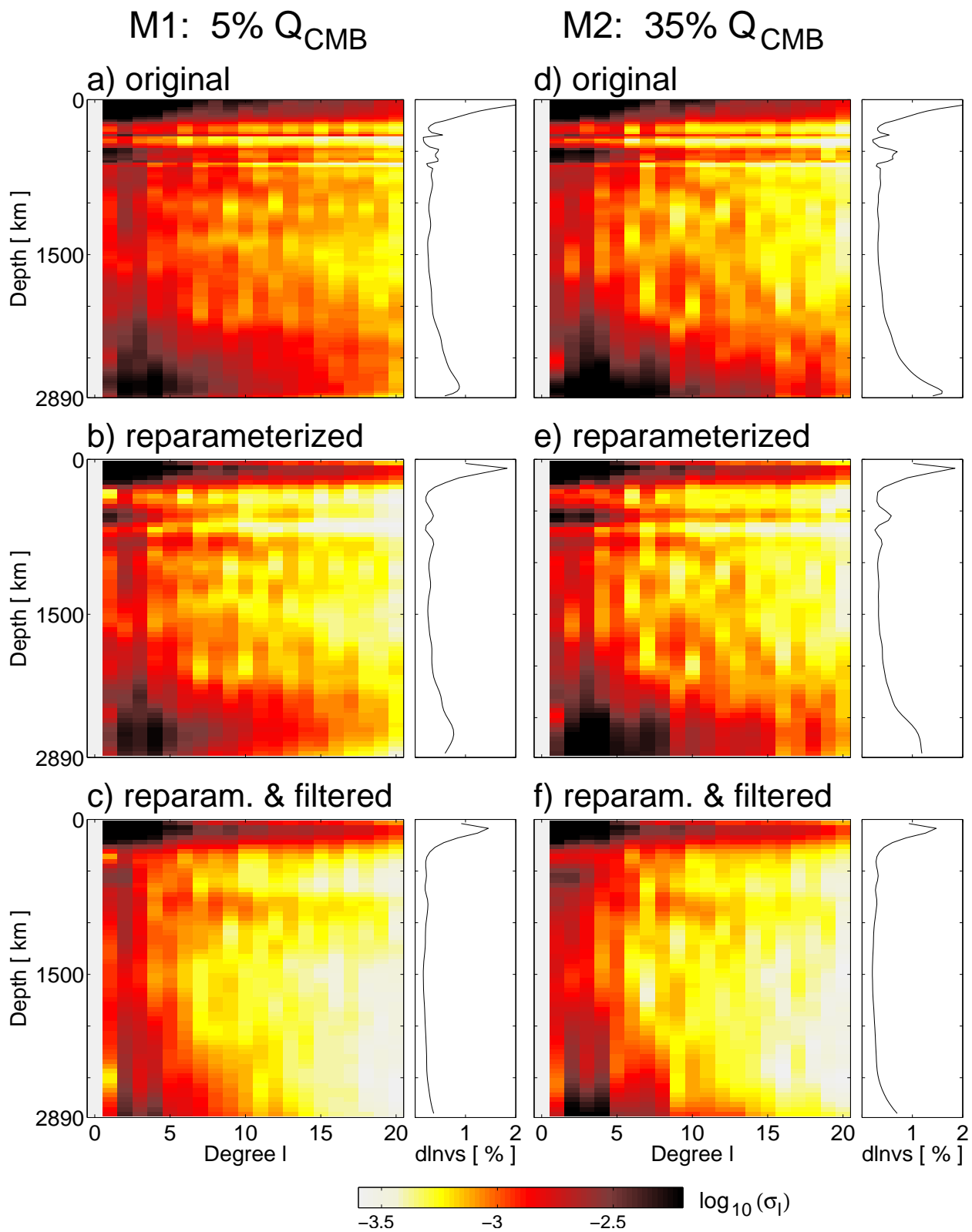




Figure 2.2: Spectral heterogeneity maps (SHM) for mantle circulation models M1 and M2. The spectral power of relative variations in  $v_s$  is given on a logarithmic color scale and plotted as a function of spherical harmonic degree and depth. Small sub-plots on the right of each spectral heterogeneity map show the root-mean-square power up to degree 20. a) SHM for M1 (5% core heating) in the original parameterization, b) for M1 in the parameterization of S20RTS and c) for M1 after tomographic filtering to reflect the resolving power of S20RTS. d–f) SHMs of M2 (35% core heating), accordingly.

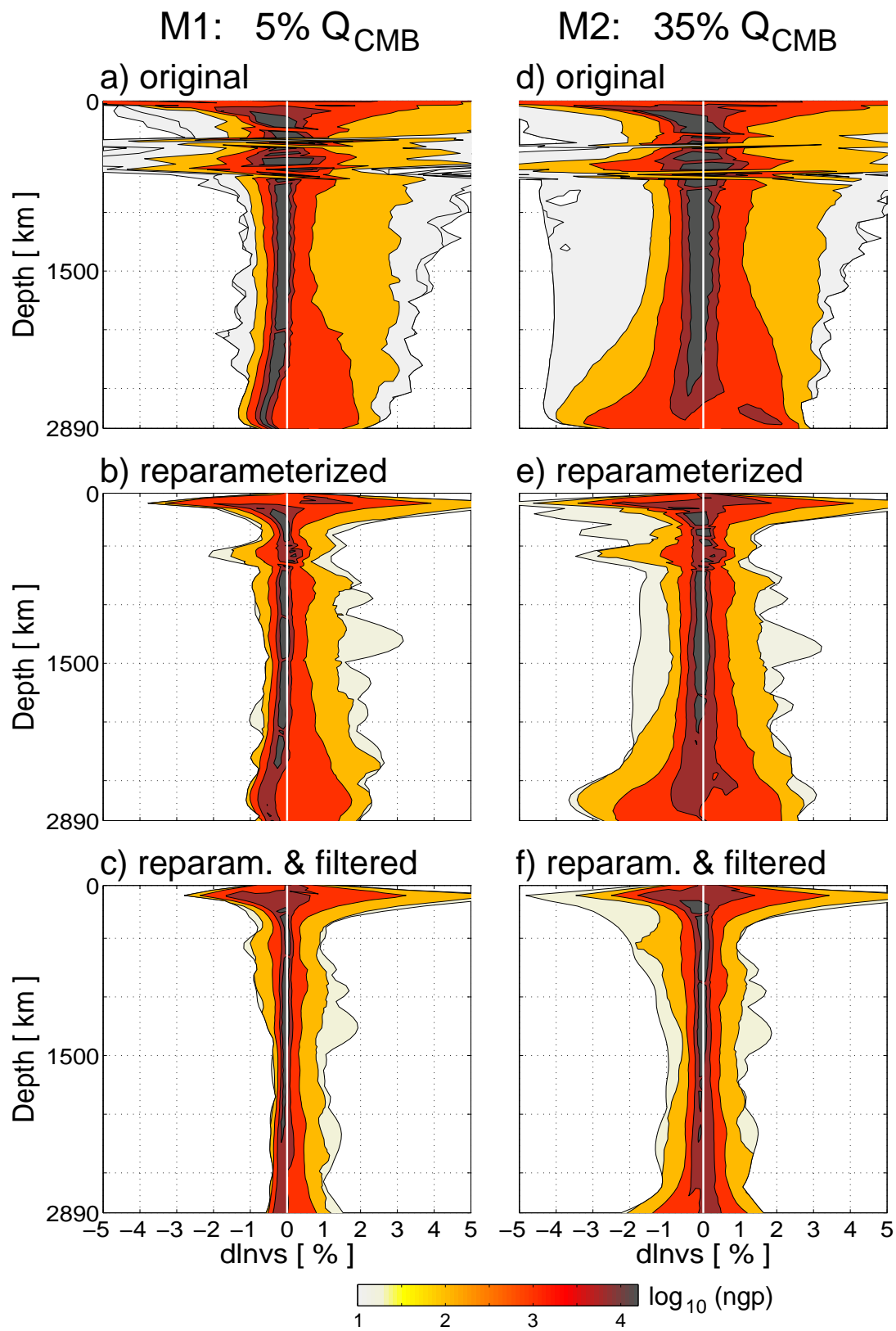


Figure 2.3: Histograms of relative variations in  $v_s$  for mantle circulation models M1 and M2. Logarithmic color scale and contours represent the total number of model grid points ( $ngp$ ) at any given depth (y-axis) as a function of their shear wave anomaly (x-axis) relative to the horizontal mean. Contour lines are plotted for  $\log_{10}(ngp) = 1, 2, 3, 3.8$  and  $4.2$ . The histograms are normalized to the number of grid points in the original parameterization of our models to allow for a direct comparison. a) Histogram for M1 (5% core heating) in the original parameterization, b) for M1 in the parameterization of S20RTS and c) for M1 after tomographic filtering to reflect the resolving power of S20RTS. d-f) Histograms of M2 (35% core heating), accordingly.

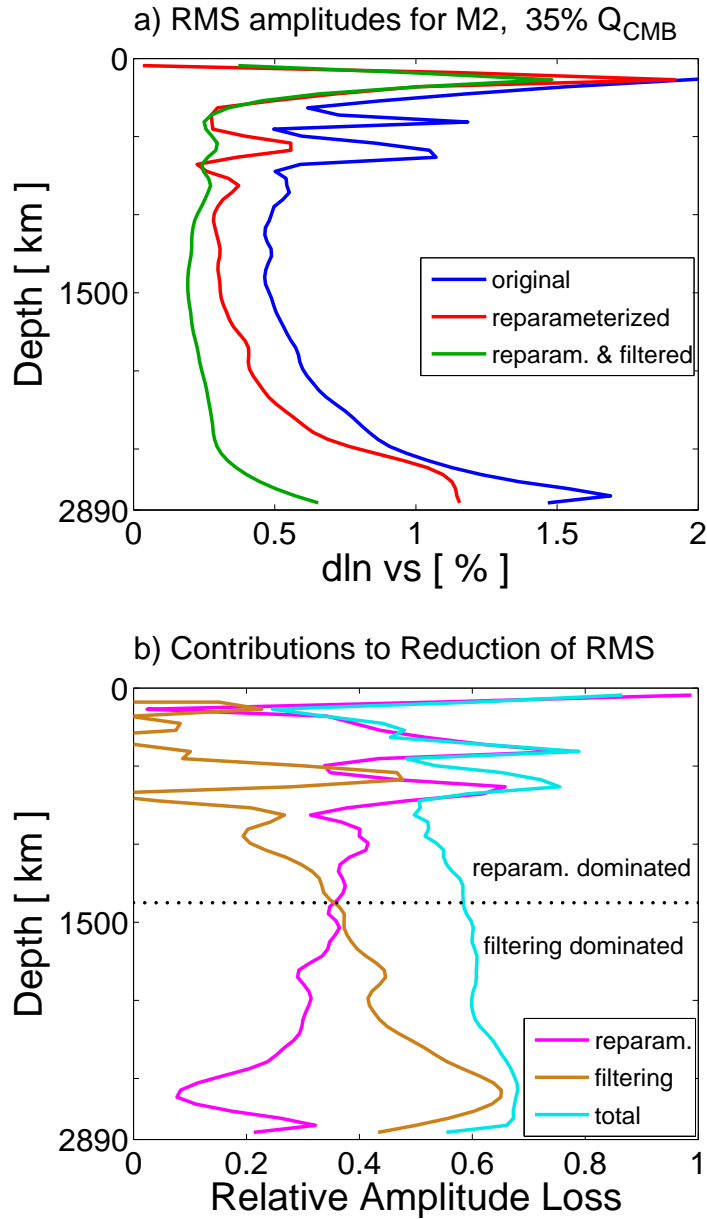


Figure 2.4: a) Root-mean-square amplitudes of heterogeneity in mantle circulation model M2 as a function of depth. RMS profiles of relative variations in  $v_s$  are given for (blue) M2 in the original parameterization, (red) M2 in the parameterization of S20RTS, and (green) M2 after tomographic filtering. b) Relative reduction in RMS amplitudes seen in a). (green) Total relative reduction between the original and the filtered model (i.e., between blue and green line in a). (blue) Relative reduction between the original and the reparameterized model (i.e., between blue and red line in a). (red) Relative reduction between the reparameterized and the tomographically filtered model (i.e., between red and green line in a). Note that the reparameterization predominantly affects the upper half, while the tomographic filtering effects are stronger in the lower half of the mantle. Taken together, the total amplitude reduction is almost constant with depth in the lower mantle.

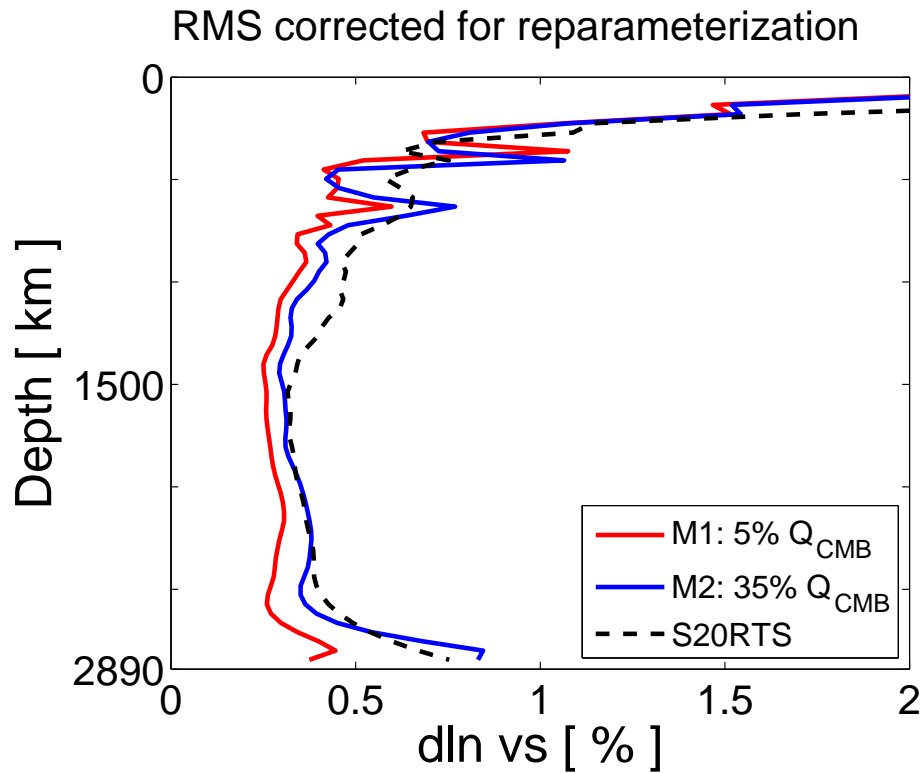


Figure 2.5: RMS profiles of relative variations in  $v_s$  for the tomographically filtered mantle circulation models M1 (red) and M2 (blue), corrected for the effects of reparameterization (see section 2.3.5 for details on the correction). The RMS profile of S20RTS [Ritsema *et al.* 2004] is shown for comparison (black dashed line).

## SHMs corrected for reparameterization

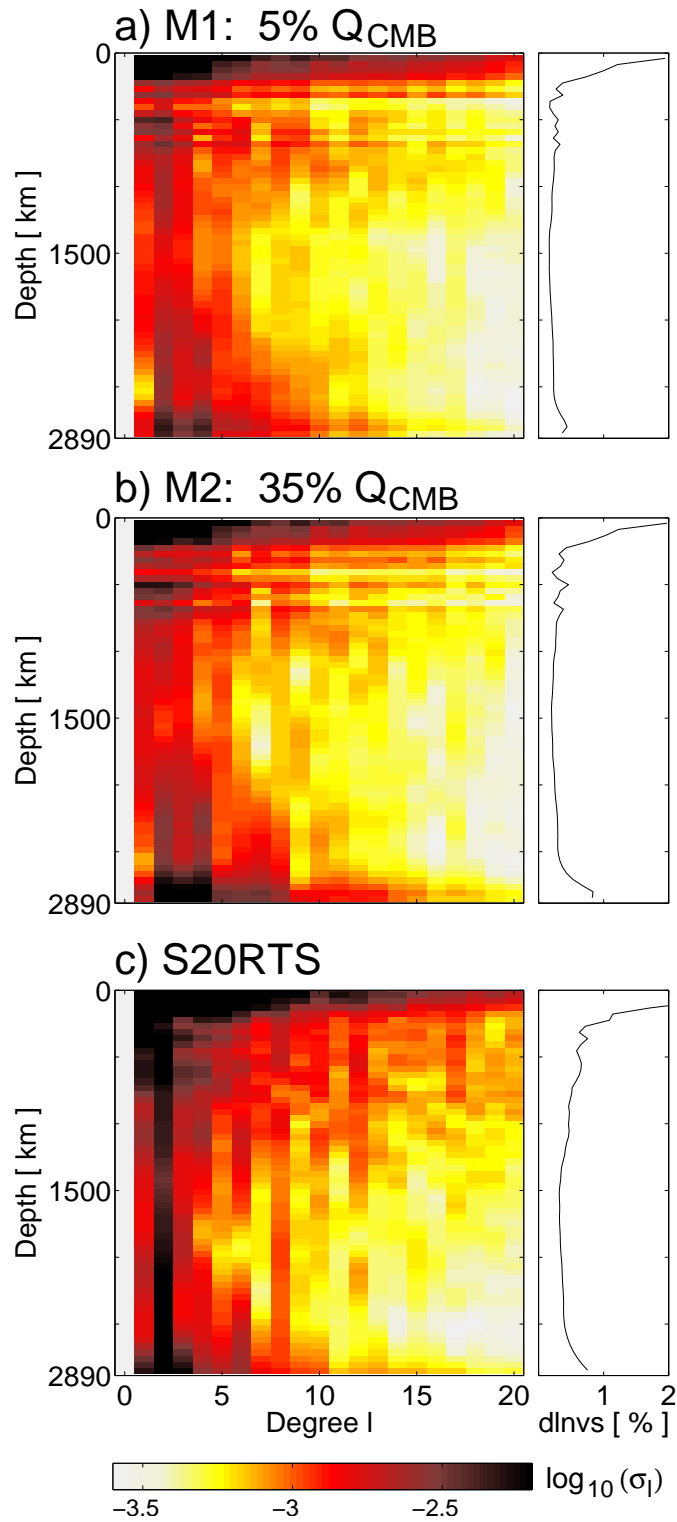


Figure 2.6: Spectral heterogeneity maps for the tomographically filtered models (a) M1 and (b) M2, corrected for the loss of power introduced by the reparameterization (i.e.,  $M1^{f^+}$  and  $M2^{f^+}$ ). Spectral power of  $v_s$  heterogeneity is given on a logarithmic color scale and plotted as a function of spherical harmonic degree and depth. See section 2.3.6 for details on the correction for the effects of reparameterization. c) Spectral heterogeneity map for S20RTS [[Ritsema et al. 2004](#)].

## Histograms corrected for reparameterization

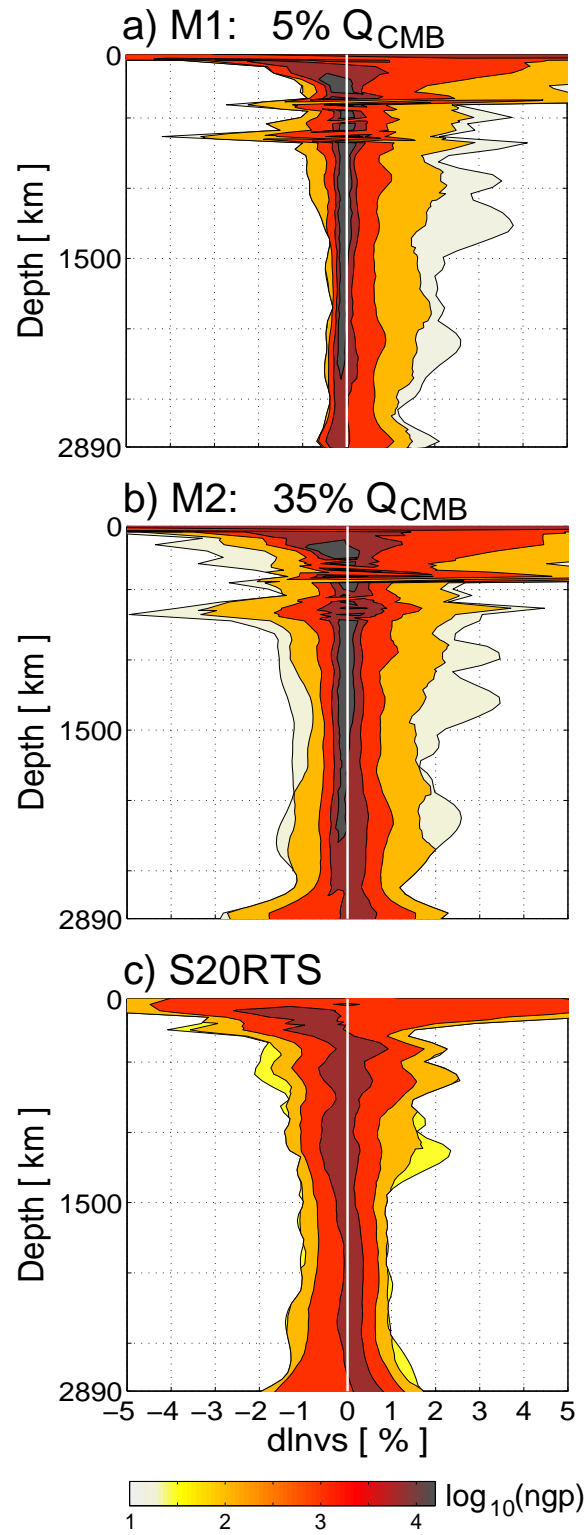




Figure 2.7: Histograms of relative variations in  $v_s$  for the tomographically filtered models (a) M1 and (b) M2, corrected for the magnitude reduction resulting from the reparameterization (i.e.,  $M1^{f^+}$  and  $M2^{f^+}$ ). Logarithmic color scale and contours represent the total number of model grid points ( $ngp$ ) at any given depth (y-axis) as a function of their shear wave anomaly (x-axis) relative to the horizontal mean. Contour lines are plotted for  $\log_{10}(ngp) = 1, 2, 3, 3.8$  and  $4.2$ . See sections 2.3.7 and 2.4 for details on the correction for the effects of reparameterization. (c) Histogram for S20RTS [Ritsema *et al.* 2004]. The histograms are normalized to the number of grid points of the original parameterization of our MCMs to allow for a direct comparison with Figure 2.3. Note the good agreement between M2 and S20RTS for both positive and negative anomalies.



# Conclusions and Outlook

In this study, the first high-resolution mantle circulation models were presented that model global mantle flow at Earth-like convective vigor. The resulting present day temperature fields were post-processed with thermodynamic models of mantle mineralogy for a pyrolite composition to predict seismic heterogeneity, which was then compared to tomographic models. By combining the advances in mineral physics with tools to account for the limited tomographic resolution, a consistent procedure for testing geodynamic models was set up that can also be used in future studies.

## Potential of Studying Magnitudes of Seismic Heterogeneity

The integrative approach for the assessment of geodynamically derived seismic heterogeneity was used here to answer the question whether a strong thermal gradient across  $D''$  is compatible with tomography. The simulations were set up in such a way as to limit the assumption on mantle dynamics made *a priori*. These include a radial viscosity stratification that is in line with geoid observations and post-glacial rebound data. Plate motions were imposed at the upper boundary of the mantle circulation models according to plate tectonic reconstructions. This way, structure predicted from the models is roughly comparable with the geographic pattern of seismic heterogeneity mapped by tomography. However, a direct geographic correlation and comparisons of spectral characteristics seem to be rather poor diagnostics even when the conversion of temperatures into seismic velocities is taken into account.

A key result of this study is that with the approach presented here it is now feasible to specifically consider the magnitudes of predicted heterogeneity in temperature and elastic parameters, thus allowing for quantitative comparisons to tomography. This is made possible by the large computational resources available nowadays together with the existence of mineralogical models that incorporate the full thermodynamic complexity of mantle minerals.

The most important finding with respect to deep Earth structure is that iso-chemical whole mantle flow with a strong heat contribution from the core together with a pyrolite composition are compatible with a number of inferences from seismology. These include the spectral characteristics and, more importantly, the

magnitudes of seismic heterogeneity. Furthermore, also strong gradients in shear wave velocity, as indicated by direct observations of rapid azimuthal traveltimes variations under Africa (i.e., sharp sides of superplumes), can be reconciled with isochemical whole mantle circulation.

As discussed in chapter 2, the effects of uneven data coverage and damping in tomographic inversions are significant, and to warrant entirely consistent comparisons, it is necessary to tomographically filter the geodynamic models. In this respect, a second important result of this work is that the filtering procedure inherently includes an artificial change in the characteristics due to reparameterization that needs to be addressed in the assessment of predicted heterogeneity. Here, it has been attempted to correct for these reparameterization effects, which is possible due to the linear nature of the resolution operator. An interesting observation is that one can relate the amplitude loss introduced by the reparameterization to structural aliasing effects expected in tomographic inversions. The results in chapter 2 demonstrate the feasibility of this correction and clearly strengthen the findings from chapter 1 that isochemical whole mantle flow with a strong thermal gradient across the CMB is compatible with tomography. However, the extent to which structural aliasing actually occurs and thus the exact amount to which the reparameterization has to be corrected for needs further analysis in future studies. It also remains to be seen whether the rise of multi-frequency traveltimes and amplitude, or alternatively adjoint, tomography will result in better resolution of the geometry and amplitude of seismic heterogeneity, which would reduce aliasing effects and thus the discrepancy between resolved and true Earth structure.

A further important outcome of this analysis is that it is crucial to compare geodynamic models with tomography only after conversion of temperatures to seismic velocities. The strong effects of upper mantle mineral phase changes result in significant seismic heterogeneity on length-scales up to spherical harmonics degrees 20. This short-scale heterogeneity in the upper mantle is stronger than the seismic heterogeneity in the lower mantle, which has been noted as a common feature in all tomographic models. This marked feature, however, has sometimes been taken as an indication for a convective separation of upper and lower mantle. In fact, the spectral characteristics of the thermal anomalies described in this work show exactly the opposite trend with stronger heterogeneity in the lower mantle, while the seismic heterogeneity resembles very well the tomographic models. Thus, the present results show that the change in spectral characteristics of these two regions can entirely be related to mineralogical effects in isochemical whole mantle flow with permanent mass exchange across the 660 km discontinuity.

Finally, important further support for strongly bottom heated isochemical whole mantle flow is provided by investigating the consequences of vigorous convection on the stability of Earth's rotation axis, which is given in the appendix A. There, the rotational stability and predicted present day geoid has been ex-

amined and compared to satellite measurements and paleomagnetic inferences on true polar wander. The geoid results show excellent agreement between models and observation at long wavelengths, and furthermore suggest the use of gravity observations to distinguish explicitly between competing plate reconstructions. Importantly, the predicted rate of polar motion in MCMs with strong core heating remains within the paleomagnetic bounds. The fact that Earth's TPW signal can be reconciled with isochemical whole mantle circulation in the presence of a strong active upwelling flow component strengthens the notion of a dominantly thermal origin of mantle heterogeneity.

## Dominance of Thermal Anomalies

The fact that the magnitudes of lateral variations can be explained with the isochemical models presented here has important implications for the possible role of chemical heterogeneity in the large superplumes. As discussed in chapter 1, large thermal variations are to be expected in the lower mantle based on a variety of considerations. The most important argument is the increase of plume excess temperature from the upper to the lower mantle in consequence of mantle subadiabaticity and the temperature dependence of the adiabatic thermal gradient. Thus, positive thermal anomalies of around 1000 K can easily be anticipated for the lower mantle and, as shown in this study, these relate quantitatively to the seismic anomalies mapped by tomographic models. In case of additional chemical heterogeneity, the seismic anomalies will likely be enhanced to values far above the tomographic anomalies. The results of this study thus imply a relatively minor contribution of chemical heterogeneity to the observed lower mantle structure, while not fully precluding its possible existence. Future studies that investigate thermochemical mantle convection should also consider the effects of compositional variations in a quantitative manner, to obtain better estimates of its relative contribution to seismic heterogeneity.

## Perspectives

After having obtained a better understanding of the temperature variations to be expected in a vigorously convecting mantle, the corresponding elastic structures can now be used to compute 3-D whole waveform synthetics. Tools to simulate wave propagation in 3-D structures with complex geometry are, for example, the spectral element [e.g., *Komatitsch and Tromp 1999, 2002a,b*] or alternatively the so-called ADER-DG method [*Käser and Dumbser 2006; Dumbser and Käser 2006*]. The resulting waveforms contain all frequency dependent wave field effects, which will then allow to compare fully synthetic seismograms with data actually observed. In this respect, the challenge for future studies will be to set up synthetic experiments in such a way that new insight into deep Earth structure will be possible. Given the limitations with respect to constraining the pattern

of lower mantle heterogeneity discussed in this thesis, it seems rather unlikely that one can directly compare synthetic waveforms with real seismograms. As a first step, it may be more promising to study statistical characteristics such as distributions of traveltimes variations in continuation of the analysis presented here.

Furthermore, the geodynamically derived seismic heterogeneity generated for this study now makes it possible to start off with the detailed examination of waveform amplitude effects of 3-D variations in seismic velocities. Focusing/defocusing effects are known to result in waveform broadening and amplitude reduction and the question still remains unsolved to what extent this adds on to the inherent dispersive attenuation of visco-elastic material. The predicted seismic heterogeneity can also be used to benchmark seismological techniques by performing, for example, synthetic inversions, as the structures resemble tomography in a statistical sense.

Most of the work presented here was focused on variations in shear wave velocity. Thus, it remains to be seen whether the forward modeling of seismic wave propagation through geodynamic mantle heterogeneity can be used to learn more about the anticorrelation between bulk sound (or density) and shear wave velocity.

This study shows that predicting dynamically consistent thermal models of the mantle through integrative approaches (i.e., solving the equations of motion in combination with mineral physics information and a tomographic resolution analysis) may become an important tool in studies of Earth's deep interior. However, the approach introduced here should be further improved and completed in various ways. First of all, the mineralogical information going into the conversion of temperatures to seismic velocities needs to be updated whenever additional or better experimental data become available. For example, new chemical components and mineral phases will have to be included, such as sodium oxides, hydrous phases and the possible occurrence of post-perovskite in the lower mantle. Water may have important influence on structure in the transition zone, while post-perovskite is likely to occur in cold regions of  $D''$  and may thus have strong influence on predicted seismic heterogeneity. However, the contributions from both post-perovskite and water being restricted to certain locations and thermal regime, they will probably not affect the current results on plume excess temperatures in the lower mantle and their compatibility with seismic anomalies mapped by tomography. Finally, it will be important in future to build elastic models that are fully self-consistent by computing densities directly from the thermodynamic mineralogical models already in the convection simulations. This idea has been explored in simple Cartesian 2-D simulations and is planned to be incorporated into the full 3-D spherical mantle circulation models as a continuation of this work.

# Appendix





# Appendix A

## Rotational Stability and Geoid of High-Resolution Mantle Circulation Models<sup>\*</sup>

### Abstract

Growing evidence points to a substantial heat flow across the Core Mantle Boundary, but the rotational stability of strongly bottom heated mantle flow with prominent upwelling plumes is poorly known. Here we calculate polar motion for the past 100 million years (Ma) induced in a new class of isochemical high resolution mantle circulation models (MCM) with Earthlike convective vigor and up to 12 TW core heat flux. Our MCMs include internal heating, and a simple three layer viscosity profile associated with the lithosphere ( $10^{23}$  Pas), the upper ( $10^{21}$  Pas) and the lower mantle ( $10^{23}$  Pas), separated at 100 and 650 km depth, respectively. A published mantle mineralogy model in the pyrolite composition, consistent with our assumption of whole mantle flow, allows us to relate thermal to density variations in a thermodynamically self-consistent way. All models yield modest polar motion on the order of 0.5 degrees/Ma or less, in accordance with paleomagnetic data, and agreeing with a number of studies that demonstrate the stabilizing effect of the rotational bulge. Although a substantially reduced lower mantle viscosity would increase this rate, the good agreement between MCM and seismic mantle heterogeneity lends independent support for our viscosity profile, as otherwise slabs in the MCM would rapidly sink to depth levels where they are tomographically not observed. In general, there is good agreement between the long wavelength geoids predicted from our MCMs and recent satellite derived

---

<sup>\*</sup>Appendix A is based on the diploma study of Katrin Schaber [[Schaber 2008](#)], which was co-supervised by the author and is in submission to “Geochemistry, Geophysics, Geosystems”: Schaber, K., H.-P. Bunge, B. S. A. Schuberth and R. Malservisi (2009), *Rotational stability and geoid of a strongly core heated Earth*, *Geochem. Geophys. Geosyst.*, *subm.*

models of Earth's geoid (correlation coefficient of around 0.4), but noticeable differences at intermediate wavelengths, for example in the western Pacific and in Africa, suggest the use of gravity data to distinguish between competing plate reconstruction models.

## A.1 Introduction

True polar wander (TPW), the coherent motion of the Earth's surface with respect to its rotation axis, is most likely controlled by redistribution of deep seated mass anomalies due to vigorous convection inside the Earth's mantle. Paleomagnetic evidence suggests that this motion has been small, not exceeding more than 10–15° of latitudinal variation during the past 100 million years (Ma) [*Besse and Courtillot 1991, 2002; Tarduno and Smirnov 2001*]. Thus, the rate of TPW has been on average only about 0.1° to 0.2° per Ma.

The apparent stability of the Earth's rotation axis is at odds with results from isoviscous whole mantle convection models, which predict much faster TPW rates on the order of 1° to 10° per Ma [*Richards et al. 1999*]. The rate slows to about 0.5° per Ma for mantle convection with a high viscosity lower mantle due to the large-scale planform induced by depth-dependent viscosity [*Bunge and Richards 1996*]. Thus, the most plausible explanation for the Earth's small TPW rests with the great stability of the upper thermal boundary layer of the mantle, the lithosphere, and the gradual movement of its major subduction systems. Confirmation for this comes in the form of analytic models, where subduction histories or advected mass anomalies inferred from seismic tomography are used to estimate the time evolution of mantle heterogeneity for the Cenozoic and Mesozoic [*Richards et al. 1997; Steinberger and OConnell 1997*].

It may seem obvious to consider mass anomalies from the upper thermal boundary layer in the excitation of TPW. More interesting is the fact that geodynamicists have long assumed the lower thermal boundary layer at the core-mantle boundary (CMB) to be of less importance, an assumption that stems from a classic argument involving the modest dynamic topography observed over hotspots. This has been taken to suggest a minor core heat flux contribution of about 5% ( $\sim 1.5$  TW) to the global mantle heat budget [*Sleep 1990; Davies 1988*], implying that hot thermal upwellings in the deep mantle play a secondary role in the dynamics of the Earth.

A number of geodynamic studies have called this assumption into question. They favor a high core heat flux in order to overcome problems of insufficient internal mantle heat sources [*Kellogg et al. 1999*], or to satisfy constraints on the power requirement of the geodynamo [*Glatzmaier and Roberts 1995; Kuang and Bloxham 1997*] and the thermal history of the core [*Buffett 2002; Nimmo et al. 2004*]. The notion of strong core heating is further supported by novel

tomographic imaging techniques, which reveal a variety of lower mantle plumes [*Montelli et al. 2004*].

A key argument for high core heat flux involves the non-adiabatic nature of the mantle geotherm away from thermal boundary layers [*Jeanloz and Morris 1987*], which arises from internal radioactive heat production and secular cooling of the mantle. Several studies have concluded that the mantle geotherm departs by as much as 500 K from the adiabat [*Bunge et al. 2001; Monnereau and Yuen 2002; Sleep 2003*]. The net effect of mantle non-adiabaticity is a strong thermal gradient and a correspondingly high heat flux across the CMB, as large as 15–30% (5–10 TW) of the total mantle heat loss [*Bunge 2005; Mittelstaedt and Tackley 2006; Leng and Zhong 2008; Lay et al. 2008*]. Thus bottom heating and buoyant mass anomalies from a lower thermal boundary layer (i.e., plumes) may affect the mantle general circulation and the rotational stability of the Earth more prominently than what is commonly assumed.

Modeling the mantle general circulation has made great progress in the last decade. Based on the conservation laws for mass, momentum, and energy, geodynamicists have constructed so called mantle circulation models (MCMs) to explore the structure of mantle heterogeneity and its temporal evolution in realistic 3-D spherical geometry [*Bunge et al. 1998, 2002; McNamara and Zhong 2005*]. MCMs involve conductive and advective heat transport and account explicitly for density heterogeneities originating from the lower thermal boundary layer in addition to density anomalies associated with past subduction [*Ricard et al. 1993a*].

Rapid growth of computational resources allows one to explore MCMs at very high numerical resolution. In fact, models with more than 80 million finite elements and a grid point resolution of less than 30 km globally are feasible now [*Oeser et al. 2006*]. With this resolution one can study highly time dependent mantle circulation at earthlike convective vigor with a thermal Rayleigh number of  $10^9$  based on internal heating. Put differently, one can resolve a characteristic thermal boundary layer thickness on the order of 100 km in the mantle, comparable to that represented by the oceanic lithosphere.

A key motivation for high numerical resolution in MCMs is the ability to model lateral and radial temperature variation comparable in magnitude to those expected in the Earth. This is essential to exploit recent progress in high pressure petrology, which makes it possible to build thermodynamically self-consistent mantle mineralogy models [*Stixrude and Lithgow-Bertelloni 2007; Piazzoni et al. 2007*], and to convert every P,T,x (pressure, temperature, composition) condition of the mantle to a stable phase assembly and its corresponding physical properties such as density.

The density structure predicted this way from a high resolution MCM with substantial core heating (35% of the surface heat loss) is shown in Figure 1 (see Figure caption and Table 1.1 for modeling parameters). To keep things simple, a three layer viscosity profile is assumed in agreement with geoid [e.g., *Hager*

and Richards 1989] and post glacial rebound studies [e.g., Mitrovica 1996]. The choice of pyrolite as compositional model [Ringwood 1975; Irifune 1987] to map thermal into density variations is consistent with the implicit assumption of whole mantle flow. A detailed analysis of the thermal structure of this model and its corresponding elastic heterogeneity is given in [Schuberth et al. 2009].

In this paper, we explore the effects of substantial core heat flux on the rotational stability of MCMs, testing the hypothesis that strongly bottom heated mantle flow is compatible with the record of Mesozoic and Cenozoic polar motion. Geodynamic mantle heterogeneity is computed from high resolution MCMs as in [Schuberth et al. 2009] and geoids and TPW are then calculated analytically from the density anomalies taking the same viscosity profile assumed in the MCMs. This assures consistency between modeled mantle heterogeneity and its geoid and TPW response.

Aside from geodynamic parameters such as viscosity stratification or CMB temperature, the density structure of MCMs is directly affected by past plate motion models. Such models are assimilated into MCMs to organize the temporal evolution of the flow and to direct the location of major downwellings. The plate motion models are limited to the past 100–150 Ma, the age of the oldest ocean floor. A widely adopted model, which spans the past 120 Ma by building on the Cenozoic reconstructions of [Gordon and Jurdy 1986], was introduced by [Lithgow-Bertelloni and Richards 1998]. However, alternative plate reconstructions have been proposed [Hall 2002; Quere et al. 2007; Müller et al. 2008]. These models suggest different plate geometries for the Mesozoic and therefore imply substantial uncertainties in the modeled mantle density structure and its temporal evolution. One must consider these uncertainties in addition to the inherent uncertainties in modeling parameters and initial conditions when assessing predictions from mantle circulation modeling for the evolution of Mesozoic and Cenozoic mantle flow.

We organize our paper as follows: Starting from a short description of the computational methods and parameters employed in the MCMs, we briefly review the theory and analytic methods involved in geoid and TPW computation. Our geoid results show excellent agreement (correlation  $> 40\%$ ) between models and observation at long wavelengths, and furthermore suggest the use of gravity observations to distinguish explicitly between competing plate reconstructions. Importantly, we find that the predicted rate of polar motion in MCMs with strong core heating remains within the paleomagnetic bounds, which indicates that the Earth’s TPW signal can be reconciled with isochemical whole mantle circulation having a strong active upwelling flow component.

## A.2 Model Setup

We model the circulation of the mantle using the parallel finite element TERRA code [Bunge and Richards 1996; Bunge et al. 1997]. Input parameters are summarized in Table 1.1 and equivalent to Schubert et al. [2009]. The code solves for momentum and energy balance of a highly viscous fluid at infinite Prandtl number (no inertial forces) in a spherical shell corresponding to the Earth’s mantle. The modeling domain is discretized with a mesh derived from the icosahedron to assure an almost uniform grid spacing at each radial level. A global grid spacing of around 25 km, resulting in 80 million finite elements, allows us to model mantle circulation at earth-like convective vigor, expressed by a thermal Rayleigh number of  $10^9$  based on internal heating. This is about ten times the value explored in earlier MCMs [Bunge et al. 2002] and yields highly time-dependent flow.

The rheologic stratification of our MCMs is a simple three layer viscosity profile. The layers are identified with the lithosphere, the upper mantle and lower mantle, which are separated at 100 and 650 km depth. The assigned viscosities are  $10^{23}$ ,  $10^{21}$  and  $10^{23}$  Pa.s, respectively, in agreement with geoid [e.g., Hager and Richards 1989] and post glacial rebound studies [e.g., Mitrovica 1996]. Mechanical boundary conditions are always free-slip at the CMB (the core supports no shear-stress), while the surface velocities are specified according to the plate motion history of Lithgow-Bertelloni and Richards [1998].

The thermal boundary conditions are constant temperature at the surface (300 K) and the CMB. In order to clearly isolate the effects of bottom heating, we focus on three MCMs (M1–M2), where we vary the CMB temperature in such a way as to produce models with weak or strong core heat flux while keeping all other model parameters constant (see Table 1.1). M1 is a standard MCM with mostly internal heating. A modest CMB heat flux of 1.5 TW (around 5% of the total surface heat flow) is accomplished in this model by setting the CMB temperature to 2900 K. M1.5 has an intermediate core heat flux of 6 TW (roughly 20% of the surface heat flow) obtained from a CMB temperature of 3500 K. A rather high core heat flux of 12 TW (around 35% of the total surface heat flow) results in M2 from setting the temperature at the CMB to a value of 4200 K. M1 and M2 are end-members in terms of core heating with Urey numbers (the ratio of internal heating to total surface heat loss) of 0.95 and 0.65, respectively, and span a reasonable range of core heat flux values. The values of CMB temperature and core heat flow are summarized in table A.1

Density anomalies for either the present day or earlier geologic times (in case of TPW calculations) of M1–M2 are obtained from mapping absolute temperatures into the corresponding absolute densities, which are afterwards referenced to the mean values in each radial layer. For this conversion, we take advantage of a recently published thermodynamically self-consistent model of mantle mineralogy [Piazzoni et al. 2007]. The model is based on physical measurements (e.g., equation of state by X-ray diffraction, phase equilibria, calorimetric data) of ma-

terial properties in the CFMAS (CaO – FeO – MgO – Al<sub>2</sub>O<sub>3</sub> – SiO<sub>2</sub>) system. As noted in section A.1, we assume a pyrolite bulk composition to convert the P,T condition at each model grid point to its corresponding density consistent with our assumption of whole mantle flow.

## A.3 Analysis of Mass Anomalies in the Mantle

### A.3.1 Geoids

Computation of the geoid from the geodynamic density structure is carried out with the well known analytic formalism of geoid kernels [*Richards and Hager 1984; Ricard et al. 1984*]. The kernels  $K_l(r')$  give the geoid anomaly at the surface in meters for a unit probing mass anomaly at each depth and degree of spherical harmonics. Their sign (positive or negative) and shape show, whether contributions to the gravitational signal coming from the mass anomaly or the induced deformation of internal and external interfaces (notably the surface and the CMB) prevail. The geoid anomaly  $N$  is obtained by a multiplication of the kernel  $K_l(r')$  and the mass anomaly at each depth  $r'$  integrated from the CMB,  $c$ , to the surface,  $a$

$$N_{lm} = \int_c^a K_l(r') \rho_0(r') \delta \rho_{lm}(r') dr' \quad (\text{A.1})$$

$$= \int_c^a \frac{\delta U(a, \delta \rho_{lm}(r') = 1)}{g(a)} \rho_0(r') \delta \rho_{lm}(r') dr' \quad (\text{A.2})$$

where  $N_{lm}$  and  $\delta \rho_{lm}$  are the expansion coefficients in spherical harmonics of the geoid and the mass anomalies, and  $\rho_0$  is the reference density in the mantle. In equation (A.1), incompressibility of the mantle is assumed. We note, however, that compressibility would have only with minor effects for viscosity structure used here [*Panasjuk et al. 1996*].

Figure A.2 shows the kernels for the three-layer viscosity profile used in our MCMs. The kernels are zero at the surface and the CMB, as isostatic adjustment is assumed at these two boundaries, and change sign within the mantle. For spherical harmonic degree two, which is prominent in the Earth's gravity field, the kernel nearly vanishes in the uppermost 100 km, is positive between 80 km and 1200 km depth and negative otherwise, so that deeply seated positive mass anomalies in the lower mantle, such as subducted slabs, result in geoid lows, while negative mass anomalies, such as upwelling plumes are associate with geoid highs.

Using the dimensionless normalized Stokes coefficients  $C_{lm}$  and  $S_{lm}$  equation (A.1) can be rewritten [Lambeck 1988]

$$\begin{aligned}
 N(\lambda, \phi) &= R_e \left[ \sum_{l=2}^{\infty} \sum_{m=0}^l (C_{lm} \cos m\lambda \right. \\
 &\quad \left. + S_{lm} \sin m\lambda) P_{lm}(\sin\phi) \right] \\
 \text{with } C_{lm}(R_e) &= \frac{R_e}{M} \sum_{r'} K_l(r') \rho_0(r') \delta\rho_{lm}^C(r') \Delta r \\
 S_{lm}(R_e) &= \frac{R_e}{M} \sum_{r'} K_l(r') \rho_0(r') \delta\rho_{lm}^S(r') \Delta r,
 \end{aligned} \tag{A.3}$$

where  $P_{lm}$  are the associated Legendre Polynomials,  $\delta\rho_{lm}^C$  and  $\delta\rho_{lm}^S$  are the two real expansion coefficients of  $\delta\rho$ . The integration in equation (A.1) is approximated by a sum.

Figure A.3 shows the observed geoid and the geoids predicted from the density anomalies of M1–M2 up to degree and order 20. The observed non-hydrostatic geoid (Figure A.3a) is obtained from the latest satellite-only gravity model GL04S1 [Förste et al. 2007; Nakiboglu 1982]. It shows major geoid highs over Africa and the western Pacific, with a great circle band of geoid lows in the intervening region. Note that the proximity of the African geoid high to the position of the former supercontinent Pangaea has been taken early on to suggest anomalously warm, buoyant mantle in this region due to continental insulation [Anderson 1982]. The prominent regional geoid high in the western Pacific is explained by upper mantle slabs [Hager 1984], and it is now widely agreed that the major geoid lows correspond to the history of subduction and lower mantle slabs [Richards and Engebretson 1992; Ricard et al. 1993a].

The density structure from our MCMs confirms this interpretation. The modeled geoids (Figs. A.3b–d) for varying core heating (CH) agree well with the observed geoid in shape and amplitude (−114/77m, 5% CH; −115/77m, 20% CH; −133/99m, 40% CH; −121/107m, observed) since their density structure is controlled mainly by the assimilated plate motion history. Models with higher core heat flux have a larger geoid amplitude, as expected, due to the additional buoyancy associated with hot upwellings.

Apart from the generally good agreement, there are important differences between modeled and observed geoids. For example, all models produce a geoid low in eastern Asia of much larger amplitude than observed, and there is also a minor geoid low over central Africa. It is likely that these differences arise from errors in the assumed subduction history, as we will see later on.

Figure A.4 shows the spectral power of the observed and modeled geoids, and the correlation between models and observation at each spherical harmonic degree. The correlation per degree  $C(l)$  and the total correlation  $C^L$  are computed

as follows from the Stokes coefficients of the measured and the computed geoid ( $C_{lm,M}$ ,  $S_{lm,M}$  and  $C_{lm,C}$ ,  $S_{lm,C}$ ) [Hager 1984; Ricard et al. 1993a]:

$$C(l) = \frac{\sum_{m=0}^l (C_{lm,M}C_{lm,C} + S_{lm,M}S_{lm,C})}{\sqrt{\sum_{m=0}^l (C_{lm,M}^2 + S_{lm,M}^2) \sum_{m=0}^l (C_{lm,C}^2 + S_{lm,C}^2)}}$$

$$C^L = \frac{\sum_{l=0}^L \sum_{m=0}^l (C_{lm,M}C_{lm,C} + S_{lm,M}S_{lm,C})}{\sqrt{\sum_{l=0}^L [\sum_{m=0}^l (C_{lm,M}^2 + S_{lm,M}^2) \sum_{m=0}^l (C_{lm,C}^2 + S_{lm,C}^2)]}}.$$

The spectral power per degree agrees well between observed and modeled geoids, except for degree two, which is too small in all MCMs, and degrees seven and eight, which are too large.

Agreement in the large-scale pattern of modeled and observed geoids is evident from the high correlation at the lowest spherical harmonic degrees, two, three and five. There is anticorrelation at degree four, but the spectral amplitude of this degree is small. At higher spectral degrees the correlation varies considerably. For example, degrees nine, eleven and eighteen are strongly anti-correlated with the observed geoid (up to  $-40\%$ ), while degrees ten, twelve, seventeen and twenty correlate positively, up to  $35\%$ .

### A.3.2 True Polar Wander

The aspiration of a rotating body to turn around its largest principal axis of inertia in order to minimize energy is expressed in the conservation of torque, which is described in a rotating reference system tied to the angular velocity  $\omega$  of the Earth. No external torques and no internal angular momenta are assumed; the resulting equation of motion for the Earth's pole is called the Liouville equation:

$$\frac{d}{dt}\mathbf{H} + \omega \times \mathbf{H} = 0,$$

where the angular momentum  $\mathbf{H}$  can be written in terms of the full inertia tensor  $\mathbf{I}(t)$

$$\mathbf{H}(t) = \mathbf{I}(t) \cdot \omega.$$

$\mathbf{I}(t)$  may be decomposed into three parts, noting  $\delta_{ij}$  the Kronecker symbol

$$I_{ij} = I_0\delta_{ij} + I_{ij}^c + \Delta I_{ij}. \quad (\text{A.4})$$

The first term  $I_0 = 0.33 MR_e^2$  is the inertia tensor of a spherical non-rotating Earth with a mass  $M$  and a radius  $R_e$ . The second term  $I_{ij}^c$  is due to the centrifugal potential and represents the rotational bulge, which controls the rate of



polar motion. The last term  $\Delta I_{ij}$  describes changes in the inertia due to internal mass redistributions, that is the excitation function [Ricard *et al.* 1993b], and relates linearly to the Stokes coefficients of degree two, describing the variations of the geoid from the planet's hydrostatic ellipsoid given in equations (A.4). This relation is called McCullagh's formula [e.g., Munk and McDonald 1960]

$$\begin{aligned}
 \Delta I_{11} &= MR_e^2 \left( \frac{1}{3} \sqrt{5} C_{20} - 2 \sqrt{\frac{5}{12}} C_{22} \right) \\
 \Delta I_{22} &= MR_e^2 \left( \frac{1}{3} \sqrt{5} C_{20} + 2 \sqrt{\frac{5}{12}} C_{22} \right) \\
 \Delta I_{33} &= -MR_e^2 \frac{2}{3} \sqrt{5} C_{20} \\
 \Delta I_{12} &= -MR_e^2 2 \sqrt{\frac{5}{12}} S_{22} \\
 \Delta I_{23} &= -MR_e^2 \sqrt{\frac{5}{3}} S_{21} \\
 \Delta I_{13} &= -MR_e^2 \sqrt{\frac{5}{3}} C_{21}.
 \end{aligned} \tag{A.5}$$

The Stokes Coefficients of the non-hydrostatic geoid already contain the viscoelastic deformation due to mass anomalies in the Earth's mantle as given by the geoid kernels or equivalently by the  $(1 + k_L(t, R_e))$ ,  $k_L$  being the load Love number [Richards and Hager 1984].

The centrifugal part  $I_{ij}^c$  describes the time-dependent behavior of the equatorial bulge and thus is equal to the convolution of the tidal Love number  $k^T(t)$  with the time history of the changes in the centrifugal potential.

$$I_{ij}^c(t) = \frac{R_e^5}{3G} k^T(t) * \left[ \omega_i(t) \omega_j(t) - \frac{1}{3} \omega^2(t) \delta_{ij} \right],$$

where  $G$  is the gravity constant and the star represents the time convolution. The tidal Love number  $k^T(t)$  describes the viscoelastic relaxation of the Earth's rotational bulge. For the long time scales associated with mantle flow it is referred to as the quasi fluid love number and decomposes into the relaxation time of the bulge  $T_1$  and the time independent fluid love number of degree two  $k^T$  [see Ricard *et al.* 1992, 1993b; Greff-Lefftz 2004]. The MCM viscosity profile (shown in Figure A.2) combined with the density and rigidity structure of PREM [Dziewonski and Anderson 1981] yields  $T_1 = 49.847$  ka and  $k^T = 0.9339$  in our models.

The solution of the Liouville equation is carried out backwards in time with the initial position of the pole being at the largest principal axis of inertia of present time.

In Figure A.5a, we track the polar motion induced in the three MCMs for the past 100 Ma. Dark blue denotes M1 with 5% CH, light blue denotes M1.5

with 20% CH, and red shows the TPW for M2 with 35% CH. The TPW path is similar in all models. Going back in time, we see that the paths start at the present position of the North Pole, travel south-east up to about 40 Ma before present (BP), and then change direction by moving south-south-west until 100 Ma BP. Note that the TPW amplitude does not exceed  $20^\circ$  in any of the models ( $19.71^\circ$  for M1,  $16.35^\circ$  for M1.5 and  $18.69^\circ$  for M2).

The largest principle axis of inertia (PIA) for each time step and model is shown Figure A.5b, on the same color code as A.5a. Again there is little difference between the models with high and low core heat flux. Starting from the present north pole the PIA moves north-east up to about 20 Ma BP, and south-west for prior times. In M1.5 and M2 the PIA lie on the southern hemisphere for the earliest time steps, and are depicted with opaque circles.

The paleomagnetically interesting rate of TPW for our models is shown in Figure A.5c together with a paleomagnetic bound ( $0.45^\circ\text{Ma}^{-1}$ ) over the past 100 Ma taken from *Besse and Courtillot [2002]*. The most rapid motion of up to  $0.425^\circ\text{Ma}^{-1}$  occurs in the last 20 Ma, where models with stronger core heating (M1.5 and M2) are somewhat faster than M1, but not by much. At earlier times the motion slows to less than  $0.3^\circ\text{Ma}^{-1}$  in all models.

To better illuminate the core heating effect on the mantle density structure and induced polar motion we track the temporal evolution of large scale density heterogeneity in our models (M1–M2) in Figure A.6. Contoured is the spectral amplitude at spherical harmonic degree two as a function of depth and time together with the geoid kernel of degree two. The most noticeable feature in Figure A.6 is the strong correspondence between degree two heterogeneity at the CMB and increasing core heat flux, which illustrates the influence of bottom heat on deep mantle mass heterogeneity (plumes) rather well. In M1 the amplitude of degree two in the lowermost 500 km amounts to  $1.0\text{ kg m}^{-3}$  over the last 100 Ma. But it is closer to  $3.0\text{ kg m}^{-3}$  in M1.5 and exceeds  $4.0\text{ kg m}^{-3}$  in M2. However, we noted before that the geoid kernel acts as weighting function for the gravitational effects of density anomalies, and that the kernel approaches zero at the CMB due to isostatic compensation. Thus the strong amplitude of degree two heterogeneity near the CMB is ineffective in changing the spectral amplitude of the geoid (Figure A.4) and the rotational behavior (Figure A.5a) in a significant way.

## A.4 Discussion

### A.4.1 Rotational Stability

Arguably, the most important result of our study is the rotational stability of MCMs in the presence of strong core heating. Apart from the isochemical, pyrolytic nature of the models, we have made three basic assumptions on character

and temporal variability of the MCM density structure: 1) a large-scale mantle flow related to past plate motion, 2) a radial viscosity profile in agreement with post-glacial rebound and geoid observations, and 3) a significant contribution to the MCM energy budget from the lower thermal boundary layer, as large as 9–12 TW. The first two assumptions are widely agreed upon by geodynamicists, and the rotational stability of geodynamic mantle models constructed under this premise has been verified explicitly [Ricard *et al.* 1993a; Richards *et al.* 1997].

The third assumption instead represents a considerable departure from traditional views of large-scale mantle dynamics and the partitioning of buoyancy forces from the upper and lower thermal boundary layer, although it is promoted by a variety of geodynamic considerations and by a range of seismological and mineral physics studies. For example, a substantial core heat loss is consistent with tomographic inferences of strong lower mantle plumes [Nolet *et al.* 2006], and with seismological constraints for a high CMB temperature ( $3950 \pm 200$  K) deduced from inverse scattering of core-reflected shear waves (ScS) *van der Hilst et al.* [2007]. Moreover, high-pressure experiments on the melting temperature of iron alloys and first-principle calculations on the elastic parameters and melting curve of iron under core conditions also support the notion of strong bottom heating in the mantle, by pointing to an elevated CMB temperature ( $4000 \pm 200$  K) and a correspondingly high core heat flux [Boehler 2000; Steinle-Neumann *et al.* 2001; Alfè *et al.* 2002].

The small displacement of the rotation axis in our MCMs can be seen from Figure A.5 where it is evident that differences in core heat flux do not translate into significantly different pole paths: in fact, direction, amplitude and speed of the modeled TPW remains similar among the MCMs. For example, TPW rate and amplitude (modeled at  $< 0.425^\circ/\text{Ma}$  and  $19.71^\circ$ , respectively) stay within the paleomagnetic bounds ( $0.5^\circ/\text{Ma}$  and total displacement of the rotational axis of  $< 15\text{--}20^\circ$  in 100 Ma) suggested by Besse and Courtillot [2002]. The result is not entirely unexpected. Several studies have concluded that as lower mantle viscosity is raised from  $10^{22}$  Pa s to  $10^{23}$  Pa s TPW drops to  $< 0.5^\circ$  per Ma due to the retarding effect of the rotational bulge [Ricard *et al.* 1992, 1993b; Greff-Lefftz 2004; Mitrovica *et al.* 2005; Tsai and Stevenson 2007]. Our models confirm this by showing that the spin axis follows the motion of the largest principal axis of inertia rather slowly. Thus any short term variations in the inertia tensor due to upwelling plumes are effectively damped and translate into minor changes of the TPW path.

It is worth noting in this context that we apply the same viscosity profile in the computation of the MCM density structure and its associated TPW. Importantly, upon lowering the deep mantle viscosity of our models substantially, we observe that considerable differences arise between the MCMs and seismically observed mantle heterogeneity. Put differently, Mesozoic and Cenozoic slabs in our MCM approach mantle depth levels where they are not imaged seismically if a lower viscosity is used for the deep mantle. This observation lends independent support

for our choice of a substantial increase in lower mantle viscosity. Equally relevant to the rotational stability of our models is the fact that core heating influences the MCM density distribution primarily in the vicinity of CMB on the lowermost mantle, as can be seen in figure A.6. This limits their impact on the inertia tensor, because the geoid kernels approach zero in the lowermost mantle.

### A.4.2 Geoid

The largest principal axis of inertia at present time and the spin axis of our models coincide with the Earth (Figure A.5a and b). This match — which should not be expected *a-priori* — confirms the high correlation between observed and modeled geoid (at degree two) and agrees with earlier findings which demonstrate that the observed geoid can be explained rather well from mantle density structures related to past subduction [Ricard *et al.* 1993a; Steinberger 2000]. The result, however, must be qualified as we have ignored effects of lateral viscosity variations together with the effects associated with uncertainties in the radial mantle viscosity profile. The values for our choice of the asthenosphere viscosity ( $10^{21}$  Pas) and its effective thickness (500 km) in particular are poorly known.

To probe the sensitivity of our results to variations in the asthenosphere viscosity and thickness, we have computed a range of geoids from M2, the MCM with 35% CH. In doing so we left the mass distribution of the model unchanged but have assumed different viscosity profiles. Figure A.7 shows the correlation between observed and modeled geoid. The viscosity of the lithosphere and lower mantle are kept fixed in all cases ( $\eta = 10^{23}$  Pas), while the viscosity of the asthenosphere and its thickness ( $D_{AS}$  and  $\eta_{AS}$ ) are varied systematically. We find high correlation (shown in red in Figure A.7) for several configurations, all of which fall on a line representing the dependence of  $\eta_{AS}$  on  $D_{AS}^3 \cdot const.$  This is in good agreement with a recent sensitivity analysis of Post Glacial Rebound data performed by Paulson and Richards [2009] (personal communication), and suggests that our results would be left unchanged if we assumed a thinner and less viscous asthenosphere.

Our assumption of a purely thermal origin of MCM heterogeneity contrasts with geodynamic studies on mantle flow with compositional variations [e.g., Kellogg *et al.* 1999; Tackley 2000; Hansen and Yuen 2000; Montague and Kellogg 2000; Stegman *et al.* 2002; McNamara and Zhong 2004b; Farnetani and Samuel 2005] and with recent interpretations of seismic tomography arguing for substantial thermochemical components of deep mantle heterogeneity [Masters *et al.* 2000; Ishii and Tromp 1999; Trampert *et al.* 2004]. While we can certainly not preclude the existence of chemical variations in the mantle, we note, however, that a thermal interpretation of lower mantle seismic velocity anomalies is supported by recent joint inversions of seismic data, free-air gravity, dynamic topography and excess ellipticity of the CMB [Simmons *et al.* 2007], and that strong lower mantle thermal variations agree with tomographic studies showing a depthwise

increase in heterogeneity strength of low seismic velocity anomalies [*Boschi and Dziewonski 1999; Romanowicz and Gung 2002; Montelli et al. 2004*].

### A.4.3 Gravity data and the potential to distinguish between competing plate reconstructions?

In section A.3.1 we noted misfits between the observed and modeled geoid for higher spherical harmonic degrees. One intriguing reason to explain these misfits; that is, the low to negative correlation for spherical harmonic degrees  $> 3$ , must certainly be sought in the assimilated subduction history of our models. Our choice for past plate motion, as pointed out before, is the widely adopted model of *Lithgow-Bertelloni and Richards [1998]*. But alternative reconstructions, such as the recent global model of *Müller et al. [2008]*, suggest substantial differences in the implied mantle density structure and its temporal evolution. This is illustrated in Figure A.8, where we compare the models of *Lithgow-Bertelloni and Richards [1998]* and *Müller et al. [2008]* at four different points in time. The left side shows the reconstruction from *Lithgow-Bertelloni et al. [1993]* with black lines outlining the plate boundaries and arrows indicating the direction and velocity of each plate's motion. The right side shows the plate configuration from *Müller et al. [2008]* with ridges indicated in white and subduction zones in blacks. The age of the oceanic lithosphere is represented in color together with the position of the continents at each time.

A likely example of plate motion related uncertainties in the modeled geoid is our strong overestimation of the Western Pacific geoid low. While the reconstructions by *Müller et al. [2008]* suggest the presence of a mid ocean ridge — and thus the subduction of very young ocean floor under Eastern Asia as recent as 70 Ma ago — much older ocean floor is assumed to lie off-shore this region in the model *Lithgow-Bertelloni and Richards [1998]*. The older but perhaps erroneous age of subducted material implicit in the model of *Lithgow-Bertelloni and Richards [1998]* would provide a straightforward explanation of why the geoid low modeled from our MCMs is stronger in this region than observed. Equally prominent is the misfit between model and observation in the shape of the African geoid high. The likely cause for this is the substantially more southern location (about  $20^\circ$ ) of the Africa/Eurasia plate boundary and the assumed subduction polarity in the model of *Lithgow-Bertelloni and Richards [1998]* relative to the choice of *Müller et al. [2008]*. Although it is too early to comment in greater detail, further work should be directed at these intriguing differences.

## A.5 Conclusions

We have investigated the effects of strongly core heated mantle flow on the stability of Earth's rotation axis, finding that a large core heat flow of up to 12 TW

and strong hot buoyant upwelling plumes with thermal anomalies on the order of +1000–1500 K can be reconciled with the observed stability of Earth’s spin axis. The modeled TPW paths agree with the paleomagnetic data in terms of amplitude and speed, the main reason being the lower mantle viscosity increase in our models with a value of  $10^{23}$  Pa.s. Time-evolving density variations of the Earth for the past 100 Ma are predicted from mantle circulation modeling together with thermodynamic models of mantle mineralogy to map thermal into corresponding density heterogeneity, and geoids and true polar wander paths are computed using the same viscosity profile applied in the MCMs. The good correlation of the predicted depth location of downwelling slabs in our MCMs with structure imaged by tomography lends independent support for our viscosity profile. A high numerical resolution of 80 million finite elements allows us to explore vigorous mantle flow at earthlike Rayleigh number ( $10^9$ ) so that modeled thermal variations are consistent with the underlying mineralogy.

Our modeled geoids correlate well with the observed non-hydrostatic geoid at the longest wavelengths. Importantly, it is likely that intermediate wavelength misfits arise from uncertainties in the plate reconstructions, suggesting the use of gravity data to distinguish between competing plate reconstruction models.



### A.6 Figures - Chapter 3

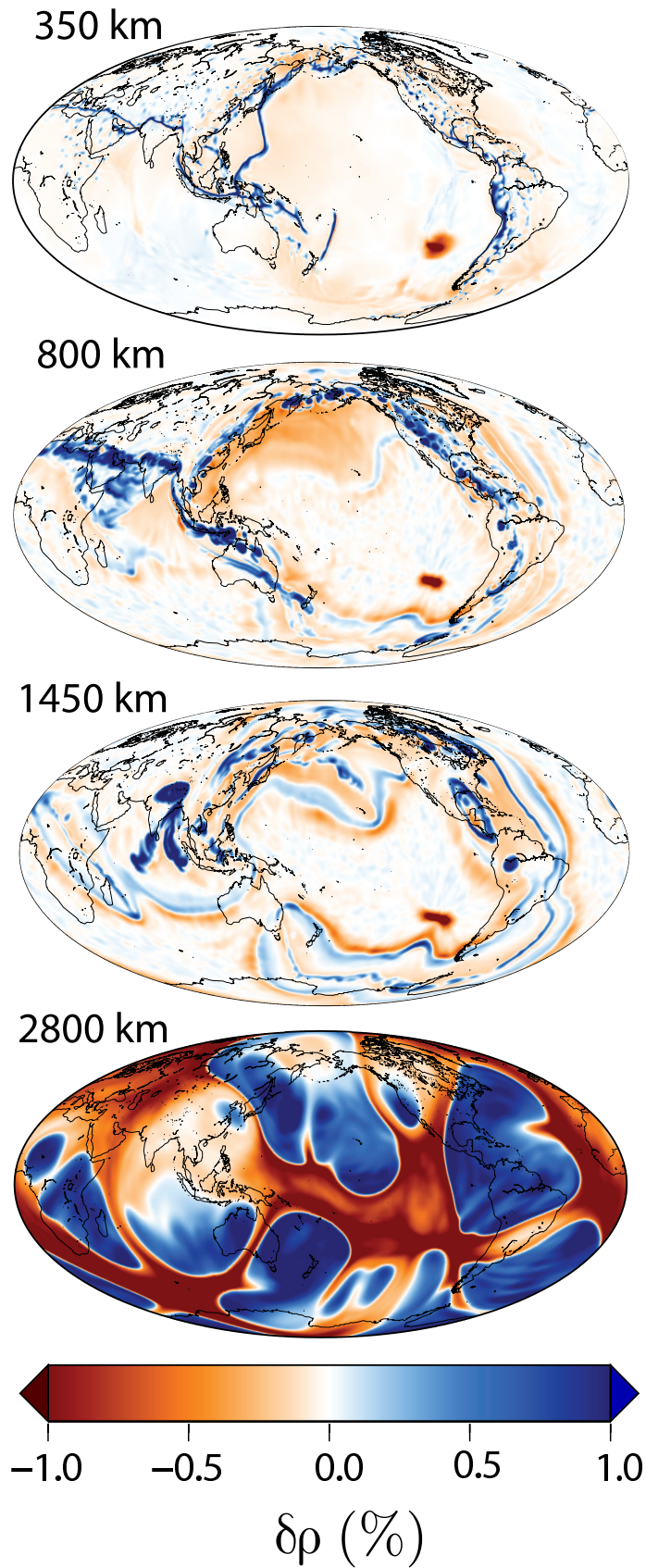




Figure A.1: Depth slices through the present day density distribution of the mantle circulation model M2 with 35% core heating (CH) corresponding to about 12 TW of core heat flux. In the upper mantle at 350 km depth, slabs located in areas of present day subduction control the density structure. At 800 km depth, the position of the prominent cold dense downwellings have changed according to the plate configuration of earlier stages of subduction, for example, all around the Pacific. Cold material associated with subduction of the Farallon plate lies east of North America's West Coast in this depth, and remnants of the Tethys ocean can be found as a distinct dense feature beneath Africa, Arabia and India. A hot low density anomaly is located in the southeast Pacific. There is little overall change in the mid mantle, at 1450 km depth, except for the location of downwellings. Here the Farallon slab lies east of North America, and remnants of subduction exist under central America. The feature with the largest thermal amplitude is a number of downwelling slabs corresponding to the collision of India and Eurasia. Cold material exists also in the North Pacific and belongs to the Kula plate which, in the reconstruction model of *Lithgow-Bertelloni and Richards* [1998], converged with North America about 50–70 Ma ago. In the lowermost mantle at 2800 km depth, hot upwellings give rise to large lateral density variations, reaching maximum values of up to  $\pm 1\%$ . A detailed analysis of the underlying thermal structure and its corresponding elastic heterogeneity showed that this model is compatible with tomography for a number of quantitative measures [*Schuberth et al.* 2009]



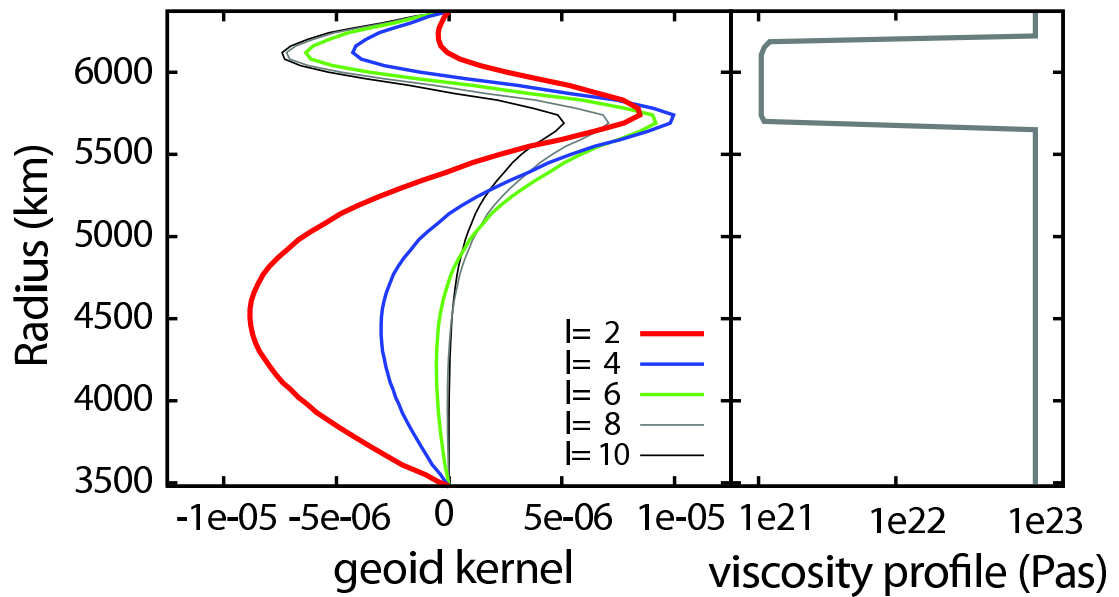
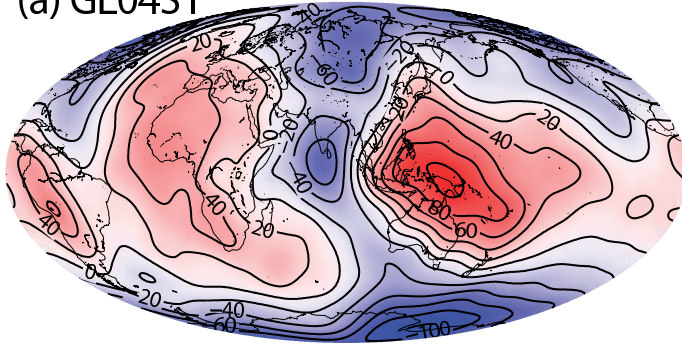


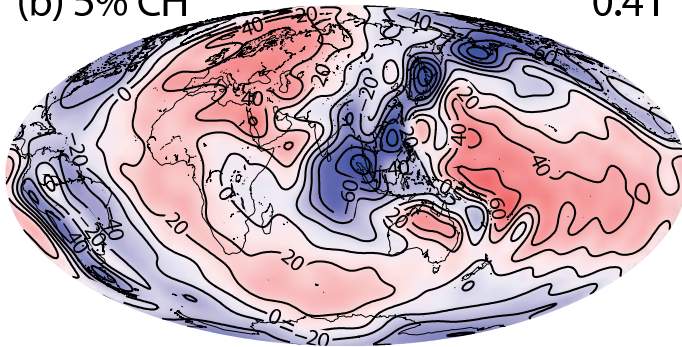
Figure A.2: Geoid kernels for different spherical harmonics degrees. The corresponding viscosity structure shown on the right is in agreement with geoid [e.g., *Hager and Richards 1989*] and post glacial rebound studies [e.g., *Mitrovica 1996*]. The kernels give the geoid anomaly at the surface for a unit probing mass anomaly: their shape and sign of the geoid kernels indicate whether the gravitational signal is dominated by the mass anomaly or by deformation of internal and external interfaces (notably the surface and the CMB). Due to isostatic compensation, all kernels tend to zero at Earth's surface and the CMB.

(a) GL04S1



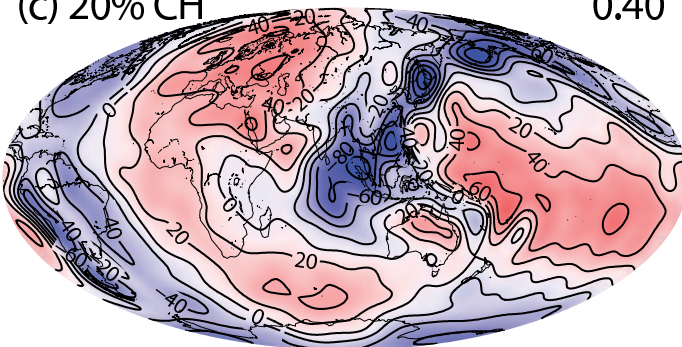
(b) 5% CH

0.41



(c) 20% CH

0.40



(d) 35% CH

0.38

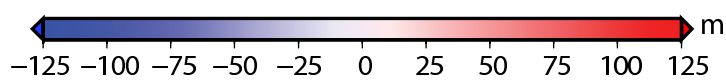
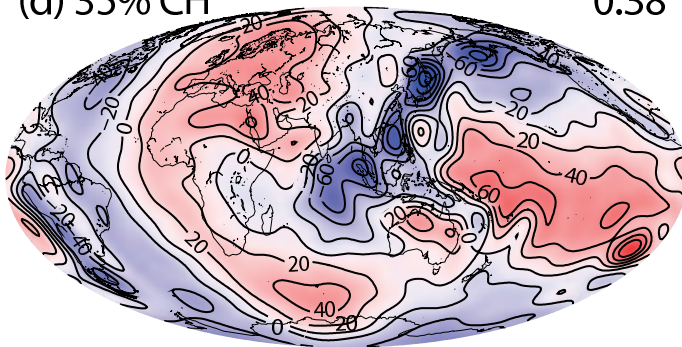


Figure A.3: a) Measured, non-hydrostatic geoid obtained from satellite-only gravity model GL04S1 [Förste *et al.* 2007; Nakiboglu 1982]. (b–d) Synthetic geoids for MCMs M1–M2 with different values of core heating (CH), which are given in percent to indicate the core contribution to the total mantle energy budget. The viscosity structure is  $\eta_{LI} = 100 \cdot 10^{21}$ ,  $\eta_{AS} = 1 \cdot 10^{21}$ ,  $\eta_{LM} = 100 \cdot 10^{21}$  as shown in Figure A.2. The correlation up to spherical harmonics degree 20 is given on the right of each modeled geoid. Generally there is good agreement between the modeled and the observed geoid in shape and amplitude (–114/77m, 5% CH; –115/77m, 20% CH; –133/99m, 40% CH; –121/107m, observed). Increasing core heating results in growing geoid highs as can be seen, for example, in the southern Indian Ocean. This is due to the additional buoyancy associated with hot upwellings. Some misfits can however be found, as for example, the overestimated geoid low in eastern Asia. As the density structure of M1–M2 is mainly controlled by the assimilated plate motion history used as boundary condition for mantle flow, it is likely that these differences arise from errors in the subduction history used.



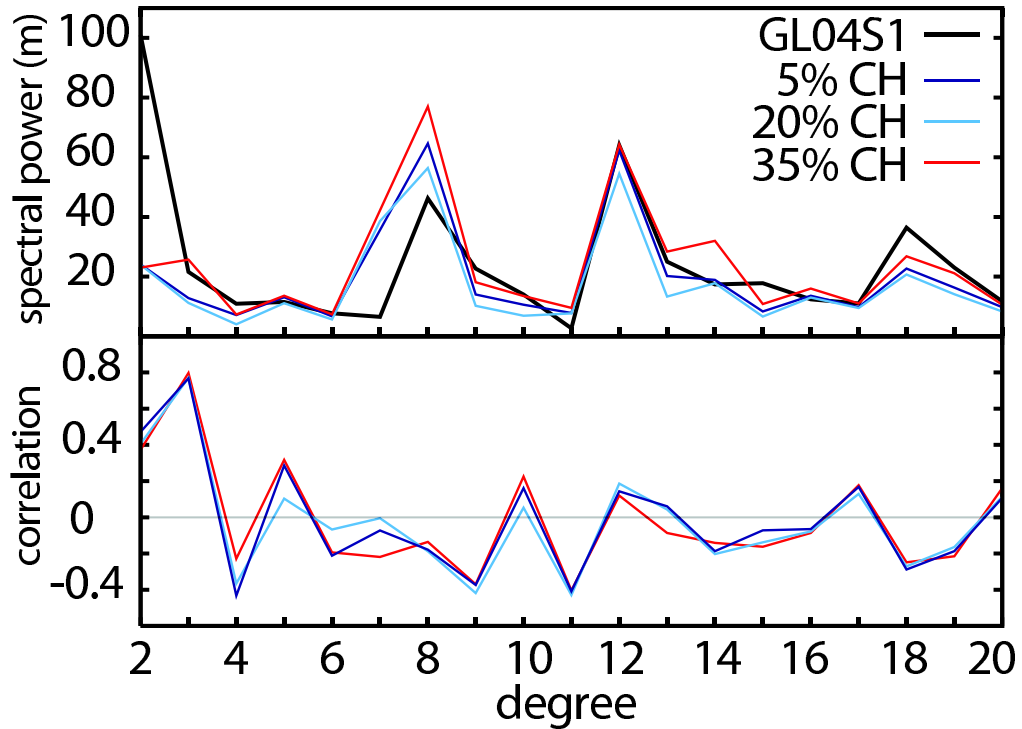


Figure A.4: Top panel: spectral amplitude of synthetic geoids from MCMs M1–M2 with different amounts of core heating (colored lines) together with the measured geoid GL04S1 (black) [Förste *et al.* 2007; Nakiboglu 1982]. Note that the amplitude of degree two does not change with more core heating. Bottom panel: correlation of our synthetic with the observed geoid as a function of spherical harmonics degree. From the high correlation of the lowest degrees, agreement in the large-scale pattern of modeled and observed geoids is evident.

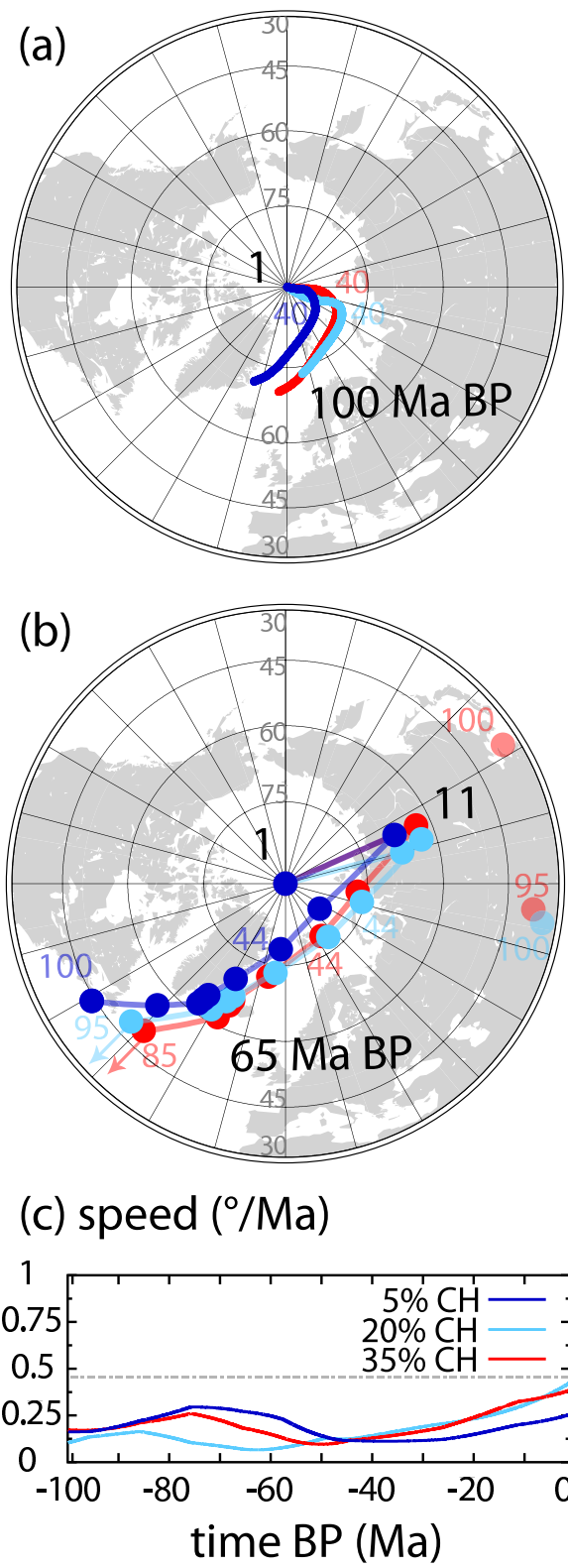




Figure A.5: (a) Synthetic true polar wander paths in the last 100 Ma computed for MCMs M1–M2 with different core heating. (b) Positional Variation of the largest principal axis of inertia in the last 100 Ma for M1–M2. Opaque circles indicate a location on the southern hemisphere. (c) Speed of true polar wander together with empirically deduced maximum speed [*Besse and Courtillot 2002*] (gray dashed line). Despite varying core heating the TPW path is similar in all models: they start at the North Pole, travel south-east up to about 40 Ma before present (BP), and then change direction by moving south-south-west until 100 Ma BP. The TPW amplitude does not exceed  $20^\circ$  in any of the models ( $19.71^\circ$  for M1,  $16.35^\circ$  for M1.5 and  $18.69^\circ$  for M2). The PIA shows little difference between the models as well and changes its direction earlier, at 20 Ma BP. The slow motion of the pole in comparison to the PIA is due to the high viscosity of the lower mantle ( $10^{23}$  Pa s) in our models, which results in small TPW speeds shown in (c). All three models are consistent with the paleomagnetic bound of  $0.45^\circ\text{Ma}^{-1}$  over the last 100 Ma.

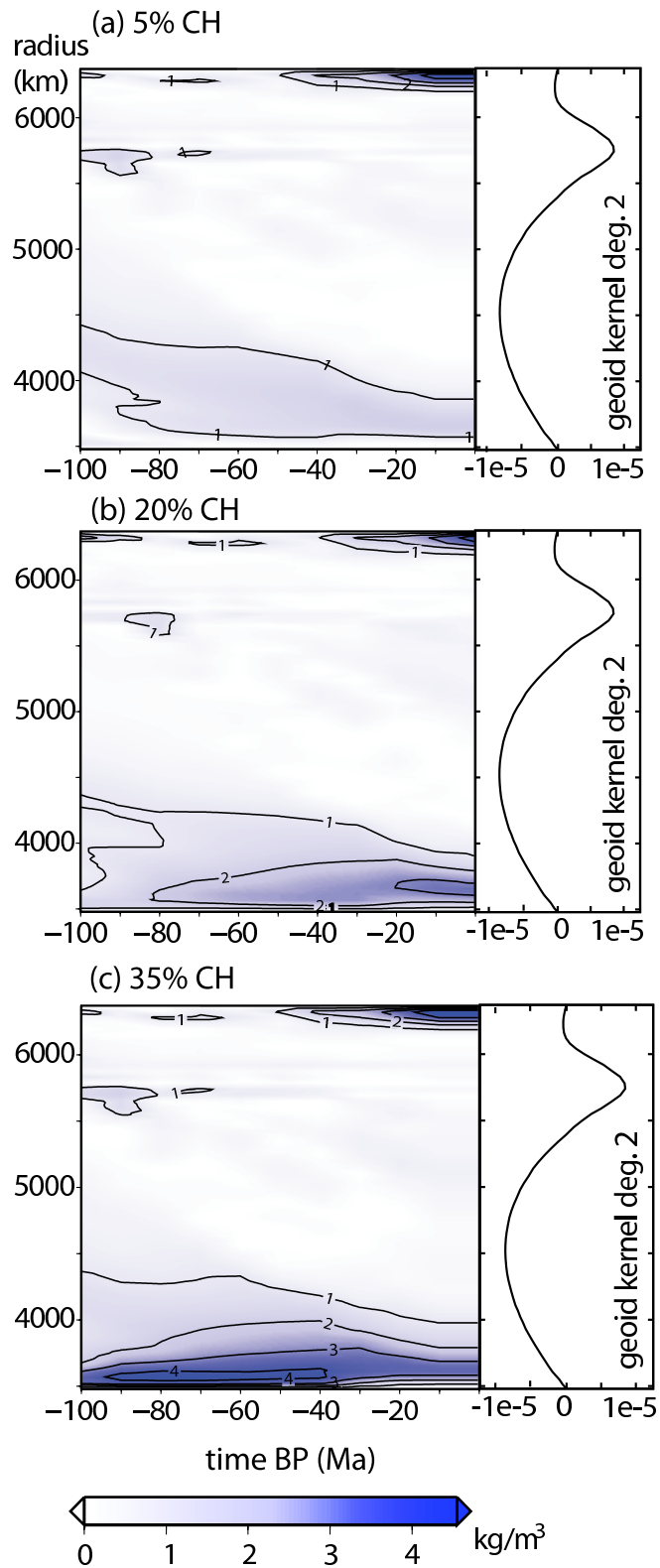


Figure A.6: Left side: Spectral amplitude of spherical harmonic degree two of the computed density structures M1–M2 at each depth and timestep backwards in time. Right side: geoid kernel of degree two. From (a) to (c) core heating increases, which mainly affects deep mantle mass anomalies (plumes) in the vicinity at the CMB. As noted in section 3 the geoid kernels act as weighting functions for the gravitational effects of density anomalies. As the kernels approach zero at the CMB, the strong amplitude of degree two heterogeneity near the CMB is ineffective in changing the spectral amplitude of the geoid (Figure A.4) and the rotational behavior (Figure A.5a) in a significant way.

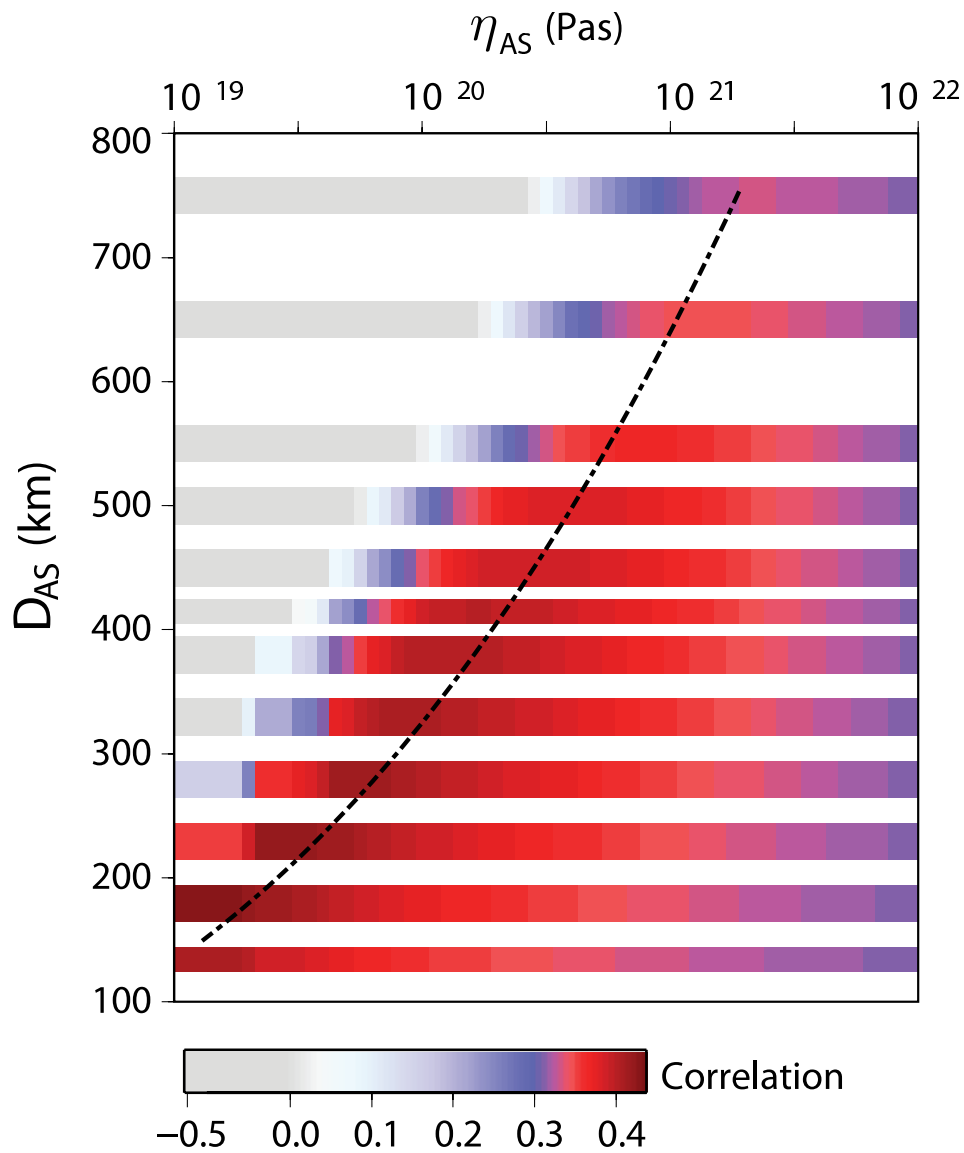


Figure A.7: Correlation of the synthetic and measured geoid for different values of the viscosity and thickness of the asthenosphere. The trade-off found here is consistent with the inferences from post-glacial rebound (black dashed line) [Paulson and Richards 2009, pers. comm.].

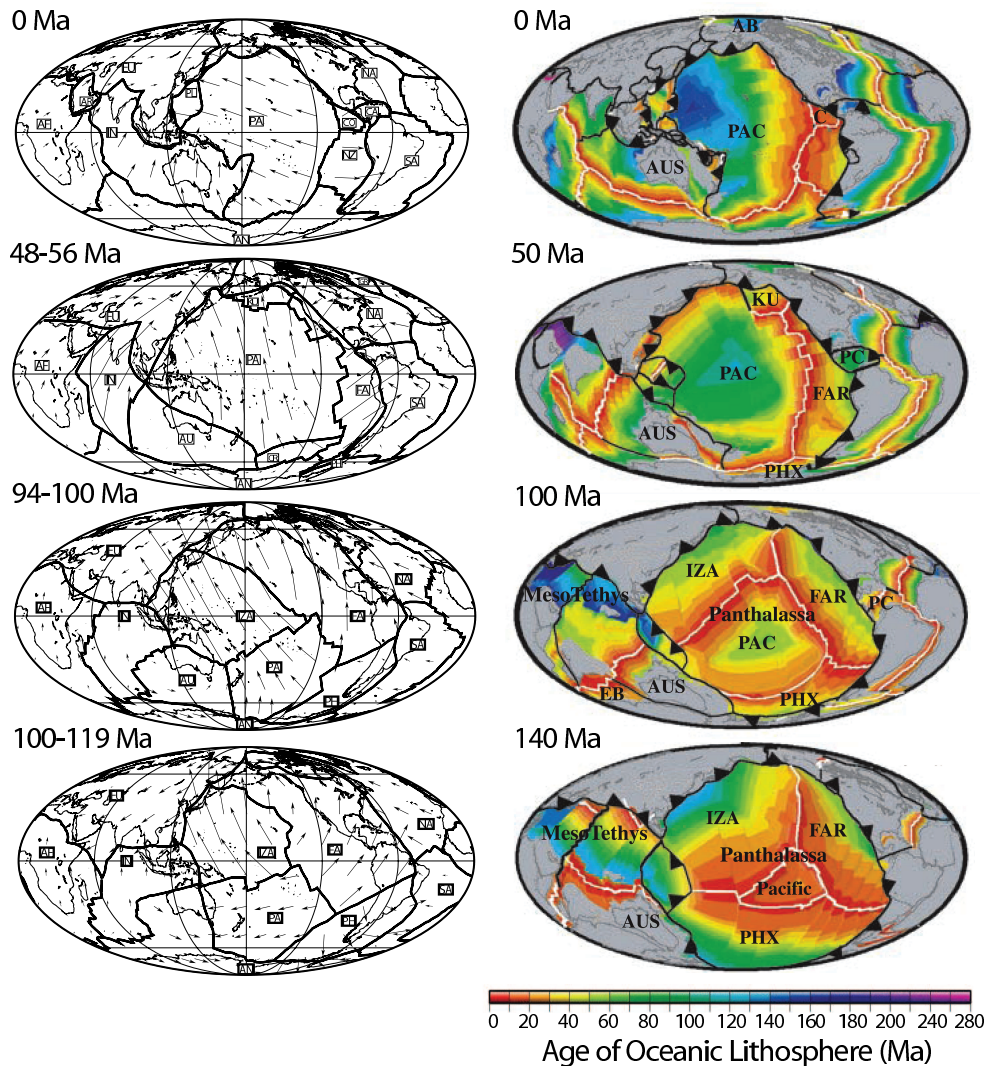


Figure A.8: Comparison of plate reconstructions. Left column: plate configurations (black lines) and velocities (arrows) from *Lithgow-Bertelloni et al. [1993]* used as boundary condition in our MCMs. Right column: recent reconstructions from *Müller et al. [2008]*. Here black and white lines indicate subduction zones and ridges, respectively, and colors illustrate the age of the oceanic lithosphere. Substantial differences between the reconstructions are visible for periods earlier than 70 Ma BP: While the reconstructions by *Müller et al. [2008]* suggest the presence of a mid oceanic ridge in the pacific at 70 Ma BP, for instance, much older ocean floor is assumed in this region in the model *Lithgow-Bertelloni and Richards [1998]*. An other example of the discrepancies is the location of the Africa/Eurasia plate boundary, which lies about  $20^\circ$  south in the model of *Lithgow-Bertelloni and Richards [1998]* relative to the choice of *Müller et al. [2008]*.

Table A.1: Variable parameters and respective values in models M1, M1.5, and M2. Viscosities in the lithosphere (LI), upper mantle (UM) and lower mantle (LM) are indexed to the reference viscosity of  $\eta_{ref} = 1 \times 10^{21}$  Pas.

Model	Viscosity structure LI/UM/LM w.r.t $\eta_{ref}$			Depth of UM/LM boundary [km]	$T_{CMB}$ [K]	CMB heat flow [TW] (% surface heat flow)	
M 1	100	1	100	660	2900	1.5	(5)
M 1.5	100	1	100	660	3500	6	(20)
M 2	100	1	100	660	4200	12	(35)

# Bibliography

- Alfè, D., G. D. Price, and M. J. Gillan (2002), Iron under Earth's core conditions: Liquid-state thermodynamics and high-pressure melting curve from ab initio calculations, *Phys. Rev. B*, *65*(16), 165,118–165,129, doi:10.1103/PhysRevB.65.165118. [13](#), [35](#), [57](#), [101](#)
- Alfè, D., M. J. Gillan, and G. D. Price (2007), Temperature and composition of the Earth's core, *Contemporary Physics*, *48*(2), 63–80, doi:10.1080/00107510701529653. [13](#), [35](#), [57](#)
- Allegre, C. J. (1982), Chemical geodynamics, *Tectonophysics*, *81*(3-4), 109–132. [11](#)
- Anderson, D. L. (1982), Hotspots, polar wander, Mesozoic convection and the geoid, *Nature*, *297*(5865), 391–393. [68](#), [97](#)
- Andraut, D., N. Bolfan-Casanova, and N. Guignot (2001), Equation of state of lower mantle (Al,Fe)-MgSiO<sub>3</sub> perovskite, *Earth Planet. Sci. Lett.*, *193*(3-4), 501–508, doi:10.1016/S0012-821X(01)00506-4. [36](#)
- Becker, T. W., and R. J. O'Connell (2001), Predicting plate velocities with mantle circulation models, *Geochem. Geophys. Geosyst.*, *2*(12), doi:10.1029/2001GC000171,2001. [12](#), [22](#), [56](#)
- Besse, J., and V. Courtillot (1991), Revised and Synthetic Apparent Polar Wander Paths of the African, Eurasian, North American and Indian Plates, and True Polar Wander Since 200 Ma, *J. Geophys. Res.*, *96*(B3), 4029–4050. [15](#), [92](#)
- Besse, J., and V. Courtillot (2002), Apparent and True Polar Wander and the geometry of the geomagnetic field in the last 200 Myrs, *J. Geophys. Res.*, *107*(B11), 2300, doi:10.1029/2000JB000050. [15](#), [92](#), [100](#), [101](#), [115](#)
- Boehler, R. (2000), High-pressure experiments and the phase diagram of lower mantle and core materials, *Rev. Geophys.*, *38*(2), 221–245. [13](#), [35](#), [57](#), [101](#)

- Boschi, L., and A. M. Dziewonski (1999), High- and low-resolution images of the Earth's mantle: Implications of different approaches to tomographic modeling, *J. Geophys. Res.*, *104*(B11), 25,567–25,594. [36](#), [103](#)
- Brodholt, J. P., G. Helffrich, and J. Trampert (2007), Chemical versus thermal heterogeneity in the lower mantle: The most likely role of anelasticity, *Earth Planet. Sci. Lett.*, *262*(3-4), 429–437, doi:10.1016/j.epsl.2007.07.054. [68](#)
- Buffett, B. A. (2002), Estimates of heat flow in the deep mantle based on the power requirements for the geodynamo, *Geophys. Res. Lett.*, *29*(12), 1566, doi:10.1029/2001GL014649. [13](#), [37](#), [57](#), [92](#)
- Bunge, H. P. (1996), Global mantle convection models, Ph.D. thesis, University of California, Berkeley. [24](#)
- Bunge, H. P. (2005), Low plume excess temperature and high core heat flux inferred from non-adiabatic geotherms in internally heated mantle circulation models, *Phys. Earth Planet. Inter.*, *153*(1-3), 3–10, doi:10.1016/j.pepi.2005.03.017. [23](#), [35](#), [67](#), [93](#)
- Bunge, H.-P., and J. Baumgardner (1995), Mantle convection modeling on parallel virtual machines, *Computers in Physics*, *9*, 207–215. [14](#), [24](#)
- Bunge, H. P., and J. H. Davies (2001), Tomographic images of a mantle circulation model, *Geophys. Res. Lett.*, *28*(1), 77–80. [15](#), [36](#), [57](#)
- Bunge, H.-P., and M. Richards (1996), The origin of large-scale structure in mantle convection: Effects of plate motions and viscosity stratification, *Geophys. Res. Lett.*, *23*, 2987–2990. [14](#), [30](#), [33](#), [59](#), [62](#), [92](#), [95](#)
- Bunge, H.-P., M. Richards, and J. Baumgardner (1996), The effect of depth-dependent viscosity on the planform of mantle convection, *Nature*, *379*, 436–438, doi:10.1038/379436a0. [14](#), [24](#), [59](#)
- Bunge, H.-P., M. Richards, and J. Baumgardner (1997), A sensitivity study of 3D-spherical mantle convection at  $10^8$  Rayleigh number: effects of depth-dependent viscosity, heating mode and an endothermic phase change, *J. Geophys. Res.*, *102*, 11,991–12,007. [14](#), [24](#), [59](#), [95](#)
- Bunge, H.-P., M. Richards, C. Lithgow-Bertelloni, J. Baumgardner, S. Grand, and B. Romanowicz (1998), Time scales and heterogeneous structure in geodynamic Earth models, *Science*, *280*, 91–95, doi:10.1126/science.280.5360.91. [12](#), [14](#), [22](#), [25](#), [56](#), [62](#), [93](#)
- Bunge, H. P., Y. Ricard, and J. Matas (2001), Non-adiabaticity in mantle convection, *Geophys. Res. Lett.*, *28*(5), 879–882. [23](#), [35](#), [93](#)



- Bunge, H.-P., M. Richards, and J. Baumgardner (2002), Mantle circulation models with sequential data-assimilation: Inferring present-day mantle structure from plate motion histories, *Phil. Trans. Roy. Soc. A*, *360*(1800), 2545–2567, doi:10.1098/rsta.2002.1080. [14](#), [15](#), [24](#), [25](#), [27](#), [37](#), [58](#), [61](#), [62](#), [93](#), [95](#)
- Bunge, H.-P., C. R. Hagelberg, and B. J. Travis (2003), Mantle circulation models with variational data-assimilation: Inferring past mantle flow and structure from plate motion histories and seismic tomography, *Geophys. J. Int.*, *2*(152), 280–301, doi:10.1046/j.1365-246X.2003.01823.x. [37](#), [38](#), [61](#)
- Cammarano, F., S. Goes, P. Vacher, and D. Giardini (2003), Inferring upper-mantle temperatures from seismic velocities, *Phys. Earth Planet. Inter.*, *138*(3–4), 197–222, doi:10.1016/S0031-9201(03)00156-0. [23](#), [32](#)
- Christensen, U. R., and A. W. Hofmann (1994), Segregation of subducted oceanic-crust in the convecting mantle, *J. Geophys. Res.*, *99*(B10), 19,867–19,884. [22](#)
- Christensen, U. R., and A. Tilgner (2004), Power requirement of the geodynamo from ohmic losses in numerical and laboratory dynamos, *Nature*, *429*(6988), 169–171, doi:10.1038/nature02508. [37](#)
- Conrad, C. P., and C. Lithgow-Bertelloni (2002), How mantle slabs drive plate tectonics, *Science*, *298*(5591), 207–209, doi:10.1126/science.1074161. [12](#), [22](#), [56](#)
- Dahlen, F. A. (2004), Resolution limit of travelttime tomography, *Geophys. J. Int.*, *157*(1), 315–331, doi:10.1111/j.1365-246X.2004.02214.x. [67](#)
- Dahlen, F. A., and J. Tromp (1998), *Theoretical Global Seismology*, Princeton University Press, Princeton, New Jersey. [29](#), [61](#)
- Davaille, A. (1999), Simultaneous generation of hotspots and superswells by convection in a heterogenous planetary mantle, *Nature*, *402*(6763), 756–760, doi:10.1038/45461. [22](#)
- Davaille, A., F. Girard, and M. Le Bars (2002), How to anchor hotspots in a convecting mantle?, *Earth Planet. Sci. Lett.*, *203*(2), 621–634, doi:10.1016/S0012-821X(02)00897-X. [23](#)
- Davies, G. F. (1988), Ocean bathymetry and mantle convection 1. Large-scale flow and hotspots, *J. Geophys. Res.*, *93*(B9), 10,467–10,480. [23](#), [37](#), [92](#)
- Davies, J. H., and H. P. Bunge (2001), Seismically "fast" geodynamic mantle models, *Geophys. Res. Lett.*, *28*(1), 73–76. [15](#), [36](#), [57](#)

- Deschamps, F., and J. Trampert (2003), Mantle tomography and its relation to temperature and composition, *Phys. Earth Planet. Inter.*, *140*(4), 277–291, doi:10.1016/j.pepi.2003.09.004. [12](#), [22](#)
- Deschamps, F., and J. Trampert (2004), Towards a lower mantle reference temperature and composition, *Earth Planet. Sci. Lett.*, *222*(1), 161–175, doi:10.1016/j.epsl.2004.02.024. [13](#), [23](#)
- Dumbser, M., and M. Käser (2006), An arbitrary high-order discontinuous Galerkin method for elastic waves on unstructured meshes-II. The three-dimensional isotropic case, *Geophys. J. Int.*, *167*(1), 319–336, doi:10.1111/j.1365-246X.2006.03120.x. [87](#)
- Dziewonski, A. M., and D. L. Anderson (1981), Preliminary reference Earth model, *Phys. Earth Planet. Inter.*, *25*, 297–356, doi:10.1016/0031-9201(81)90046-7. [11](#), [28](#), [99](#)
- Dziewonski, A. M., B. H. Hager, and R. J. O’Connell (1977), Large-Scale Heterogeneities in the Lower Mantle, *J. Geophys. Res.*, *82*(2), 239–255. [12](#), [56](#)
- Farnetani, C. G., and H. Samuel (2005), Beyond the thermal plume paradigm, *Geophys. Res. Lett.*, *32*(7), L07,311, doi:10.1029/2005GL022360. [23](#), [56](#), [102](#)
- Fichtner, A., H.-P. Bunge, and H. Igel (2006a), The adjoint method in seismology: I - Theory, *Phys. Earth Planet. Inter.*, *157*(1-2), 86–104, doi:10.1016/j.pepi.2006.03.016. [39](#)
- Fichtner, A., P. Bunge, and H. Igel (2006b), The adjoint method in seismology: II - Applications: traveltimes and sensitivity functionals, *Phys. Earth Planet. Inter.*, *157*(1-2), 105–123, doi:10.1016/j.pepi.2006.03.018. [39](#)
- Förste, C., et al. (2007), The GeoForschungsZentrum Potsdam/Groupe de Recherche de Geodesie Spatiale satellite-only and combined gravity field models: EIGEN-GL04S1 and EIGEN-GL04C, *Journal of Geodesy*. [97](#), [111](#), [113](#)
- Fukao, Y., S. Widiyantoro, and M. Obayashi (2001), Stagnant slabs in the upper and lower mantle transition region, *Rev. Geophys.*, *39*(3), 291–323. [12](#)
- Garnero, E. J. (2000), Heterogeneity of the lowermost mantle, *Annual Review of Earth and Planetary Sciences*, *33*, 1–66, doi:10.1146/annurev.earth.28.1.509. [36](#)
- Gilbert, F., and A. Dziewonski (1975), An application of normal mode theory to the retrieval of structural parameters and source mechanisms for seismic spectra, *Phil. Trans. R. Soc. Lond., Ser. A* *278*, 187–269. [11](#)

- Glatzmaier, G. A. (1988), Numerical simulations of mantle convection - time-dependent, 3-dimensional, compressible, spherical-shell, *Geophysical And Astrophysical Fluid Dynamics*, *43*(2), 223–264, doi:10.1080/03091928808213626. [24](#)
- Glatzmaier, G. A., and P. H. Roberts (1995), A 3-dimensional self-consistent computer-simulation of a geomagnetic-field reversal, *Nature*, *377*(6546), 203–209, doi:10.1038/377203a0. [13](#), [37](#), [57](#), [92](#)
- Goes, S., F. Cammarano, and U. Hansen (2004), Synthetic seismic signature of thermal mantle plumes, *Earth Planet. Sci. Lett.*, *218*(3-4), 403–419, doi:10.1016/S0012-821X(03)00680-0. [32](#)
- Gordon, R. G., and D. M. Jurdy (1986), Cenozoic global plate motions, *J. Geophys. Res.*, *91*(B12), 2389–2406. [94](#)
- Grand, S., R. van der Hilst, and S. Widiyantoro (1997), Global seismic tomography: A snapshot of mantle convection in the Earth, *GSA Today*, *7*, 1–7. [12](#), [22](#), [56](#)
- Greff-Lefftz, M. (2004), Upwelling plumes, superswells and true polar wander, *Geophys. J. Int.*, *159*(3), 1125–1137, doi:10.1111/j.1365-246X.2004.02440.x. [99](#), [101](#)
- Gubbins, D., D. Alfe, G. Masters, G. D. Price, and M. J. Gillan (2003), Can the Earth's dynamo run on heat alone?, *Geophys. J. Int.*, *155*(2), 609–622, doi:10.1046/j.1365-246X.2003.02064.x. [37](#)
- Gubbins, D., D. Alfe, G. Masters, G. D. Price, and M. Gillan (2004), Gross thermodynamics of two-component core convection, *Geophys. J. Int.*, *157*(3), 1407–1414, doi:10.1111/j.1365-246X.2004.02219.x. [13](#), [37](#), [57](#)
- Hager, B. H. (1984), Subducted slabs and the geoid: Constraints on mantle rheology and flow, *J. Geophys. Res.*, *89*, 6003–6015, doi:10.1029/JB089iB07p06003. [97](#), [98](#)
- Hager, B. H., and M. A. Richards (1989), Long-wavelength variations in Earths geoid - Physical models and dynamical implications, *Phil. Trans. Roy. Soc. A*, *328*(1599), 309–327, doi:10.1098/rsta.1989.0038. [26](#), [93](#), [95](#), [109](#)
- Hall, R. (2002), Cenozoic geological and plate tectonic evolution of SE Asia and the SW Pacific: Computer-based reconstructions, model and animations, *Journal Of Asian Earth Sciences*, *20*(4), 353–431. [94](#)
- Hansen, U., and D. A. Yuen (1989), Dynamical influences from thermal-chemical instabilities at the core-mantle boundary, *Geophys. Res. Lett.*, *16*(7), 629–632. [23](#)

- Hansen, U., and D. A. Yuen (1994), Effects of depth-dependent thermal expansivity on the interaction of thermal-chemical plumes with a compositional boundary, *Phys. Earth Planet. Inter.*, *86*(1-3), 205–221, doi:10.1016/0031-9201(94)05069-4. [23](#)
- Hansen, U., and D. A. Yuen (2000), Extended-Boussinesq thermal-chemical convection with moving heat sources and variable viscosity, *Earth Planet. Sci. Lett.*, *176*(3-4), 401–411, doi:10.1016/S0012-821X(00)00009-1. [23](#), [102](#)
- Hernlund, J. W., and C. Houser (2008), On the statistical distribution of seismic velocities in Earth’s deep mantle, *Earth Planet. Sci. Lett.*, *265*(3-4), 423–437, doi:10.1016/j.epsl.2007.10.042. [39](#), [69](#)
- Houser, C., G. Masters, P. Shearer, and G. Laske (2008), Shear and compressional velocity models of the mantle from cluster analysis of long-period waveforms, *Geophys. J. Int.*, *174*(1), 195–212, doi:10.1111/j.1365-246X.2008.03763.x. [12](#), [41](#), [50](#), [51](#), [52](#), [56](#), [57](#), [59](#)
- Hutko, A. R., T. Lay, J. Revenaugh, and E. J. Garnero (2008), Anticorrelated seismic velocity anomalies from post-perovskite in the lowermost mantle, *Science*, *320*(5879), 1070–1074, doi:10.1126/science.1155822. [39](#), [69](#)
- Iaffaldano, G., and H.-P. Bunge (2008), Strong plate coupling along the Nazca–South America convergent margin, *Geology*, *36*(6), 443–446, doi:10.1130/G24489A.1. [38](#)
- Iaffaldano, G., H.-P. Bunge, and T. H. Dixon (2006), Feedback between mountain belt growth and plate convergence, *Geology*, *34*(10), 893–896, doi:10.1130/G22661.1. [38](#)
- Irifune, T. (1987), An experimental investigation of the pyroxene garnet transformation in a pyrolite composition and its bearing on the constitution of the mantle, *Phys. Earth Planet. Inter.*, *45*(4), 324–336, doi:10.1016/0031-9201(87)90040-9. [17](#), [23](#), [94](#)
- Ishii, M., and J. Tromp (1999), Normal-Mode and Free-Air Gravity Constraints on Lateral Variations in Velocity and Density of Earth’s Mantle, *Science*, *285*(5431), 1231–1236, doi:10.1126/science.285.5431.1231. [13](#), [22](#), [36](#), [102](#)
- Ishii, M., and J. Tromp (2001), Even-degree lateral variations in the Earth’s mantle constrained by free oscillations and the free-air gravity anomaly, *Geophys. J. Int.*, *145*(1), 77–96, doi:10.1111/j.1365-246X.2001.00385.x. [13](#), [22](#), [52](#), [56](#)
- Ismail-Zadeh, A., G. Schubert, I. Tsepelev, and A. Korotkii (2004), Inverse problem of thermal convection: numerical approach and application to mantle plume restoration, *Phys. Earth Planet. Inter.*, *145*(1-4), 99–114, doi:10.1016/j.pepi.2004.03.006. [38](#)

- Ismail-Zadeh, A., A. Korotkii, G. Schubert, and I. Tsepelev (2007), Quasi-reversibility method for data assimilation in models of mantle dynamics, *Geophys. J. Int.*, *170*(3), 1381–1398, doi:10.1111/j.1365-246X.2007.03496.x. [38](#)
- Jackson, I. (Ed.) (1998a), *The Earth's Mantle*, Cambridge University Press, — Sig.: Bf161. [13](#), [68](#)
- Jackson, I. (1998b), Elasticity, composition and temperature of the earth's lower mantle: a reappraisal, *Geophys. J. Int.*, *134*(1), 291–311, doi:10.1046/j.1365-246x.1998.00560.x. [36](#)
- Jarvis, G. T., and D. P. McKenzie (1980), Convection in a compressible fluid with infinite Prandtl number, *Journal Of Fluid Mechanics*, *96*(FEB), 515–583, doi:10.1017/S002211208000225X. [24](#)
- Jeanloz, R., and S. Morris (1987), Is the mantle geotherm subadiabatic, *Geophys. Res. Lett.*, *14*(4), 335–338. [23](#), [35](#), [93](#)
- Jellinek, A. M., and M. Manga (2004), Links between long-lived hot spots, mantle plumes, D", and plate tectonics, *Rev. Geophys.*, *42*, RG3002, doi:10.1029/2003RG000144. [23](#), [37](#)
- Jochum, K. P., A. W. Hofmann, E. Ito, H. M. Seufert, and W. M. White (1983), K, U and Th in mid-ocean ridge basalt glasses and heat-production, K/U and K/Rb in the mantle, *Nature*, *306*(5942), 431–436, doi:10.1038/306431a0. [37](#)
- Jordan, T. H., P. Puster, G. A. Glatzmaier, and P. J. Tackley (1993), Comparisons between seismic Earth structures and mantle flow models based on radial correlation-functions, *Science*, *261*(5127), 1427–1431, doi:10.1126/science.261.5127.1427. [29](#), [61](#)
- Kárason, H., and R. D. van der Hilst (2001), Tomographic imaging of the lowermost mantle with differential times of refracted and diffracted core phases (PKP, Pdiff), *J. Geophys. Res.*, *106*, 6569–6588. [52](#)
- Käser, M., and M. Dumbser (2006), An arbitrary high-order discontinuous Galerkin method for elastic waves on unstructured meshes-I. The two-dimensional isotropic case with external source terms, *Geophys. J. Int.*, *166*(2), 855–877, doi:10.1111/j.1365-246X.2006.03051.x. [87](#)
- Kellogg, L. H., B. H. Hager, and R. D. van der Hilst (1999), Compositional stratification in the deep mantle, *Science*, *283*(5409), 1881–1884, doi:10.1126/science.283.5409.1881. [22](#), [37](#), [92](#), [102](#)
- Kennett, B. L. N., and E. R. Engdahl (1991), Traveltimes for global earthquake location and phase identification, *Geophys. J. Int.*, *105*, 429–465, doi:10.1111/j.1365-246X.1991.tb06724.x. [11](#)

- Kennett, B. L. N., E. R. Engdahl, and R. Buland (1995), Constraints on seismic velocities in the earth from travel-times, *Geophys. J. Int.*, *122*(1), 108–124, doi:10.1111/j.1365-246X.1995.tb03540.x. [11](#), [28](#)
- Kennett, B. L. N., S. Widiyantoro, and R. D. van der Hilst (1998), Joint seismic tomography for bulk sound and shear wave speed in the Earth’s mantle, *J. Geophys. Res.*, *103*(B6), 12,469–12,493. [12](#), [13](#), [22](#), [56](#)
- Khan, A., J. A. D. Connolly, and S. R. Taylor (2008), Inversion of seismic and geodetic data for the major element chemistry and temperature of the earth’s mantle, *J. Geophys. Res.*, *113*, B09,308, doi:10.1029/2007JB005239. [13](#)
- Kiefer, B., L. Stixrude, and R. M. Wentzcovitch (2002), Elasticity of (Mg,Fe)SiO<sub>3</sub>-perovskite at high pressures, *Geophys. Res. Lett.*, *29*(11), 1539, doi:doi:10.1029/2002GL014683. [36](#)
- Komatitsch, D., and J. Tromp (1999), Introduction to the spectral-element method for 3-D seismic wave propagation, *Geophys. J. Int.*, *139*, 806–822. [87](#)
- Komatitsch, D., and J. Tromp (2002a), Spectral-element simulations of global seismic wave propagation-I. Validation, *Geophys. J. Int.*, *149*, 390–412. [87](#)
- Komatitsch, D., and J. Tromp (2002b), Spectral-element simulations of global seismic wave propagation - ii. three-dimensional models, oceans, rotation and self-gravitation, *Geophys. J. Int.*, *150*(1), 303–318. [87](#)
- Kuang, W. L., and J. Bloxham (1997), An earth-like numerical dynamo model, *Nature*, *389*(6649), 371–374, doi:10.1038/38712. [13](#), [37](#), [57](#), [92](#)
- Kustowski, B., G. Ekstrom, and A. M. Dziewonski (2008), Anisotropic shear-wave velocity structure of the Earth’s mantle: A global model, *J. Geophys. Res.*, *113*(B6), B06,306. [12](#), [56](#)
- Labrosse, S. (2003), Thermal and magnetic evolution of the earth’s core, *Phys. Earth Planet. Inter.*, *140*(1-3), 127–143, doi:10.1016/j.pepi.2003.07.006. [37](#)
- Lambeck, K. (1988), *Geophysical Geodesy — The Slow Deformations of the Earth*, Clarendon Press, Oxford. [97](#)
- Lay, T. (2008), Sharpness of the D” discontinuity beneath the Cocos Plate: Implications for the perovskite to post-perovskite phase transition, *Geophys. Res. Lett.*, *35*, L03,304, doi:10.1029/2007GL032465. [23](#)
- Lay, T., J. Hernlund, and B. A. Buffett (2008), Core-mantle boundary heat flow, *Nature Geoscience*, *1*(1), 25–32, doi:10.1038/ngeo.2007.44. [93](#)

- Leng, W., and S. J. Zhong (2008), Controls on plume heat flux and plume excess temperature, *J. Geophys. Res.*, *113*(B4), B04,408, doi:10.1029/2007JB005155. [93](#)
- Li, X. D., and B. Romanowicz (1995), Comparison of global wave-form inversions with and without considering cross-branch modal coupling, *Geophys. J. Int.*, *121*(3), 695–709. [57](#)
- Li, X. D., and B. Romanowicz (1996), Global mantle shear velocity model developed using nonlinear asymptotic coupling theory, *J. Geophys. Res.*, *101*(B10), 22,245–22,272. [12](#), [22](#), [56](#)
- Lin, J. F., S. D. Jacobsen, W. Sturhahn, J. M. Jackson, J. Y. Zhao, and C. S. Yoo (2006), Sound velocities of ferropericlase in the Earth’s lower mantle, *Geophys. Res. Lett.*, *33*(22), L22,304, doi:10.1029/2006GL028099. [36](#)
- Lithgow-Bertelloni, C., and M. A. Richards (1998), The dynamics of Cenozoic and Mesozoic plate motions, *Rev. Geophys.*, *36*(1), 27–78. [12](#), [22](#), [25](#), [38](#), [56](#), [94](#), [95](#), [103](#), [107](#), [119](#)
- Lithgow-Bertelloni, C., M. A. Richards, Y. Ricard, R. J. O’Connell, and D. C. Engebretson (1993), Toroidal-poloidal partitioning of plate motions since 120 ma, *Geophys. Res. Lett.*, *20*(5), 375–378. [4](#), [103](#), [119](#)
- Liu, L. J., and M. Gurnis (2008), Simultaneous inversion of mantle properties and initial conditions using an adjoint of mantle convection, *J. Geophys. Res.*, *113*(B8), B08,405, doi:10.1029/2008JB005594. [38](#)
- Mao, H. K., R. J. Hemley, Y. Fei, J. F. Shu, L. C. Chen, A. P. Jephcoat, Y. Wu, and W. A. Bassett (1991), Effect of pressure, temperature, and composition on lattice-parameters and density of (Fe,Mg)SiO<sub>3</sub>-perovskites to 30 gpa, *J. Geophys. Res.*, *96*(B5), 8069–8079. [36](#)
- Marton, F. C., and R. E. Cohen (2002), Constraints on lower mantle composition from molecular dynamics simulations of mgsio<sub>3</sub> perovskite, *Phys. Earth Planet. Inter.*, *134*(3-4), 239–252. [13](#)
- Masters, G., S. Johnson, G. Laske, H. Bolton, and J. H. Davies (1996), A shear-velocity model of the mantle, *Phil. Trans. Roy. Soc. A*, *354*(1711), 1385–1410, doi:10.1098/rsta.1996.0054. [22](#)
- Masters, G., G. Laske, H. Bolton, and A. M. Dziewonski (2000), *Earth’s Deep Interior – Mineral Physics and Tomography From the Atomic to the Global Scale*, chap. The Relative Behavior of Shear Velocity, Bulk Sound Speed, and Compressional Velocity in the Mantle: Implications for Chemical and Thermal Structure, pp. 63–87, American Geophysical Union, Washington D.C. [12](#), [13](#), [22](#), [36](#), [52](#), [56](#), [102](#)

- Matas, J., J. Bass, Y. Ricard, E. Mattern, and M. S. T. Bukowinski (2007), On the bulk composition of the lower mantle: predictions and limitations from generalized inversion of radial seismic profiles, *Geophys. J. Int.*, *170*, 764–780, doi:10.1111/j.1365-246X.2007.03454.x. [13](#), [23](#)
- Mattern, E., J. Matas, Y. Ricard, and J. Bass (2005), Lower mantle composition and temperature from mineral physics and thermodynamic modelling, *Geophys. J. Int.*, *160*(3), 973–990, doi:10.1111/j.1365-246X.2004.02549.x. [13](#), [23](#), [35](#)
- Matyska, C., and D. A. Yuen (2000), Profiles of the Bullen parameter from mantle convection modelling, *Earth Planet. Sci. Lett.*, *178*(1-2), 39–46, doi:10.1016/S0012-821X(00)00060-1. [23](#), [35](#)
- McDonough, W. F. (2007), Mapping the earth’s engine, *Science*, *317*(5842), 1177–1178, doi:10.1126/science.1144405. [37](#)
- McKenzie, D., and M. J. Bickle (1988), The volume and composition of melt generated by extension of the lithosphere, *J. Petrology*, *29*(3), 625–679. [27](#)
- McKenzie, D., and F. M. Richter (1981), Parameterized thermal-convection in a layered region and the thermal history of the earth, *J. Geophys. Res.*, *86*(NB12), 1667–1680. [11](#)
- McNamara, A., and S. Zhong (2005), Thermochemical structures beneath Africa and the Pacific Ocean, *Nature*, *437*, 1136–1139, doi:10.1038/nature04066. [14](#), [23](#), [37](#), [61](#), [93](#)
- McNamara, A. K., and S. J. Zhong (2004a), The influence of thermochemical convection on the fixity of mantle plumes, *Earth Planet. Sci. Lett.*, *222*(2), 485–500, doi:10.1016/j.epsl.2004.03.008. [58](#)
- McNamara, A. K., and S. J. Zhong (2004b), Thermochemical structures within a spherical mantle: Superplumes or piles?, *J. Geophys. Res.*, *109*(B7), B07,402, doi:10.1029/2003JB002847. [23](#), [37](#), [102](#)
- McNamara, A. K., P. E. van Keken, and S. I. Karato (2002), Development of anisotropic structure in the Earth’s lower mantle by solid-state convection, *Nature*, *416*(6878), 310–314, doi:10.1038/416310a. [12](#), [22](#), [56](#)
- Mégnin, C., H.-P. Bunge, B. Romanowicz, and M. Richards (1997), Imaging 3-D spherical convection models: What can seismic tomography tell us about mantle dynamics?, *Geophys. Res. Lett.*, *24*(11), 1299–1302, doi:10.1029/97GL01256. [15](#), [36](#), [57](#), [67](#)
- Mitrovica, J. X. (1996), Haskell [1935] revisited, *J. Geophys. Res.*, *101*(B1), 555–569. [26](#), [94](#), [95](#), [109](#)



- Mitrovica, J. X., J. Wahr, I. Matsuyama, and A. Paulson (2005), The rotational stability of an ice-age Earth, *Geophys. J. Int.*, *161*, 491–506, doi:10.1111/j.1365-246X.2005.02609.x. [101](#)
- Mittelstaedt, E., and P. J. Tackley (2006), Plume heat flow is much lower than CMB heat flow, *Earth Planet. Sci. Lett.*, *241*(1-2), 202–210, doi:10.1016/j.epsl.2005.10.012. [23](#), [93](#)
- Monnereau, M., and D. A. Yuen (2002), How flat is the lower-mantle temperature gradient?, *Earth Planet. Sci. Lett.*, *202*(1), 171–183, doi:10.1016/S0012-821X(02)00756-2. [23](#), [35](#), [93](#)
- Montague, N. L., and L. H. Kellogg (2000), Numerical models of a dense layer at the base of the mantle and implications for the geodynamics of D", *J. Geophys. Res.*, *105*(B5), 11,101–11,114. [23](#), [102](#)
- Montelli, R., G. Nolet, F. A. Dahlen, G. Masters, E. R. Engdahl, and S.-H. Hung (2004), Finite-Frequency Tomography Reveals a Variety of Plumes in the Mantle, *Science*, *303*(5656), 338–343, doi:10.1126/science.1092485. [12](#), [22](#), [36](#), [93](#), [103](#)
- Montelli, R., G. Nolet, F. A. Dahlen, and G. Masters (2006), A catalogue of deep mantle plumes: New results from finite-frequency tomography, *Geochem. Geophys. Geosyst.*, *7*, Q11,007, doi:10.1029/2006GC001248. [12](#), [22](#), [32](#), [41](#), [50](#), [51](#), [52](#), [56](#), [57](#), [59](#)
- Müller, R., M. Sdrolias, C. Gaina, and W. Roest (2008), Age, spreading rates and spreading asymmetry of the world's ocean crust, *Geochem. Geophys. Geosyst.*, *9*(4), doi:10.1029/2007GC001743. [4](#), [37](#), [94](#), [103](#), [119](#)
- Munk, W. H., and G. J. F. McDonald (1960), *The Rotation of the Earth*, Cambridge University Press. [99](#)
- Murnaghan, F. (1951), *Finite Deformation of an Elastic Solid*, Wiley, New York. [25](#)
- Nakagawa, T., and P. J. Tackley (2004), Thermo-chemical structure in the mantle arising from a three-component convective system and implications for geochemistry, *Phys. Earth Planet. Inter.*, *146*(1-2), 125–138, doi:10.1016/j.pepi.2003.05.006. [23](#)
- Nakiboglu, S. M. (1982), Hydrostatic theory of the Earth and its mechanical implications, *Phys. Earth Planet. Inter.*, *28*, 302–311, doi:10.1016/0031-9201(82)90087-5. [97](#), [111](#), [113](#)

- Ni, S., and D. V. Helmberger (2003), Further constraints on the african superplume structure, *Phys. Earth Planet. Inter.*, *140*(1-3), 243–251, doi:10.1016/j.pepi.2003.07.011. [12](#), [22](#)
- Ni, S. D., E. Tan, M. Gurnis, and D. V. Helmberger (2002), Sharp sides to the African superplume, *Science*, *296*, 1850–1852, doi:10.1126/science.1070698. [12](#), [22](#), [37](#), [56](#), [58](#), [68](#), [70](#)
- Nimmo, F., G. D. Price, J. Brodholt, and D. Gubbins (2004), The influence of potassium on core and geodynamo evolution, *Geophys. J. Int.*, *156*(2), 363–376, doi:10.1111/j.1365-246X.2003.02157.x. [13](#), [37](#), [57](#), [92](#)
- Nolet, G., S. I. Karato, and R. Montelli (2006), Plume fluxes from seismic tomography, *Earth Planet. Sci. Lett.*, *248*, 685–699, doi:10.1016/j.epsl.2006.06.011. [12](#), [13](#), [37](#), [57](#), [101](#)
- Oeser, J., H. P. Bunge, and M. Mohr (2006), Cluster design in the Earth Sciences - Tethys, *High Performance Computing And Communications, Proceedings, 4208*, 31–40. [24](#), [93](#)
- Panasjuk, S. V., B. H. Hager, and A. M. Forte (1996), Understanding the effects of mantle compressibility on geoid kernels, *Geophys. J. Int.*, *124*(1), 121–133, doi:10.1111/j.1365-246X.1996.tb06357.x. [96](#)
- Panning, M., and B. Romanowicz (2006), A three dimensional radially anisotropic model of shear velocity in the whole mantle, *Geophys. J. Int.*, *167*, 361–379. [12](#), [56](#)
- Paulson, A., and M. Richards (2009), On the resolution of radial viscosity structure in modeling long-wavelength post-glacial rebound data, *Geophys. J. Int.*, *subm.* [102](#), [118](#)
- Paulson, A., S. J. Zhong, and J. Wahr (2007), Inference of mantle viscosity from GRACE and relative sea level data, *Geophys. J. Int.*, *171*(2), 497–508, doi:10.1111/j.1365-246X.2007.03556.x. [26](#)
- Phillips, B. R., and H.-P. Bunge (2005), Heterogeneity and time dependence in 3D spherical mantle convection models with continental drift, *Earth Planet. Sci. Lett.*, *233*(1-2), 121–135, doi:10.1016/j.epsl.2005.01.041. [68](#)
- Piazzoni, A. S., G. Steinle-Neumann, H.-P. Bunge, and D. Dolejš (2007), A mineralogical model for density and elasticity of the Earth’s mantle, *Geochem. Geophys. Geosyst.*, *8*, doi:10.1029/2007GC001697. [16](#), [18](#), [24](#), [34](#), [35](#), [45](#), [56](#), [67](#), [93](#), [95](#)
- Presnall, D. C., and G. H. Gudfinnsson (2008), Origin of the oceanic lithosphere, *Journal Of Petrology*, *49*(4), 615–632, doi:10.1093/petrology/egm052. [27](#)

- Quere, S., D. Rowley, A. Forte, and R. Moucha (2007), No-Net-Rotation and Indo-Atlantic hotspot reference frames: Towards a new view of tectonic plate motions and Earth dynamics, *Eos Trans. AGU*, *88*(52), Abstract U34A-03, fall Meet. Suppl. [94](#)
- Resovsky, J., and J. Trampert (2003), Using probabilistic seismic tomography to test mantle velocity-density relationships, *Earth Planet. Sci. Lett.*, *215*(1-2), 121–134, doi:10.1016/S0012-821X(03)00436-9. [13](#), [22](#)
- Ricard, Y., L. Fleitout, and C. Froidevaux (1984), Geoid heights and lithospheric stresses for a dynamic Earth, *Annales Geophysicae*, *2*, 267–285. [96](#)
- Ricard, Y., R. Sabadini, and G. Spada (1992), Isostatic deformations and polar wander induced by redistribution of mass within the Earth, *J. Geophys. Res.*, *97*, 14,223–14,236. [99](#), [101](#)
- Ricard, Y., M. Richards, C. Lithgow-Bertelloni, and Y. LeStunff (1993a), A geodynamic model of mantle density heterogeneity, *J. Geophys. Res.*, *98*(B12), 21,895–21,909. [93](#), [97](#), [98](#), [101](#), [102](#)
- Ricard, Y., G. Spada, and R. Sabadini (1993b), Polar wandering of a dynamic Earth, *Geophys. J. Int.*, *113*(2), 284–298, doi:10.1111/j.1365-246X.1993.tb00888.x. [99](#), [101](#)
- Ricard, Y., E. Mattern, and J. Matas (2005), *Earth's Deep Mantle: Structure, Composition, and Evolution*, chap. Synthetic Tomographic Images of Slabs From Mineral Physics, pp. 285–302, American Geophysical Union. [16](#), [30](#)
- Richards, M., H.-P. Bunge, Y. Ricard, and J. R. Baumgardner (1999), Polar wandering in mantle convection models, *Geophys. Res. Lett.*, *26*, 1777–1780, doi:10.1029/1999GL900331. [92](#)
- Richards, M. A., and D. C. Engebretson (1992), Large-scale mantle convection and the history of subduction, *Nature*, *355*(6359), 437–440, doi:10.1038/355437a0. [12](#), [22](#), [56](#), [97](#)
- Richards, M. A., and B. H. Hager (1984), Geoid anomalies in a dynamic Earth, *J. Geophys. Res.*, *89*, 5987–6002. [96](#), [99](#)
- Richards, M. A., Y. Ricard, C. Lithgow-Bertelloni, G. Spada, and R. Sabadini (1997), An Explanation of Earth's Long-Term Rotational Stability, *Science*, *275*, 372–375. [92](#), [101](#)
- Richards, M. A., W. S. Yang, J. R. Baumgardner, and H. P. Bunge (2001), Role of a low-viscosity zone in stabilizing plate tectonics: Implications for comparative terrestrial planetology, *Geochem. Geophys. Geosyst.*, *2*, GC000,115, doi:10.1029/2000GC000115. [38](#)

- Ringwood, A. E. (1975), *Composition and Petrology of the Earth's Mantle*, McGraw-Hill Company, New York, bb55. [17](#), [23](#), [94](#)
- Ritsema, J., and H. J. Van Heijst (2000), Seismic imaging of structural heterogeneity in Earth's mantle: Evidence for large-scale mantle flow, *Science Progress*, *83*, 243–259. [22](#)
- Ritsema, J., and H. J. van Heijst (2002), Constraints on the correlation of P- and S-wave velocity heterogeneity in the mantle from P, PP, PPP and PKPab traveltimes, *Geophys. J. Int.*, *149*(2), 482–489, doi:10.1046/j.1365-246X.2002.01631.x. [12](#), [22](#), [56](#)
- Ritsema, J., S. Ni, D. V. Helmberger, and H. P. Crotwell (1998), Evidence for Strong Shear Velocity Reductions and Velocity Gradients in the Lower Mantle Beneath Africa, *Geophys. Res. Lett.*, *25*(23), 4245–4248. [56](#), [58](#), [68](#)
- Ritsema, J., H. J. Van Heijst, and J. H. Woodhouse (1999), Complex shear velocity structure imaged beneath Africa and Iceland, *Science*, *286*, 1925–1928, doi:10.1126/science.286.5446.1925. [12](#), [22](#)
- Ritsema, J., H. J. van Heijst, and J. H. Woodhouse (2004), Global transition zone tomography, *J. Geophys. Res.*, *109*(B2), doi:10.1029/2003JB002610. [12](#), [18](#), [41](#), [50](#), [51](#), [52](#), [55](#), [56](#), [59](#), [60](#), [61](#), [73](#), [79](#), [81](#), [83](#)
- Ritsema, J., A. K. McNamara, and A. L. Bull (2007), Tomographic filtering of geodynamic models: Implications for model interpretation and large-scale mantle structure, *J. Geophys. Res.*, *112*(B1), B01,303, doi:10.1029/2006JB004566. [15](#), [57](#), [58](#)
- Roberts, P. H., and G. A. Glatzmaier (2000), A test of the frozen-flux approximation using a new geodynamo model, *Phil. Trans. R. Soc. Lond.*, *358*(1768), 1109–1121, doi:10.1098/rsta.2000.0576. [37](#)
- Roberts, P. H., C. A. Jones, and A. R. Calderwood (2003), Energy fluxes and ohmic dissipation in the earth's core, *Earth's Core And Lower Mantle*, *11*, 100–129. [37](#)
- Romanowicz, B., and Y. C. Gung (2002), Superplumes from the core-mantle boundary to the lithosphere: Implications for heat flux, *Science*, *296*, 513–516, doi:10.1126/science.1069404. [36](#), [103](#)
- Samuel, H., C. G. Farnetani, and D. Andraut (2005), *Earth's Deep Mantle: Structure, Composition, and Evolution*, chap. Heterogeneous lowermost mantle: Compositional constraints and seismological observables, pp. 101–116, AGU. [56](#)

- Schaber, K. (2008), The geoid and true polar wander signature of mass transport in Earth's mantle, Master's thesis, Ludwig-Maximilians-Universität München. [17](#), [91](#)
- Schilling, J. G. (1991), Fluxes and excess temperatures of mantle plumes inferred from their interaction with migrating midocean ridges, *Nature*, *352*(6334), 397–403, doi:10.1038/352397a0. [35](#)
- Schuberth, B. S. A., H.-P. Bunge, G. Steinle-Neumann, C. Moder, and J. Oeser (2009), Thermal versus elastic heterogeneity in high-resolution mantle circulation models with pyrolite composition: High plume excess temperatures in the lowermost mantle, *Geochem. Geophys. Geosyst.*, *10*(1), Q01W01, doi:10.1029/2008GC002235. [55](#), [56](#), [57](#), [59](#), [61](#), [70](#), [73](#), [94](#), [95](#), [107](#)
- Sigloch, K., N. McQuarrie, and G. Nolet (2008), Two-stage subduction history under North America inferred from multiple-frequency tomography, *Nature Geoscience*, *1*(7), 458–462, doi:10.1038/ngeo231. [39](#)
- Simmons, N. A., A. M. Forte, and S. P. Grand (2007), Thermochemical structure and dynamics of the African superplume, *Geophys. Res. Lett.*, *34*, L02,301, doi:10.1029/2006GL028009. [12](#), [36](#), [41](#), [50](#), [51](#), [52](#), [56](#), [57](#), [59](#), [102](#)
- Sleep, N. H. (1990), Hotspots and mantle plumes - some phenomenology, *J. Geophys. Res.*, *95*(B5), 6715–6736. [12](#), [23](#), [37](#), [92](#)
- Sleep, N. H. (2003), Simple features of mantle-wide convection and the interpretation of lower-mantle tomograms, *Comptes Rendus Geoscience*, *335*(1), 9–22, doi:10.1016/S1631-0713(03)00008-7. [23](#), [35](#), [93](#)
- Staudigel, H., K. H. Park, M. Pringle, J. L. Rubenstone, W. H. F. Smith, and A. Zindler (1991), The longevity of the South-Pacific isotopic and thermal anomaly, *Earth Planet. Sci. Lett.*, *102*(1), 24–44, doi:10.1016/0012-821X(91)90015-A. [43](#)
- Stegman, D. R., M. A. Richards, and J. R. Baumgardner (2002), Effects of depth-dependent viscosity and plate motions on maintaining a relatively uniform mid-ocean ridge basalt reservoir in whole mantle flow, *J. Geophys. Res.*, *107*(B6), 2116, doi:10.1029/2001JB000192. [23](#), [102](#)
- Steinberger, B. (2000), Slabs in the lower mantle - results of dynamic modelling compared with tomographic images and the geoid, *Phys. Earth Planet. Inter.*, *118*(3-4), 241–257, doi:10.1016/S0031-9201(99)00172-7. [25](#), [102](#)
- Steinberger, B., and R. Holme (2008), Mantle flow models with core-mantle boundary constraints and chemical heterogeneities in the lowermost mantle, *J. Geophys. Res.*, *113*(B5), B05,403, doi:10.1029/2007JB005080. [13](#), [35](#), [57](#)

- Steinberger, B., and R. J. OConnell (1997), Changes of the Earth's rotation axis owing to advection of mantle density heterogeneities, *Nature*, *387*(6629), 169–173. [92](#)
- Steinle-Neumann, G., L. Stixrude, R. E. Cohen, and O. Gulseren (2001), Elasticity of iron at the temperature of the Earth's inner core, *Nature*, *413*(6851), 57–60, doi:10.1038/35092536. [13](#), [35](#), [57](#), [101](#)
- Stixrude, L., and C. Lithgow-Bertelloni (2005), Thermodynamics of mantle minerals - I. Physical properties, *Geophys. J. Int.*, *162*(2), 610–632, doi:10.1111/j.1365-246X.2005.02642.x. [16](#), [18](#), [24](#), [34](#), [44](#), [45](#), [47](#), [49](#), [52](#), [57](#)
- Stixrude, L., and C. Lithgow-Bertelloni (2007), Influence of phase transformations on lateral heterogeneity and dynamics in Earth's mantle, *Earth Planet. Sci. Lett.*, *263*, 45–55, doi:10.1016/j.epsl.2007.08.027. [15](#), [16](#), [18](#), [24](#), [30](#), [32](#), [34](#), [44](#), [45](#), [47](#), [49](#), [52](#), [57](#), [93](#)
- Su, W.-j., and A. M. Dziewonski (1997), Simultaneous inversion for 3-D variations in shear and bulk velocity in the mantle, *Phys. Earth Planet. Inter.*, *100*(1-4), 135–156, doi:10.1016/S0031-9201(96)03236-0. [12](#), [22](#), [36](#), [52](#), [56](#)
- Su, W.-j., R. L. Woodward, and A. M. Dziewonski (1994), Degree 12 model of shear velocity heterogeneity in the mantle, *J. Geophys. Res.*, *99*(B4), 6945–6980. [12](#), [56](#)
- Tackley, P. J. (2000), Mantle convection and plate tectonics: Toward an integrated physical and chemical theory, *Science*, *288*(5473), 2002–2007, doi:10.1126/science.288.5473.2002. [23](#), [102](#)
- Tackley, P. J. (2002), Strong heterogeneity caused by deep mantle layering, *Geochem. Geophys. Geosyst.*, *3*, 1024, doi:10.1029/2001GC000167. [23](#)
- Talagrand, O. (1997), Assimilation of observations, an introduction, *Journal Of The Meteorological Society Of Japan*, *75*(1B), 191–209. [25](#)
- Tarduno, J. A., and A. V. Smirnov (2001), Stability of the Earth with respect to the spin axis for the last 130 million years, *Earth Planet. Sci. Lett.*, *184*(2), 549–553. [15](#), [92](#)
- Tateno, S., K. Hirose, N. Sata, and Y. Ohishi (2009), Determination of post-perovskite phase transition boundary up to 4400 k and implications for thermal structure in D'' layer, *Earth Planet. Sci. Lett.*, *277*(1-2), 130 – 136, doi:10.1016/j.epsl.2008.10.004. [69](#)
- Torsvik, T. H., R. D. Müller, R. V. der Voo, B. Steinberger, and C. Gaina (2008), Global plate motion frames: Toward a unified model, *Rev. Geophys.*, *46*, RG3004, doi:10.1029/2007RG000227. [27](#), [38](#)

- Trampert, J., P. Vacher, and N. Vlaar (2001), Sensitivities of seismic velocities to temperature, pressure and composition in the lower mantle, *Phys. Earth Planet. Inter.*, *124*(3-4), 255–267, doi:10.1016/S0031-9201(01)00201-1. [32](#)
- Trampert, J., F. Deschamps, J. Resovsky, and D. Yuen (2004), Probabilistic tomography maps chemical heterogeneities throughout the lower mantle, *Science*, *306*(5697), 853–856, doi:10.1126/science.1101996. [13](#), [22](#), [36](#), [56](#), [102](#)
- Tromp, J., C. Tape, and Q. Y. Liu (2005), Seismic tomography, adjoint methods, time reversal and banana-doughnut kernels, *Geophys. J. Int.*, *160*(1), 195–216, doi:10.1111/j.1365-246X.2004.02453.x. [39](#)
- Trompert, R., and U. Hansen (1998), Mantle convection simulations with rheologies that generate plate-like behaviour, *Nature*, *395*(6703), 686–689. [38](#)
- Tsai, V., and D. Stevenson (2007), Theoretical constraints on true polar wander, *J. Geophys. Res.*, *112*, doi:10.1029/2005JB003923. [101](#)
- Turcotte, D. L., and G. Schubert (2001), *Geodynamics*, 528 pp., Cambridge University Press, second edition. [37](#)
- Urey, H. C. (1956), The cosmic abundances of potassium, uranium, and thorium and the heat balances of the earth, the moon, and mars, *Proceedings Of The National Academy Of Sciences Of The United States Of America*, *42*(12), 889–891. [25](#), [37](#)
- van der Hilst, R., R. Engdahl, W. Spakman, and G. Nolet (1991), Tomographic imaging of subducted lithosphere below northwest pacific island arcs, *Nature*, *353*, 37–43. [11](#)
- van der Hilst, R. D., and H. Karason (1999), Compositional heterogeneity in the bottom 1000 kilometers of earth’s mantle: Toward a hybrid convection model, *Science*, *283*(5409), 1885–1888, doi:10.1126/science.283.5409.1885. [12](#), [22](#), [56](#)
- van der Hilst, R. D., S. Widiyantoro, and E. R. Engdahl (1997), Evidence for deep mantle circulation from global tomography, *Nature*, *386*(6625), 578–584, doi:10.1038/386578a0. [12](#), [22](#), [56](#)
- van der Hilst, R. D., M. V. de Hoop, P. Wang, S. H. Shim, P. Ma, and L. Tenoerio (2007), Seismostratigraphy and thermal structure of Earth’s core-mantle boundary region, *Science*, *315*, 1813–1817, doi:10.1126/science.1137867. [13](#), [35](#), [57](#), [101](#)
- van der Lee, S., and G. Nolet (1997), Seismic image of the subducted trailing fragments of the farallon plate, *Nature*, *386*(6622), 266–269. [12](#)

- Vine, F. J., and D. H. Matthews (1963), Magnetic anomalies over oceanic ridges, *Nature*, 199(4897), 947–949. [10](#)
- Wang, Y., and L. Wen (2004), Mapping the geometry and geographic distribution of a very low velocity province at the base of the Earth’s mantle, *J. Geophys. Res.*, 109(B10), B10,305, doi:10.1029/2003JB002674. [12](#), [22](#), [56](#)
- Wang, Y. B., and D. J. Weidner (1996),  $(\frac{\partial \mu}{\partial T})_P$  of the lower mantle, *Pure Appl. Geophys.*, 146(3-4), 533–549, doi:10.1007/BF00874732. [36](#), [68](#)
- Wegener, A. (1915), *Die Entstehung der Kontinente und Ozeane*, 1 ed., Vieweg, Braunschweig. [10](#)
- Wen, L. X., P. G. Silver, D. James, and R. Kuehnel (2001), Seismic evidence for a thermo-chemical boundary at the base of the Earth’s mantle, *Earth Planet. Sci. Lett.*, 189, 141–153, doi:10.1016/S0012-821X(01)00365-X. [12](#), [22](#), [56](#)
- Yanagisawa, T., and Y. Hamano (1999), “skewness” of s-wave velocity in the mantle, *Geophys. Res. Lett.*, 26(6), 791–794. [33](#)
- Zhang, J. Z., and D. J. Weidner (1999), Thermal equation of state of aluminum-enriched silicate perovskite, *Science*, 284(5415), 782–784, doi:10.1126/science.284.5415.782. [36](#)
- Zhong, S. J. (2006), Constraints on thermochemical convection of the mantle from plume heat flux, plume excess temperature, and upper mantle temperature, *J. Geophys. Res.*, 111(B4), B04,409, doi:10.1029/2005JB003972. [23](#)



# Curriculum Vitae

## Bernhard Schuberth

---

### Date and Place of Birth

21.07.1977                      Regensburg, Germany

### Education

May 2004 - July 2009              PhD Student in computational geodynamics/seismology within the International Graduate College "THESIS" of the Elite-Network Bavaria  
Dept. of Earth and Environmental Sciences, Ludwig-Maximilians-Universität München

Nov. 2003                              Graduation with distinction in Geophysics (Diplom)

Nov. 1997 - Nov. 2003              Studies of Geophysics  
Ludwig-Maximilians-Universität München

Jun. 1996                                Allgemeine Hochschulreife

1987 - 1996                              Werner-Heisenberg-Gymnasium Garching (Secondary School)

1983 - 1987                              Grundschule Garching Ost (Primary School)

### Internships and Working Experience

Mar./Apr. 2004                      Graduate Assistant, Geophysics Section, Dept. for Earth and Environmental Sciences, LMU Munich

Nov. 2002 - Feb. 2004              Student Assistant, Geophysics Section, Dept. for Earth and Environmental Sciences, LMU Munich

Aug. - Oct. 2002                      Participation in the Arctic Expedition ARK XVIII/2 on board the RV and Polarstern as Student Assistant of the Alfred Wegener Institute for Polar Marine Research

Oct. 2001 - Mar. 2002	Working Student at S.u.B. Handelshaus GmbH, Munich
Aug. - Sep. 2001	Student Trainee at TiNOX GmbH, Munich
Nov. 2000 - Jan. 2001	Working Student in the Legal Dept., Hypover-einsbank Munich
Apr. - Aug. 2000	Student Trainee at the Dept. for Satellite Navigation, Astrium Space GmbH (EADS), Otto-brunn
Mar. - Jul. 2001	Student Assistant at the German Geodetic Research Institute, Munich
Nov. 1999 - Oct. 2000	Student Assistant at the German Geodetic Research Institute, Munich
Oct. 1999	Internship at the Institute of Atmospheric Physics, German Aerospace Center (DLR), Oberpfaffenhofen
Mar. 1999	Working Student in the Legal Dept., Hypover-einsbank Munich

### **Awards**

March 2008	Best Oral Presentation Award of the German Geophysical Society (DGG) for a talk given at the 67th Annual Meeting 2007 in Aachen, Germany
Jun. 2004	Edison Award - Silver Prize of the General Electrics Foundation and the Institute of International Education
Feb. 2002 - 2008	Stipend from e-fellows.net